Micro-integrated Diode Laser Modules for Quantum Optical Sensors in Space

vorgelegt von
Anja Kohfeldt,
M.Sc.
geb. in Malchin

von der Fakultät IV – Elektrotechnik und Informatik
Technische Universität Berlin
zur Erlangung des akademischen Grades

Doktor der Naturwissenschaften
– Dr. rer. nat. –

genehmigte Dissertation

Promotionsausschuss:

Vorsitzender:	Prof. Dr. Klaus Petermann
Gutachter:	Prof. Dr. Günther Tränkle
Gutachter:	Prof. Achim Peters, Ph.D.
Gutachter:	Prof. Dr. Klaus Brieß

Tag der wissenschaftlichen Aussprache: 20.07.2017

Berlin 2017

Abstract

Quantum sensors are rely on laser technology for preparation and for manipulation of their quantum probes. With the endeavour of operating quantum sensors in microgravity in order to gain measurement precision, laser technology has to be developed further to meet the new requirements. In addition to high frequency stability at specific wavelengths and sufficient optical output power, the laser modules have to be small in size, lightweight, mechanically robust and energy efficient to be suitable for operations outside the laboratory, even outside Earth‘s mesosphere.

With FOKUS, the first optical clock in space, and MAIUS, the first atom interferometer in space, two ambitious sounding rocket experiments were initiated that push the boundaries of both quantum technology and laser technology further.

In this thesis, the laser modules for both quantum sensor missions were developed, assembled, characterized, and validated. Semiconductor laser diodes are best suited for small, robust, and energy efficient laser sources. However, the optical output power of a single diode is limited, and they suffer from frequency stability issues, such as distortions induced by feedback reflection, and thermal drift.

To overcome these issues, a master oscillator power amplifier (MOPA) configuration, embedded in a hybrid micro-integrated design was chosen. As optical master oscillator (MO) a distributed feedback (DFB) diode optimized for narrow linewidth emission at the designated wavelength is used. The MO is shielded against external feedback by optical isolators. The optical emission of the DFB diode is guided to a separate optical amplifier chip, boosting the optical output power. All optical components are hosted on a micro-optical bench (MIOB) made of aluminium nitride for mechanical stiffness and good thermal conductivity. In addition to the optical and electro-optical components, it contains temperature sensors for monitoring and thermal stabilization, as well as an electrical interface supporting the frequency stabilization by allowing the on-board modulation of the laser diodes injection current. The MIOB has a footprint of 80 mm x 25 mm. It omits movable parts to increase mechanical stability, and it provides space for an optical fibre coupler on board the MIOB.

To ensure that the requirements on the laser modules can be fulfilled components are run through a qualification process as described in this thesis before being integrated onto the MIOB. Further, an assembly procedure with active alignment and in-assembly-characterization is presented.

After integration the laser modules undergo an electro-optical characterization, revealing that a FWHM linewidth of $<$400 kHz and an intrinsic linewidth of $<$15 kHz (3 mm long DFB diode at 100 mW DFB output power) can be achieved. The laser modules provide a spectral single-mode tuning range of $>$1.5 nm, an optical free space output power of $>$1 W, and an electrical-to-optical efficiency of almost 30%.

The robustness against environmental influences was validated with random-vibration tests up to 29 g_{RMS}, a half-sine shock test at 1500 g, and thermal cycles up to a temperature range of -55°C to $+85$°C. The laser modules still operated according to the requirements after these stress tests.

The suitability of these laser modules for spaceborne quantum-optical sensors is proven in the FOKUS and MAIUS experiments. FOKUS was launched successfully in April 2015, hosting a DFB module based on the technology developed in this thesis. The FOKUS apparatus was still operational after returning to Earth. MAIUS was launched in January 2017, hosting 5 MOPA modules and a DFB module. All laser modules operated as expected during and after the mission.

The laser modules developed in this thesis are suitable for Earth-bound experiments as well, e.g. in mobile measurement setups or to save space in laboratories. The concept is adaptable to other wavelengths, not only increasing the number of atom species that can be manipulated but also enabling usage in other applications, such as in optical communications.

Zusammenfassung

Für Quantensensoren spielen Laser eine entscheidende Rolle, sowohl bei der Aufbereitung als auch bei der Manipulation der zu untersuchenden Quantenproben. Mit den Bestrebungen Quantensensoren in Schwerelosigkeit zu betreiben um die Messgenauigkeit zu erhöhen, muss sich auch die Lasertechnologie weiterentwickeln. Neben den Anforderungen nach hoher Frequenzstabilität bei bestimmten Wellenlängen und ausreichender optischer Ausgangsleistung müssen Lasermodule kompakt, leicht, robust und energieeffizient sein um aus außerhalb des Labors, gar außerhalb der Erdmesosphäre betrieben werden zu können.

Mit FOKUS, der ersten optischen Uhr im Weltraum, und MAIUS, dem ersten Atominterferometer im Weltraum, sind zwei ambitionierte Höhenforschungsraketenmissionen ins Leben gerufen worden, welche sowohl die Quantensensortechnologie, als auch die Lasertechnologie voranbringen. Im Rahmen dieser Dissertation wurden die Lasermodule für diese beiden Missionen entwickelt, integriert, charakterisiert und validiert.

Halbleiterlaserdioden sind sehr kompakt und robust, sowie energieeffizient. Jedoch ist die optische Ausgangsleistung einzelner Dioden begrenzt und sie sind anfällig für spektrale Störungen, wie optisches Feedback und thermische Drifts.

Um diesen Limitierungen entgegenzuwirken wurde das Konzept eines hybriden, mikro-integrierten Masteroszillator-Poweramplifier (MOPA) gewählt. Als Masteroszillator (MO) dient ein Distributed-Feedback (DFB) Laser, welcher für die Emission mit schmaler Linienbreite optimiert wurde. Der MO wird mit Hilfe von optischen Isolatoren vor externem Feedback abgeschirmt. Der optische Beam des MO wird zu einer separaten Verstärkerdiode geführt, welche die optische Ausgangsleistung erhöht. Alle optischen und elektro-optischen Komponenten des Lasermoduls sitzen auf einer mikrooptischen Bank (MIOB) aus Aluminiumnitrid mit hoher mechanischer Steifigkeit und guter Wärmeleitfähigkeit. Neben den optischen Komponenten sitzen auf der MIOB Temperatursensoren zur Überwachung und Stabilisierung der Modultemperatur. Zudem bietet die MIOB ein elektrisches Interface mit Coaxialanschlüssen und der Option, den Injektionsstrom für die Frequenzstabilisierung der Halbleiterdioden auf der MIOB direkt zu modulieren. Die MIOB hat eine Grundfläche von 80 mm x 25 mm und verzichtet komplett auf bewegliche Teile um die mechanische Stabilität zu erhöhen.

Um sicherzustellen, dass die Lasermodule die Missionsanforderungen erfüllen können, werden die optischen und elektro-optischen Komponenten vor der Integration einem Qualifizierungsprozess unterzogen, welcher in dieser Arbeit beschrieben ist. Des Weiteren wird der Integrationsprozess der Komponenten in die MIOB ausgeführt.

Nach Fertigstellung der Integration werden die Lasermodule einer elektro-optischen Charakterisierung unterzogen. Diese zeigt auf, dass die Lasermodule FWHM-Linienbreiten von $<$400kHz und intrinsische Linienbreiten von $<$15 kHz (3 mm lange DFB-Diode, bei je 100 mW Ausgangsleistung) erreichen können. Die Lasermodule sind spektral single-mode über einen Wellenlängenbereich von 1,5 nm durchstimmbar, erreichen eine optische Ausgangsleistung von $>$1 W und weisen eine Effizienz von nahezu 30% bei der Wandlung von elektrischer zu optischer Energie auf.

Die Widerstandsfähigkeit gegen externe Umwelteinflüsse wird mit Random-Vibration-Tests mit bis zu 29 g_{RMS}, Halb-Sinus-Schocktest mit Amplituden bis zu 1500 g, und Thermalzyklentests im Temperaturbereich von – 55°C bis + 85°C validiert. Die Performance der Lasermodule entsprach auch nach den Umwelttests noch den Missionsanforderungen.

Die Eignung der Lasermodule für den Einsatz in Quantensensoren im Weltraum wird durch die FOKUS und MAIUS-Missionen unter Beweis gestellt. Die FOKUS-Apparatur, welche ein DFB-Modul basierend auf der Technologie dieser Arbeit enthielt, wurde im April 2015 erfolgreich gestartet. Die Apparatur war auch nach Rückkehr auf die Erde noch voll funktionsfähig. Die MAIUS Mission wurde im Januar 2017 erfolgreich durchgeführt, mit 5 MOPA-Modulen und einem DFB-Modul an Bord. Auch bei MAIUS funktionierten die Lasermodule während und nach dem Raketenflug einwandfrei.

Die Lasermodule, die während dieser Dissertation entwickelt wurden, eignen sich auch für den Einsatz in erdgebundenen Experimenten. Das Konzept ist für andere Wellenlängen adaptierbar. Damit erweitern sich nicht nur die Zahl der manipulierbare Atomspezien in Quantenexperimenten, auch der Einsatz der Lasermodule für andere Anwendungen, wie etwa optische Kommunikation, wäre denkbar.

Acknowledgements

First, I would like to thank Professor Günther Tränkle who gave me the opportunity to work in the motivating environment of the Ferdinand-Braun-Institut, Leibniz Institut für Höchstfrequenztechnik (FBH). I would like to acknowledge his support, professional supervising, and helpful discussions.

I am deeply grateful to Dr. Andreas Wicht for his support and his valuable contributions to this work. His enthusiasm and commitment to research was very inspiring. Further, I would like to thank him for sharing his wide experience in the field of quantum optical metrology.

I would also like to acknowledge Professor Achim Peters, for his insights into applied physics, and to thank him for using my laser modules in the laser systems designed in his group.

I would like to thank Max Schiemangk for introducing me to the Hexapod micro integration environment and the linewidth measurement, and for his helpful support in the lab and for the proofreading of almost all of my abstracts.

This work would not have been possible without everybody at FBH who was involved in diode laser processing and production. Especially I want to acknowledge Sabrina Kreutzmann and Arnim Ginolas for the diode assembly, but also for all discussions about bonding, wire bonding, and for the help to remove faulty components. Maik Erbe and Robert Smol did a great job in supporting me with all the electro-optical characterizations performed over the years. Thank you!

Further, I would like to thank the entire Laser Metrology Lab at FBH for establishing and running a fantastic lab, but also for all the lunch and in-between discussions, and for the beer and pizza from time to time.

I am grateful to Markus for the motivation that kept me working and for the discussions about cold atoms in general.

Special thanks go to Aline, Hanna, Sunti, Belkeys, Fredi, and Heike for reading and commenting on this thesis.

I would like to thank the DLR for funding under grant number: 50WM1134.

Finally, I would like to thank my family, first Benno for always being around when I need him, for all the motivation, dissipation, and bringing me back to focus again. And of course I have to thank my parents for all the support and trust they put into me. This thesis would have been impossible without you. <3

Contents

Chapter 1

Lasers and Quantum Optical Sensors in Space

1.1 Lasers in Space

Ever since the first laser, an acronym for light amplification by stimulated emission of radiation, was constructed by Mainman in 1960 [1], the monochromatic and coherent light sources gained rapidly in importance and applications. One year later, in 1961, a ruby laser was used by Campbell and Koester [2] to destroy a tumour. With that, the laser was introduced to medicine. Nowadays it is an indispensable part of surgery. Today, lasers have widely spread applications in industry, everyday life, spanning from material processing [3] to optical communication [4, 5], medicine and entertainment. Lasers also play an important role in metrology and science. A short wavelength source of coherent radiation not only allows for high precision measurements [6], it can also be used to manipulate atom states and hence constitute a basic tool for atom physics and quantum optical metrology (see section 1.2).

With this wide spectrum of applications it is not surprising that lasers are operated in very different environments. One of the most demanding operation environments is space[1]. Not only that lasers have to be small in size, low in weight, and power efficient in order to minimize launch costs and required resources, they have to survive vibrations and shocks, radiation, and temperature gradients up to some 100 K. When operated on a satellite, they have to be extremely reliable because malfunctioning parts can typically not be replaced.

In space, lasers are mostly used in measurement and communication devices. A popular measuring device is a light detection and ranging (LIDAR) system, which can be used for supporting docking manoeuvres and to analyse atmospheric compositions. The first airborne LIDAR instrument was reported in 1985 [7], followed by the first LIDAR instrument in space, the Lidar In-space Technology Experiment (LITE), conducted by "National Aeronautics and Space Administration" (NASA) in 1994 at the STS-64 space shuttle mission. It used a pair of flash light pumped Nd:YAG lasers, con-

[1] There are a lot of definitions of "space". One of the most accepted definitions is given by the Fédération Aéronautique Internationale (FAI) with everything outside the Kármán line, 100 km above sea level.

suming 1865 W when transmitting [8], the total instrument mass was 990 kg. Modern spaceborne LIDAR missions, such as the EarthCARE mission, scheduled for 2018, are still based on Nd:YAG lasers, however, the instrument's consumption and mass could be reduced to around 300 W and 230 kg, respectively [9].

Optical satellite communication with lasers gains importance, building a network around Earth to cope with the increasing demand for higher data rates and availability even in remote areas [10]. The first inter-satellite link was demonstrated 2001 with the Semiconductor-laser Inter-satellite Link EXperiment (SILEX) by European Space Agency (ESA) [11] using semiconductor lasers with an optical output power of 60 mW, transmitting up to 50 Mbit/s. The total mass of the optical terminal was 160 kg [12]. Depending on the application, spectral requirements on the lasers can be very strict. In communication, dependent on the modulation procedure, linewidths smaller than 8 MHz[2], or even down to 6.9 kHz[3] are necessary. Emission output power levels larger than 1 W are desirable to bridge long distances in space communication.

The requirements on laser sources for space communications are comparable to requirements that apply to certain quantum optics applications. Natural linewidths of alkali atom transitions may be, as well, in the range of 6 MHz [15, 16], the linewidth requirement for the coherent manipulation of atomic ensembles may be in the range of less than 100 kHz [17]. Also, more than 1 W output power per laser source may be required. These quantum optical sensors also reach out into space to gain precision, as will be described in section 1.2. Hence, stable, compact, and reliable laser sources will soon be required for quantum metrology applications in space.

Commonly, fibre lasers or optically pumped solid-state laser technologies are used to fulfil the requirement combination of narrow linewidth and high output power. However, solid-state lasers are quite energy inefficient [8], large, and are limited to very specific emission frequencies. By developing all-semiconductor based laser systems for space applications, it is possible to minimize the size and weight as well as the power consumption of the instruments. Semiconductor lasers also enable a wide range of emission frequencies and are, therefore, the best technology choice for quantum optical sensors in space.

1.2 Quantum Optical Metrology in Space

The discoveries in the field of quantum physics in the past century [18–21] laid the basis for the construction of measurement devices with a precision beyond what is possible with classical approaches. Quantum metrology makes use of the wave-particle dualism [22] and is in theory ultimately limited by the uncertainty principle. High-precision quantum sensors can be used to detect gravitational waves [23]. They are used to precisely determine physical constants [24–26] or acceleration [17, 27]. The most precise, man-made reference systems (clocks) are based on atomic transitions [28, 29]. Applications for quantum technology can be found not only in fundamental

[2]with binary phase-shift keying (BPSK) [13]

[3]with quadrature amplitude modulation (QAM) [14]

physics, but also in time keeping and navigation, and in Earth exploration, as well as in telecommunication.

Quantum optical technologies are based on single atoms or ions, or on precisely controlled ensembles of atoms or ions. They owe their potential to the fact that the properties of an atom are well known and the interactions with the environment can be described very accurately. This is important for understanding the measurement environment and to guarantee accuracy and reproducibility of the measurement. A milestone for quantum optical sensors was the first realization of a Bose-Einstein condensate (BEC) [30,31], a macroscopic quantum object that can be described by a single wave function and allows for the implementation of high-resolution atom interferometers [32, 33], for example to determine accelerations.

The sensitivity of these experiments, however, increases with the measurement time. To enhance the sensitivity, atom interferometers have been realized with atomic ensembles launched in an atomic fountain apparatus [27, 34, 35] or dropped in drop-towers [36]. Both approaches provide microgravity environments on a limited scale on Earth. However, in Earth-bound experiments the duration of the microgravity period and hence of the measurement time is limited. Deploying atom interferometers in space is an approach to overcome this limitation. A first step towards space is the deployment on a sounding rocket, extending the measuring time from seconds to several minutes.

Measurement apparatus, leaving the laboratory in order to be operated on mobile platforms or even in space, must fulfil the environmental requirements, given by the platform. Hence, new technologies have to be developed.

Quantum sensors rely on ultra-precise oscillators, lasers for atom cooling, stimulation, and manipulation. In most laboratory based experiments the precise oscillators are realized with solid-state lasers, such as the Nd:YAG lasers [23], Ti:Sapphire laser [37] or Er:Glass with a crystal cavity [38, 39]. These laser systems require an active, optical medium for pumping, either realized with flash lights or with diode lasers. This reduces the efficiency of the laser, adds complexity to the system and increases the weight. The wavelength is defined by the doping, hence the spectral tuning range is very limited for most solid-state laser types. With renouncing the solid-state cavity and operating with the semiconductor laser directly, the laser system of quantum sensors can be designed in a more compact and energy efficient way. However, frequency stability of the diode emission has to be ensured.

The focus of this work is on the development and implementation of semiconductor based laser modules for quantum sensors on board sounding rockets.

1.3 Outline of this Thesis

As explained above, laser systems that are reliable, compact, robust, and energy efficient are key components of quantum optical sensors, specifically for sensors operated in space. The aim of this thesis is to develop laser modules for quantum optical experiments on BECs of rubidium and potassium on board of sounding rockets.

Chapter 2 introduces two quantum optical experiment missions that are operated in space on board of sounding rockets, the FOKUS mission and the MAIUS mission. Based on the experiment's requirements and on the operation environment, the requirements and specifications that apply to the lasers for these experiments are derived.

In chapter 3 the basic theory of semiconductor lasers is presented. Laser module configuration concepts such as the MOPA concept and the hybrid integration approach are discussed.

Based on the requirements identified in chapter 2 and the technology introduced in chapter 3, the design of the laser modules is described in chapter 4. The chapter also outlines the integration process of the semiconductor laser modules, including the description of a specially developed assembly station for active alignment of all optical components, as well as the description of the micro-integration procedure.

Single components, such as laser diodes, amplifiers, as well as passive components have to be qualified before integration to ensure stable and reliable performance. Chapter 5 focusses on the preparation and characterization of these components. Qualification criteria of the components are defined and the description of a specially developed pre-integration measurement setup is presented. Furthermore, typical reasons of failure as well as the total yield of the component qualification process are described and discussed.

Chapter 6 presents a detailed characterization of the laser modules after integration. The electro-optical performance, such as spectral behaviour, optical output power, and frequency stability, is investigated and compared to the mission critical requirements given in chapter 2. Environmental stress tests are carried out and the laser module performances before and after the stress test campaign are compared.

The validated laser modules are delivered for integration into the mission's experiment apparatus. In chapter 7 the results of the FOKUS experiment and the laser module behaviour during the MAIUS mission are presented. The FOKUS experiment aims at the demonstration of the suitability of the newly developed laser module technology for the employment in quantum optical sensors in space. Further, this chapter presents a post-flight characterization of the FOKUS laser module, validating that it is still operational.

Chapter 8 gives a brief summary of lessons learned during the fabrication of the laser modules and an outlook for future work.

Chapter 2

Quantum Sensors and Laser Module Requirements

A new generation of quantum optical sensors is being deployed in microgravity in order to improve measurement accuracy [28, 40]. To move an experiment out of the laboratory and into microgravity (μg), most of the hardware, including the laser modules, have to be re-designed to be able to cope with the new operational environment.

This chapter introduces two experiments on board of sounding rockets that represent quantum sensors in space. In addition to the mission goals and a brief description of the technical realization of the experiments, the requirements of the laser modules are outlined. The mechanical requirements are defined by the environment on board a sounding rocket, the electro-optical requirements are determined by the experiment design and the task that shall be performed by the lasers in the experiment. The summery of these requirements is the baseline of the design of the laser modules that will be discussed in this thesis.

2.1 The Sounding Rocket Experiment FOKUS

Precision frequency control of light is a key requirement for quantum sensors. In order to allow for ultra-precise measurements in microgravity, suitable technology for frequency stabilization has to be provided. The experiment "Faserlaserbasierter Optischer Kammgenerator unter Schwerelosigkeit" (FOKUS)[1], led by Menlo Systems GmbH, a company specialized on frequency combs [41], is the first mission ever to operate optical frequency stabilization technology for semiconductor lasers in space. The FOKUS experiment is described by Lezius in [42].

The following paragraphs present the mission goals and experimental setup of FOKUS and summarize the requirements for the diode laser modules employed in this experiment. The results of the FOKUS experiment, launched in April 2015, are described in chapter 7.

---

[1]The FOKUS activities at the FBH were funded by the Federal Ministry for Economic Affairs and Energy (BMWi) under the grant number 50WM1240

2.1.1 FOKUS Mission Goals

The mission goals of the FOKUS project can be summarized as:

- The development and validation of frequency stabilization technologies of laser systems on board a sounding rocket
- The deployment of the first ever diode laser module with its frequency stabilized to an optical transition, and the first ever frequency comb in space
- A preliminary test of the master laser module and frequency reference system that should also be provided for the "Materiewelleninterferometrie unter Schwerelosigkeit" (MAIUS) mission
- A proof-of-principle for a spaceborne local position invariance (LPI) experiment that includes an optical clock.

The LPI results from the Einstein equivalence principle (EEP) and signifies that two clocks of different internal structure should see the same red-shift as they move together through a changing gravitational field. The experimental setup allows the comparison of two clocks that are based on different oscillators and physical implementations and can hence be considered clocks of different type.

2.1.2 Experimental Setup

The experiment can be divided into two optical subsystems: the frequency comb system and the rubidium (Rb) reference system, as illustrated in figure 2.1.

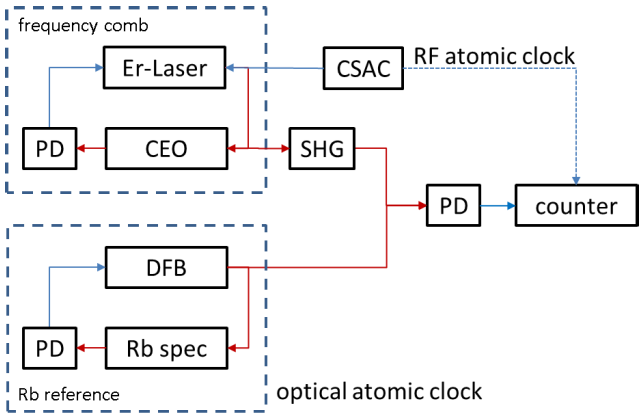

Figure 2.1: Schematic of FOKUS experiment: the RF atomic CSAC is compared to the optical atomic clock, formed by the Rb reference system, via the frequency comb system. Optical signals are illustrated in red, electrical signals in blue.

The Rb reference system (together with the counter) can be considered as optical atomic clock, delivering a frequency stabilized to an optical transition of Rb. The frequency comb system is referenced on a chip scale atomic clock (CSAC) (SA.45s CSAC, Symmetricon), based on microwave oscillation, and allows the comparison of the CSAC with the optical atomic clock. A frequency doubling of the output of the frequency comb system, done by second harmonic generation (SHG), is required to adapt the

output of the frequency comb to the range of the frequency of the Rb reference system. Both frequencies, the Rb reference system output and the corresponding needle of the frequency doubled comb system, are superimposed on a photodiode (PD) and the difference of both frequencies is detected by a counter.

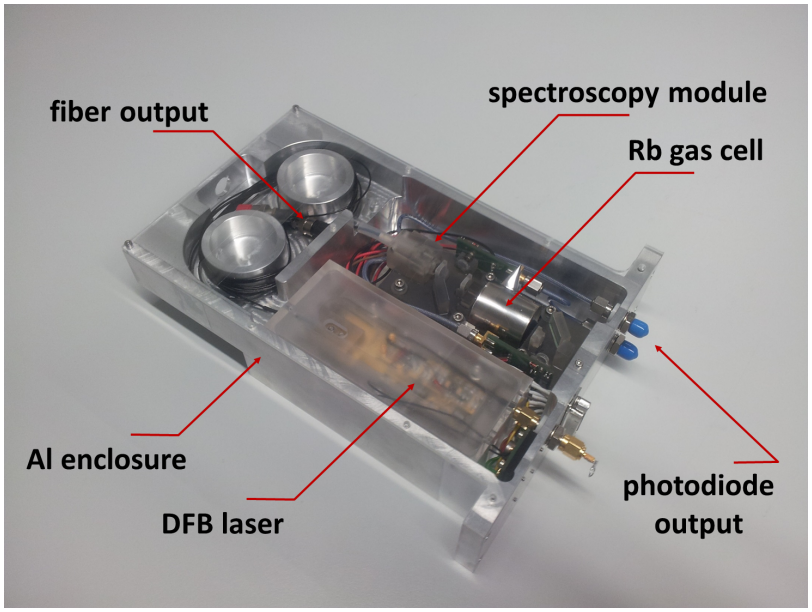

Figure 2.2: FOKUS Rb reference system, hosting a spectroscopy board (right) with master laser (left, underneath semi-transparent lid) in flight model housing

The Rb reference system is depicted in figure 2.2. It consists of a semiconductor laser module and a spectroscopy module. The semiconductor laser module is a distributed feedback (DFB) diode laser micro-integrated on an aluminium nitride (AlN) based micro-optical bench (MIOB). It emits approximately 19 mW at 780 nm. More details of the design of the laser module will be given in chapter 4. The free-space laser beam is collimated with micro-lenses and coupled into a polarization maintaining fibre with a Zerodur fibre coupler on board the MIOB. The beam is guided to the spectroscopy module. The spectroscopy module rests on a 50 mm thick Zerodur base plate in order to maintain the positions of the optically aligned components, independent of the environmental temperatures and mechanical loads. It contains fibre coupled input and free-space optics and is described by Duncker in [43]. The incoming light is first split into two beams with a polarizing beam splitter (PBS). Both beams are guided through a vapour gas cell filled with Rb. While one beam passes the cell only once, the second beam passes the Rb cell twice, producing a Doppler broadened and a Doppler free spectroscopy signal, respectively. Each beam is recorded on a separate PD. The AC part of the Doppler free PD signal is mixed down with a 10 MHz reference signal, provided by the CSAC and serves as a frequency modulation spectroscopy (FMS) error signal for the feedback loop. The FMS error signal is then processed by the servo electronics and fed back to the laser's injection current in order to lock the laser emission frequency to the frequency of the D2 transition ($5^2S_{1/2} \rightarrow 5^2P_{3/2}$) of Rb [15]. A fibre-integrated splitter between laser module and spectroscopy module is used to guide a

fraction of the light to another photodiode, allowing for beat measurements with the light from the frequency comb.

The comb system contains a mode-locked erbium (Er)-fibre laser [44, 45] emitting approximately 3 mW at 1560 nm with a bandwidth of 30 nm [46]. The output of this oscillator is amplified and split with a 1:2 fibre splitter. One part is used in carrier-envelope-offset (CEO) beat detection, the other part is frequency doubled in a SHG stage in order to facilitate beat note measurements with the light from the Rb stabilized diode laser.

The chip scale atomic clock, providing the 10 MHz reference signal of the FOKUS scientific payload, is also used for phase-locking of the repetition rate signal and the carrier envelope offset signal. The CSAC also references the counter that measures the phase of the beat note signal between the Rb system and the frequency comb, as shown in figure 2.1.

2.1.3 Flight Configuration

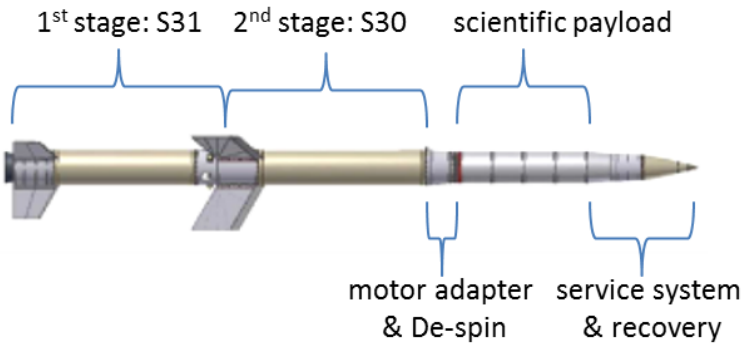

Figure 2.3: Flight configuration of a VSB-30 sounding rocket

The German sounding rocket program "Technologische Experimente unter Schwerelosigkeit" (TEXUS) serves as launch vehicle for the FOKUS experiment. The rocket motor of the TEXUS rocket is a "Veículo de Sondagem Booster – 30" (engl.: Booster Sounding Vehicle) (VSB-30) type booster. It consists of two solid propellant rocket stages, which are depicted in figure 2.3. The rocket was developed at "Instituto de Aeronáutica e Espaço", Brazil (IAE) in cooperation with "Mobile Raketenbasis des Deutschen Zentrums für Luft- und Raumfahrt" (DLR-MORABA) and is launched from Esrange Space Center near Kiruna, Sweden.

The design of the launch vehicle and environment provided by the launch vehicle set limits on the mechanical design of the payload and define the environmental requirements of the payload design. This also affects the components and modules integrated into the scientific payload.

The payload is mounted on top of the rocket engines with a motor adapter ring adjusting the diameter differences between engines and payload. The entire payload

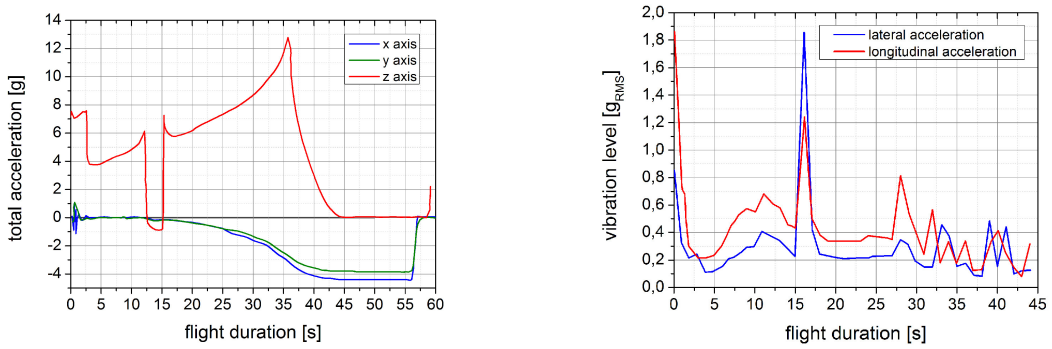

(a) (b)

Figure 2.4: Acceleration load (a) and vibration level (b) of a typical launch. Burnout of 1st stage at 13.5 s, maximum load is reached before burnout of 2nd stage at 36 s. Data from TEXUS 45 mission [47, 48]

is limited to 400 kg and has to fit into an approximately 4500 mm x 440 mm drum shaped envelope [49]. Since the envelope dimensions also include thickness of the outer structure and secondary mounting structure, the space for the actual experiment is even more limited.

With an apogee of about 260 km approximately 360 s of microgravity with a μg level of 10^{-4} g [49] can be achieved. During ascent the engines of the VSB-30 will cause significant acceleration and vibration. Figure 2.4 illustrates a typical acceleration load during launch. The z-acceleration peaks shortly before burnout of the second stage (S30 engine) with 12.1 g at 13 s. Vibration levels peak at ignition of each stage at 0 s and 18 s time of flight. The integrated RMS value should not exceed 2 g_{RMS}. However, it is recommended for TEXUS flights that payload components as well as experiment modules are considered with 8.1 g_{RMS} qualification level [47] in all three axes as design parameter. At re-entry even higher accelerations are expected, though they might differ due to the re-entry conditions at 40 km altitude and the centre of gravity of the payload. Friction of the atmosphere causes 20 – 25 g while touch down shocks are in the range of 50 g to 250 g [47]. Depending whether the experiment shall be operational after touch down, these acceleration loads have to be taken into account as well.

During launch preparation the VSB-30 is connected to the ground support equipment (GSE), providing the payload with electricity, data link and fluids like cooling water. At launch the connection to the GSE is cut and the experiments have to perform autonomously. Since the service module does not provide sufficient electricity for most experiments, a battery with additional capacity to supply the experiment's electronics have to be included in the scientific payload, on the cost of space and weight for the experimental apparatus. Additionally this limits the power consumption of the experiment. Therefore energy efficient components for the experimental hardware have to be chosen.

For frequency stabilized components heat management is an important issue as well. Since the operation during flight only lasts several minutes, an active cooling of

requirements	value	comment
	electro-optical	
wavelength (λ)	780.241 nm	^{87}Rb D2 line [15]
FWHM linewidth	$\leq$ 6 MHz	^{87}Rb D2 line [15]
tunability at WP	100 GHz	^{87}Rb D2 [15] + margin
free-space optical power	$>$ 10 mW (CW)	system design
max. WP current	200 mA	current driver limitation
	mechanical/environmental	
volume	$<$ (200 x 100 x 50) mm^3	system design
vibration loads, qualification	8.1 g_{RMS}	VSB-30 rocket [47]
shock loads, qualification	$\geq$ 250 g	VSB-30 rocket [47]
WP temperature	$\geq$ 35 °C	passive temp. control
storage temperature	–30 °C ... +45 °C	Swedish winter [47]

Table 2.1: Requirements on laser module of the Rb reference system due to experimental needs and microgravity platform environment

the experiment's apparatus is not required. Still, the heat distribution and passive cooling structures are critical design parameters. Due to the electronics the environment inside the envelope will reach temperatures above 35 °C. The laser module, however, requires active thermal stabilization to maintain frequency stability. Ideally the working point (WP)[2] temperature of the laser module is in the range close to this environmental temperature in order to reduce the load on the cooling system.

2.1.4 Requirements of Laser Modules in FOKUS

Table 2.1 summarizes all requirements on the laser of the rubidium reference system for the FOKUS experiment. Electro-optical requirements refer to the operation of the laser and influence the choice of the laser diode. The mechanical requirements make demands on the package and physical interfaces of the laser module.

Spectral requirements, such as wavelength and linewidth, are determined by the ^{87}Rb transition of the D2 line. In order to stimulate atoms in this state, the laser has to emit at the transition wavelength, which is 780.241 nm (384.230 484 THz) for the D2 line [15], and the lasers full width at half maximum (FWHM) linewidth should be well below the natural linewidth of the transition. Since the natural linewidth of the ^{87}Rb D2 line transition is 6.07 MHz [15], the laser's emission linewidth must not exceed this value. In order to be able to address all allowed transitions of the D2 line, a range of emission frequency of λ_{D2} - 2.369 GHz to λ_{D2} + 4.198 GHz is necessary, resulting in a tuning range of 6.567 GHz. In addition, the tunability of the laser's frequency has to exceed the frequency drift of an unstabilized laser, which also can reach several GHz. With that, a minimum tuning range of 10 GHz would be required to achieve all D2 lines. However, the wider the tuning range, the easier and more stable the

[2]The working point is the set of physical parameters a diode laser is operated at.

frequency stabilization algorithms can perform. Therefore a tuning range of more than 100 GHz seems appropriate. Also this would guarantee a single-mode emission at the desired wavelength not only for one but for various working points and would allow experimental shifting the wavelength in the GHz range.

Several mW of optical output power are required due to losses at the fibre couplers and free-space components located on the spectroscopy module. In order to provide sufficient optical power for the experiment, at least 10 mW optical free-space output power of the laser module should be provided. The maximal injection current of the DFB laser is limited by the electronics of the experimental setup, which only delivers a maximum current of 200 mA. Since the electrical power for temperature stabilization is limited as well, the WP temperature of the laser should be around 35 °C.

Mechanical requirements, such as vibration and shock loads, are given by the launch vehicle, as described above, and are defined in the TEXUS-interface control document [47]. The physical size of experiments operated on sounding rockets is limited. In FOKUS, only a box with a volume of 200 x 100 50 mm^3 is available for the Rb reference system, containing both the laser module and the spectroscopy module. Consequently, the laser module has to be smaller than this. The rocket launch side is situated near Kiruna in Sweden. Since the campaign can be in winter and last several weeks and recovery may last several days, the experiment may be exposed to –30 °C outside temperature.

The Rb reference system with DFB laser and spectroscopy module has the same design and specification as the master laser and reference system of the MAIUS mission, which is described in the following section.

2.2 The Sounding Rocket Mission MAIUS

The first mission to operate an atom interferometer [50] on board a sounding rocket is the MAIUS mission. MAIUS is executed by a project group lead by the "Leibniz-Universität Hannover", Institut für Quantenoptik (LUH), and is part of the project series "Quantengase unter Schwerelosigkeit" (QUANTUS). The main objective of QUANTUS is the production of and research on Bose-Einstein condensates (BEC) in a microgravity (μg) environment. Predecessor experiments of MAIUS as described in [51] and [36] are operated at the droptower in Bremen, Germany. The droptower only provides 4.7 s (in drop configuration) and 9.4 s (in catapult configuration) of μg operation time, thus limiting measurement time and accuracy.

Figure 2.5: Official logo of MAIUS-1 mission

This section will give a brief overview of the MAIUS goals and experimental apparatus, and determine the requirements for laser modules necessary for Rb-BEC based atom interferometry.

2.2.1 Mission Goal

In order to enhance observation time of the experiment and to prepare for future missions of spaceborne interferometry setups the sounding rocket mission MAIUS-1 was initiated. Based on the goals of the QUANTUS experiments the MAIUS mission goals were defined as follows:

- The creation of the first BEC using rubidium-87 in space
- BEC expansion velocity of less than 0.3 mm/s, corresponding to a temperature below one nanokelvin
- BEC observation time of several seconds
- The demonstration of matter-wave interferometry based on a BEC in space.

The MAIUS-1 apparatus is a technical demonstrator and shall prove the ability to perform matter-wave interferometry on board a sounding rocket. This shall serve as a door opener for future space missions, e.g. on board the International Space Station (ISS) or other satellites.

2.2.2 Scientific Methods

In order to understand the requirements of the laser modules that are needed to achieve the mission goals of MAIUS, this section gives a brief introduction in the scientific methods used in this experiment. A more detailed description of the physics and techniques behind matter-wave interferometry can be found in [52].

2.2.2.1 Cooling of Atoms and BEC Creation

Figure 2.6 illustrates the hyperfine structure of ^{87}Rb, the element used in MAIUS.

In order to prepare a BEC, the corresponding atoms have to be cooled. This is accomplished by a combination of optical Doppler cooling with laser beams and trapping of atoms in a magnetic field [53, 54]. Three orthogonal laser beams with their frequency red-shifted to one of the absorption lines (here: D2 line of ^{87}Rb, $|5^2S_{1/2}, F = 2\rangle \rightarrow |5^2P_{3/2}, F' = 3\rangle$, see figure 2.6) are directed onto the Rb atoms. While absorbing the photon energy the momentum of the photon is transferred to the atom effectively causing a friction force on the atom in the direction opposite to the laser beam. Due to the orthogonal directions of the tree laser beams and the fact that the photons, which are emitted spontaneously during the relaxation of the excited atom, are emitted isotropically, the atom loses kinetic energy. Since the temperature of an ensemble of atoms is a measure of the random internal kinetic energy, reducing the kinetic energy of the atoms is equivalent to reducing the temperature of the atoms.

With a low probability, an atom relaxes into the lower hyperfine state $|5^2S_{1/2}, F = 1\rangle$, as depicted in blue in figure 2.6, which removes the atom from the cooling cycle. To re-excite these atoms and to bring them back into the optical cooling cycle, an additional laser with a wavelength tuned to the $|5^2S_{1/2}, F = 1\rangle \rightarrow |5^2P_{3/2}, F' = 2\rangle$ transition of ^{87}Rb is required. This laser is called re-pump laser and has a wavelength offset of + 6.5 GHz with respect to the cooling laser [15]. The re-pumper needs three orders of magnitude

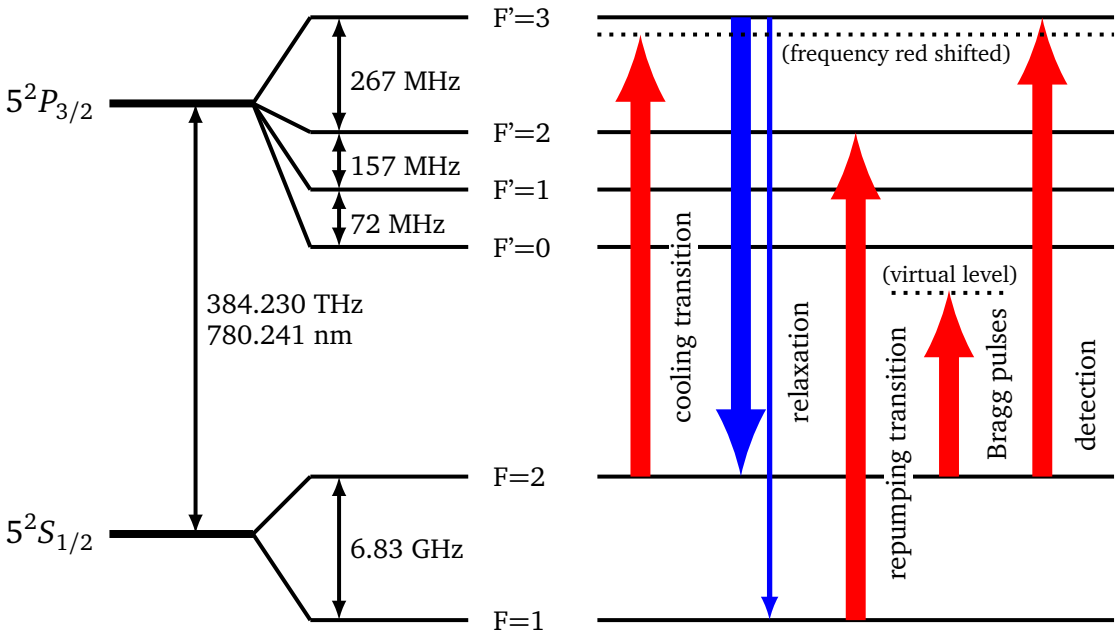

Figure 2.6: Hyperfine structure of ^{87}Rb D2 transition line and frequencies differences. Data from [15]

less optical output power than the cooling lasers due to the low probability of the atoms relaxing to this state.

Cooling, as described above, is limited by heating through spontaneous emission that leads to the Doppler-limit, which corresponds to a temperature in the range of 100 μK [55]. In addition, the atoms will diffuse away from the volume in which the six laser beams intersect because the frictional force is not dependent on position. A restoring force can be introduced by adding a magnetic quadruple field to maintain a defined position of the atom cloud [56]. This technique is called magneto-optical trap (MOT).

In order to create a BEC, temperatures in the nK regime are necessary [57]. The final cooling step is performed with evaporative cooling, firstly described by Hess in 1986 [58]. The atoms which were cooled in the magneto-optical trap (MOT) are transferred into a harmonic magnetic trap. A radio frequency (RF) field, appropriately applied to the atom chip, selectively removes atoms with the highest kinetic energies in the ensemble and the remaining atoms re-thermalize at a lower temperature. When sweeping down the frequency of the RF signal, the remaining atom cloud gets colder until it reaches the critical temperature for phase transition to a BEC.

A more detailed description of the physics and techniques used in MAIUS can be found in [48].

2.2.2.2 Matter Wave Interferometry

BECs can serve as matter wave source for interferometry experiments. Ultra-cold atoms in BECs lose their individual identity and form a macroscopic wave function, as described in the Nobel lectures of Ketterle and Cornell [30, 31]. Very low momentum widths and a macroscopic de Broglie wavelength allow for new levels of interferometric sensitivity, large interrogation times [36] and an enhanced signal to noise ratio (SNR).

A popular method for determination of the gravitational acceleration of the atoms is the Mach-Zehnder-type interferometer [32, 36]. The wave is separated into two paths, travelling for a time 2 T before both paths are superimposed again. Interferometric fringes are caused by the accumulated phase difference between both paths when travelling separately. The matter-wave manipulation is realized with a pair of counter-propagating laser pulses that are detuned either by the recoil energy or by the energy difference of the two ground states. This causes the atoms to oscillate via a virtual transition, which is detuned to a real transition by several 100 MHz in order to avoid spontaneous emission. The length of the laser pulse defines the effect of the laser pulse. A full π pulse causes a population inversion, also called "mirror", a $\pi/2$ pulse creates a superposition of two equal distributed states, a "splitter". A splitter that only shifts the momentum of the atoms is called Bragg splitter. If the atoms oscillate between the internal ground state and momentum state, the splitter is called Raman splitter. In MAIUS a Bragg splitter is realized.

The Mach-Zehnder interferometer is then realized with a sequence of $\pi/2 - \pi - \pi/2$ laser pulses. The Bragg splitter coherently transfers half of the atoms to another state and gives them a momentum kick. The superposition is done by exchanging momentum states (mirror) after a time T and by the coherent recombination after time 2 T with a second splitter pulse.

The number of atoms in each state is determined by absorption imaging. The light of a laser pulse tuned to the $|F = 2\rangle \rightarrow |F' = 3\rangle$ transition, as depicted in figure 2.6, is captured by a charge-coupled device (CCD) camera, revealing the atoms that absorbed the detection light. From the intensity and location of the atoms on the camera the number of atoms and the phase difference can be estimated. With that, acceleration through gravitational forces can be calculated.

2.2.3 Experimental Setup

The apparatus of the MAIUS experiment is divided into the following subsystems:

- The laser system providing frequency stabilized laser beams tuned for laser cooling, interferometry, and imaging,
- The physics package hosting the vacuum chamber in which the BEC is prepared and the experiments are performed,
- The electronics hosting the laser drivers and controls, and the experiment computer,
- The battery module providing electrical power during flight,
- The rocket including the rocket service modules and umbilical.

Figure 2.7 depicts the subsystems and the MAIUS rocket. The scientific payload fits into a structure of 2790 mm length, 500 mm diameter, and 5 mm wall thickness. The rocket engine is the VSB-30, the same rocket engine as used in FOKUS, see section 2.1. The environmental stress applied on the scientific payload by the launch vehicle therefore is comparable.

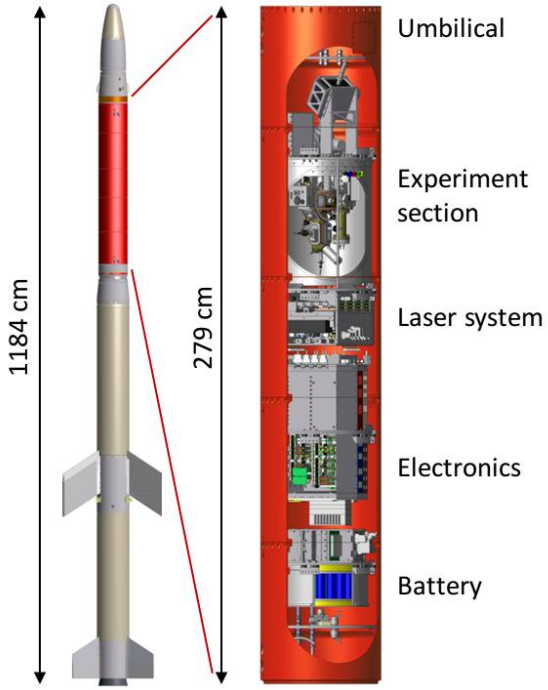

Figure 2.7: Sketch of VSB-30 rocket with MAIUS payload, modified version in [59]

The complete MAIUS payload is described in the work of Seidel [48]. Here, we only focus on the laser system.

The laser system itself consists of several subsystems. It contains the laser modules, the frequency stabilization unit, and the distribution and switching units. The subsystems are connected through fibres and optical fibre splitters. A schematic of the laser system is shown in figure 2.8.

The compact housing of the laser system is designed to maintain the temperature inside as stable as possible. On ground water cooling is provided, during flight a massive aluminium heat sink absorbs the heat produced by the laser modules and their Peltier elements, resulting in a rise of temperature $< 4\,\mathrm{K}$. Each laser module is individually temperature controlled to allow for individual WP settings and to maintain frequency stability.

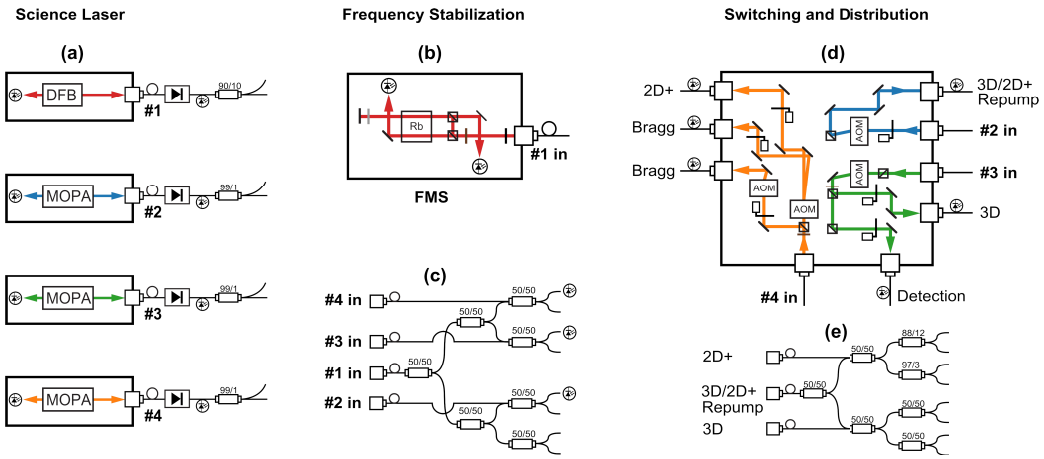

Figure 2.8: Schematic of laser system with four experiment lasers, spectroscopy module, and switching and distribution module, as presented in [60]

There are four laser modules: three of them are science lasers, providing the beams for two-dimensional magneto-optical trap (2D-MOT) cooling and interferometry, three-dimensional magneto-optical trap (3D-MOT) cooling and detection, and the re-pumping during the cooling process. The fourth laser is part of the frequency stabilization unit, comparable to the FOKUS setup, and serves as frequency reference. Two redundancy lasers are provided additionally. If a science laser module fails during the testing on ground, the fibre outputs can be switched without re-assembling the laser system. The science and redundancy laser modules are master oscillator power amplifier (MOPA) modules and are the subject of this thesis. All free-space laser beams are coupled into a polarization-maintaining fibre with a Zerodur-based fibre coupler and are monitored with in-line photodiodes.

The frequency stabilization unit consists of a DFB optical master oscillator (MO) and a Zerodur-based spectroscopy module. Its design is identical to that of the Rb reference system used in FOKUS as described in section 2.1. For frequency stabilization of the three science lasers a fraction of the light of each MOPA is superimposed with light from the DFB master laser on a fast photodetector. The corresponding beat note signals are then used for frequency offset-locking of each of the MOPA laser modules.

The main portion of the MOPA light is tailored to provide the various continuous wave (CW) fields and light pulses required for laser cooling, preparation of a BEC and implementation of an atom interferometer. The switching unit, again, is based on a 5 cm thick Zerodur base plate and contains fibre coupled inputs and Zerodur based free space optics, as described by Duncker in [43]. Several acousto-optic modulators (AOM) and mechanical shutters shape the laser pulses and switch the light from various inputs to various outputs. The power levels of the laser beams in the optical fibres of the switching and distribution module are monitored with in-line photodiodes to identify system malfunctions. Using fibre splitters, the light is then distributed to 11 polarization maintaining fibres guiding the light to the physics package.

Although each MOPA delivers more than 1 W free-space output power the overall laser system provides 115 mW and 110 mW cooling light for the 2D-MOT and the 3D-MOT, respectively. The losses can be explained by imperfect fibre coupling and in-line fibre optics. Still, the provided output power is sufficient for experiment operation.

2.2.4 Requirements on Laser Modules

A summary of requirements of the MAIUS laser modules is given in table 2.2, based on the experimental needs and operation environments.

As in FOKUS, MAIUS targets the ^{87}Rb D2 line transition for atom manipulation. This defines the emission wavelength of the laser modules to be 780.241 nm (384.230 484 THz), as well as the FWHM linewidth of the laser module to be less than the natural linewidth of the transition ($\Delta\nu \leq 6.07$ MHz). The applications targeted for laser light in MAIUS are more versatile than in FOKUS. Still, as explained in section 2.2.2, all optical frequencies required for Doppler cooling and the re-pumping are within the range of the Doppler-broadened Rb D2-line. For the implementation of an atom interferometer a laser linewidth well below the natural linewidth is sufficient. Since the lasers serve multiple purposes (cooling, interferometry, detection), as shown

requirements	**value**	**comment**
	electro-optical	
wavelength (λ)	780.241 nm	^{87}Rb D2 line [15], as in FOKUS
FWHM linewidth	≤ 6 MHz	^{87}Rb D2 line [15], as in FOKUS
tunability around WP	100 GHz	as in FOKUS
optical power per science laser	> 1 W (CW)	complex distribution
optical power of reference laser	> 10 mW (CW)	as in FOKUS
max. power consumption per MOPA	7.2 W	current driver limitation
	mechanical/environmental	
vibration loads	8.1 g_{RMS}	VSB-30 rocket, as in FOKUS
shock loads	≥ 250 g	VSB-30 rocket, as in FOKUS
WP temperature	$\geq 35\,^\circ$ C	system design, as in FOKUS
storage temperature	–30 °C ... +45 °C	as in FOKUS

Table 2.2: Requirements on laser modules in the MAIUS laser system according to the scientific and environmental needs

in figure 2.6, the tuning range of a single laser has to cover different wavelengths. All wavelengths are in the range of some GHz, resulting in the demand of a multiple GHz tuning range. Still, this is covered by the tuning range defined in section 2.1.4. With that, there are no further requirements on the tuning range and linewidth of the laser modules compared to the spectral requirements as defined in FOKUS.

An optical output power of 10 mW for the frequency reference laser is sufficient, as explained in section 2.1.4. According to section 2.2.3, an optical output power in the 1 W range is required for the science lasers, due to the more complex laser switching and distribution concept of the MAIUS experiment. The power consumption per laser, however, is limited to 7.2 W due to limited resources during flight and the limitations of the current driver electronics. In order to relieve the thermal stabilization system the working point temperature of the laser modules should match the temperature of the environment in the payload container, which will be around 35 °C, as in the FOKUS mission. As for FOKUS, the rocket launch side is situated near Kiruna in Sweden, resulting in a possible exposure to –30 °C outside temperature in winter times.

The rocket motor of the MAIUS rocket is of the same type as the motor used for the TEXUS rocket in the FOKUS experiments. Shock and vibration loads on the MAIUS payload therefore are comparable to the FOKUS mechanical environmental requirements.

Chapter 3

Diode Lasers

The previous chapter introduced quantum optical experiments that depend on compact and efficient lasers. This chapter picks up the requirements of the laser modules and presents semiconductor laser technology that is suitable for mobile high-precision optical measurement devices. Semiconductor light amplification by stimulated emission of radiation (laser) diodes are small in size, easy to use, and highly efficient. Combined with other semiconductor diodes and discrete optics, powerful, frequency stable, and frequency tunable laser modules can be created. In this chapter semiconductor diode lasers are introduced, their functionality is explained and some configurations for hybrid laser modules are discussed.

3.1 Concept and Functionality of Diode Lasers

Even before the concept of a photon was introduced by Einstein in 1905 [19], the concept of a powerful "fiery beam" was present in fiction novels, such as in H.G. Wells "The War of the Worlds", 1898 [61]. In 1916 Albert Einstein described the effect of stimulated emission [20], a reversal to photon absorption triggered by an external photon and resulting in the release of a copy of the trigger photon. However, only in 1958 the realization of a laser became feasible by the theoretical description of an "optical microwave amplification by stimulated emission of radiation (MASER)" by Schawlow and Townes [62], followed by the first demonstration of optical lasing by Maiman 1960 [1] where a ruby laser was pumped with a flash-light. Since then, many other lasers have been developed with varying gain materials, such as gas, organic materials, other solid crystals, or semiconductor materials, achieving a wide variety of different wavelengths. They can be pumped with different pump mechanisms, such as coherent or non-coherent optical waves, or electrical current.

The idea of semiconductor laser diodes was first articulated in 1953 by von Neumann, although his manuscript was not published before 1987 [63, 64]. In 1962 the first semiconductor laser, a pulsed GaAs laser at 850 nm, was operated by the group of Hall [65]. The introduction of heterostructures [66, 67] allowed for lower threshold current density and room temperature operation [68]. Today, diode lasers have become a cheap and available component, used amongst others in optical storage units and for

optical data transmission, as well as in science.

Laser diodes can be designed in various ways, such as surface emitters and edge emitters. In this thesis, only edge emitters are discussed. Figure 3.1 defines the spatial orientation of an edge emitting laser diode as used in this thesis in order to be able to describe wave propagation in the semiconductor material according to the optical axis and the p-n-junction. The longitudinal propagation is defined to be in parallel with the optical axis. A lateral wave propagates perpendicular to the optical axis, but still is in plane with the p-n-junction, whereas vertical propagation is perpendicular to both the optical axis and the p-n-junction plane.

In the following section, the functionality and main properties of semiconductor lasers are discussed.

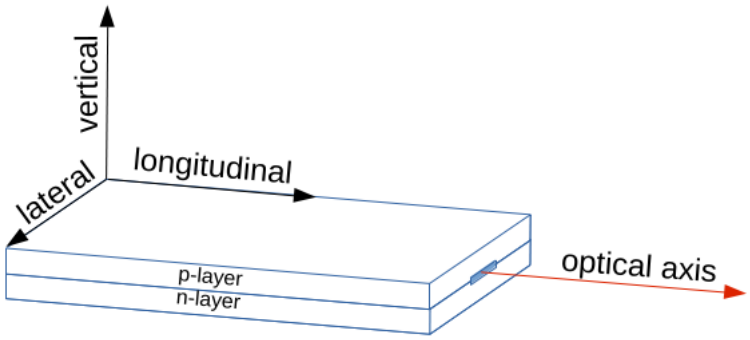

Figure 3.1: Definition of the spatial orientation of an edge emitting laser diode in this thesis

3.1.1 Radiative Transitions and Laser Conditions

Laser devices are based on the principle of stimulated emission [20]. An electron in an excited energy state E_m relaxes to a lower energy state or ground state E_n when interacting with a photon fulfilling the equation

$$\nu = \frac{E_m - E_n}{h} \tag{3.1}$$

where ν is the frequency of the photon and h is the Planck constant. In contrast to spontaneous emission, the photon released to overcome the energy difference between E_m and E_n is coherent with the stimulating photon and cannot be distinguished from the original one. A photon can be absorbed as well, lifting an electron from E_n to E_m state.

The concept of a laser implies two conditions: first, the emission of photons has to exceed the absorption to guarantee constant supply of photons, and second, stimulated emission has to dominate over spontaneous emission to achieve a coherent photon beam. The first condition can be fulfilled when the gain material is set into the state of population inversion by a pump. For the second condition coherent photons have to be kept inside the system while non-coherent photons have to be filtered out. This is realized with an optical resonator that contains the gain medium [69].

3.1.2 Advantages and Application of Diode Lasers

Diode lasers have a wide variety of applications. Since one semiconductor wafer can host thousands of laser diodes, the production costs can be very low. The laser diodes are compact in size, typically some millimetres long and a fraction of a millimetre wide. For population inversion, only electrical pumping is required, although optical pumping is also possible. Internal structures of the semiconductor material, as the facets or internal gratings, can form a resonator. Material combinations of gallium nitride (GaN), gallium arsenide (GaAs), and indium phosphide (InP) allow for wavelengths ranging from 400 nm to 3500 nm [70] and continuous wavelength tuning up to some nanometres is possible. With that, a semiconductor laser is an easy-to-use device, suitable for mobile applications in everyday life, such as in optical communication and laser pointers. Due to its simplicity, compactness, and robustness, they also lend themselves to a wide range of applications in harsh environments such as spaceflight.

Monolithic semiconductor lasers provide an output power up to some ten Watts CW [71] and typically about 100 kHz – 10 MHz FWHM linewidth [72]. Setups with external optical feedback can reach FWHM linewidths in the range of 1 kHz [73]. Still, there are other laser concepts, such as gas lasers and solid state lasers that are superior in terms of output power (CO_2 laser with 2 – 6 kW [74]) or linewidth (ND:YAG laser with sub Hertz linewidth [75]) which are also used in space [76, 77]. These systems are limited in wavelength availability, and they are more complex, bigger, less robust in terms of mechanical stability, and less energy efficient than semiconductor based laser modules. Semiconductor lasers therefore are a future alternative for applications with demands on specific wavelengths on ground and in space.

3.1.3 Basic Properties of Semiconductor Lasers

Semiconductors are solid materials that allow for the movement of charge carriers due to the material composition and doping. Typically, these materials are compound III-V materials as GaAs or InP and provide a p-n-junction, where injected carriers combine permanently. This region of permanent recombining is called *active region*. Electron - hole recombination can be illustrated with the energy band model [78]. Energy bands are discrete energy levels that an electron is allowed to have, whereas band gaps are ranges of energies that are forbidden by the laws of quantum mechanics. At absolute zero temperature the valence band is the highest energy level occupied by electrons, while the conduction band is the lowest unoccupied energy level. In semiconductor materials these energy bands are separated by the band gap energy E_g, the minimal difference between valence and conduction band, as depicted in blue in figure 3.2. The Fermi level, defining the probability of occupation to be 50%, is in the middle of the band gap. E_g is defined by the semiconductor material itself.

For improving recombination efficiency, vertical carrier confinement, as in a double heterostructure, is common. In a double heterostructure a low band gap material is sandwiched between higher band gap materials, as shown on top of figure 3.2b, in order to form a carrier trap. Differences in the refraction index of the sandwiched material also result in a vertical optical waveguide, allowing for fundamental mode

enforcement in vertical direction, like in the red curve in figure 3.2b. The threshold current decreases with the thickness of the active area. Modern epitaxy allows for an active area thickness in the range of the electron's De Broglie wavelength. In this case a quantum well region is generated increasing the internal efficiency of the laser. Lateral carrier confinement can be achieved with a ridge-waveguide structure (index guiding), changing the refraction index profile in lateral direction, and restricted electrical pumping of the waveguide region (gain guiding).

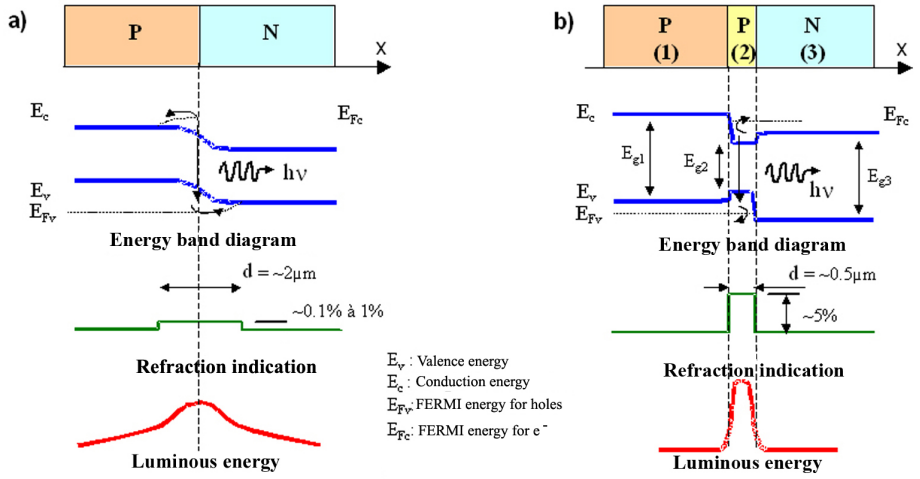

Figure 3.2: Emitting Junctions a) Homojunction. b) Double-heterojunction. In the case of a heterojunction, a better confinement of the photon carriers can be obtained. [79], licence: CC-PD

In longitudinal direction, optical feedback is essential to support stimulated emission. For some types of diode lasers the cleaved facets of the semiconductor material form the resonator mirrors so that the coating of the facets influences the laser properties. Refraction coatings at front and rear facet allow for controlling the ratio of optical output power emitted on both facets. In addition, they also increase the resistance to facet damages. Commonly a low refraction coating at the front facet and high reflection (HR) coating at the rear facet are used to concentrate the optical output on one side of the diode.

The optical feedback in the active region forms a Fabry-Pérot resonator, typically supporting several longitudinal modes due to the macroscopic size of the laser diode. Often, single mode operation is aspired and a wavelength selective element, as will be described in section 3.1.4, is required.

Lattice mismatches between active region and waveguide or cladding lasers can also be used for adjusting the emission wavelength. The emission wavelength also depends on the temperature of the device. With an increase of the temperature T, both the resonator length L and group refraction index $n_{R,g}$ [1] increase, resulting in a higher wavelength, as the modal emission wavelength is proportional to $2n_{r,g}L$ [80]. Also the band gap E_g decreases with higher temperature, and, with respect to equation 3.1, re-

[1] relation between vacuum velocity c_0 and velocity of the wave packet $c_G(\lambda)$ (all emitted modes)

sults in a higher emission wavelength [80]. Fine tuning of the emission wavelength is commonly realized by tuning of the injection current. The injection current defines the carrier density in the active region. A change of the carrier density results in a change of the refraction index $n_{R,g}$ and the temperature in the active region, which is followed by the change of the emission wavelength as described above. In addition, an increasing number of carries results in an increasing number of photons in the resonator which is equivalent to the optical output power.
These effects also can be used for modulating the frequency and amplitude of the electrical field of the output beam. The following sections introduce the mathematics behind semiconductor laser emissions.

3.1.3.1 Mathematical Description

The behaviour and interaction of electrons and photons in a laser diode can be described with rate equations. Common are the rate equations for carrier density n_c and for the photon number S, as described by Petermann [81]. The change of carrier density per unit time is given by the difference between the injection rate of electrons R_i and the electron recombination rate R_{rec} per unit volume in the active region:

$$\frac{dn_c}{dt} = R_i - R_{rec} \tag{3.2}$$

Only a fraction of the injected current I contributes to carrier recombination in the active region, thus, η_i reflects this injection efficiency. We can state for R_i that there are $\eta_i I/q$ electrons per second injected in the active region with a volume V, where q is the elementary electrical charge [82].

R_{rec} is a combination of the spontaneous recombination rate R_{sp}, the non-radiative recombination rate R_{nr}, the leakage rate R_l, and the stimulated recombination rate R_{st}. R_{sp}, R_{nr}, and R_l can be summarized as natural carrier decay. They are defined as number of carriers N per carrier lifetime τ.
The rate of stimulated emission R_{st} describes the electron-hole recombination that is stimulated by photons, generating even more photons. The number of photons S increases by travelling across a pumped gain medium with the length Δz. For sufficient small Δz this can be expressed with

$$S + \Delta S = S e^{g\Delta z} \approx S(1 + g\Delta z) \tag{3.3}$$

where g is the gain of the increasing photons. Taking into account that the group velocity of the photons v_g depends on Δz by $v_g = \Delta z/\Delta t$, the rate of increasing photon number $R_{st} = \Delta S/\Delta t$ can be defined as number of photons S multiplied with the gain g and the group velocity v_g of the photons in the gain medium [82]. Combined, that results in a rate equation for electrical carrier density as follows:

$$\frac{dn_c}{dt} = R_i - R_{sp} - R_{nr} - R_l - R_{st} \tag{3.4}$$

$$= \frac{\eta_i I}{qV} - \frac{N}{\tau} - S g v_g \tag{3.5}$$

The rate equation of photon density S is also dependent on the spontaneous and stimulated emission rate, and introduces the spontaneous emission factor β_{sp}, as well as the confinement factor $\Gamma = V/V_p$, which is the ratio between the volume of the active area and the volume of the optical mode [82]:

$$\frac{dS}{dt} = \Gamma\beta_{sp}R_{sp} + \Gamma R_{st} - \frac{S}{\tau_p} \tag{3.6}$$

$$= \Gamma\beta_{sp}R_{sp} + \Gamma v_g g S - \frac{S}{\tau_p} \tag{3.7}$$

The photon density increases with stimulated and spontaneous emission, although just a small fraction of spontaneous emitted photons contribute to the lasing mode, as expressed by the spontaneous emission factor β_{sp} which is in the order of $10^{-5}...10^{-4}$ [82]. The photon density in the resonator is reduced by photons leaving the resonator or being absorbed internally. τ_p is the average lifetime of a photon in the resonator. Comparing both rate equations from equation 3.5 and 3.7 it is shown that stimulated emission reduces the number of carriers and increases the number of photons.

3.1.3.2 Output Power and Efficiency

The steady state solution of equation 3.5 above threshold ($g = g_{thr}$) can be written as

$$S = \frac{\eta_i(I - I_{thr})}{q\, v_g g_{thr} V} \tag{3.8}$$

As a steady state solution to equation 3.7 and for quite small values for β_{sp} we find the threshold modal gain Γg_{thr} to be

$$\Gamma g_{thr} = \frac{1}{v_g \tau_p} \tag{3.9}$$

With the optical energy been stored in the cavity, E_{Mode} equals S times the photon energy $h\nu$ times the volume of the optical mode V_p. The optical power can be calculated by multiplying E_{Mode} with the energy loss rate through the cavity facets (mirrors). The mirror loss rate can be expressed by $1/\tau_m$ [82].

$$P_o = \frac{E_{Mode}}{\tau_m} = \frac{h\nu V_p S}{\tau_m} \tag{3.10}$$

$$= \frac{h\nu}{q}\eta_d(I - I_{thr}) \qquad \text{for } I < I_{thr}. \tag{3.11}$$

I_{thr} is the threshold current, and η_d the differential quantum efficiency, defined by the number of photons emitted per injected electron [82] that takes the injection efficiency η_i, the lifetime of a photon τ_p, and mirror losses $1/\tau_m$ into account.

Below threshold current, the laser just emits spontaneously, like a light emitting diode (LED). For an injection current $I > I_{thr}$ the carrier density n_c is basically constant

[83], resulting in an increasing number of photons S and a linear relation between injection current and output power.

The dependency of the threshold current on the temperature can be expressed with [82]

$$I_{thr} \propto e^{T/T_0} \tag{3.12}$$

T_0 is the characteristic temperature, given by the material system. T_0 depends on the barrier height, defined by the wavelength of the diode, and the necessary threshold current density. For GaAs diodes with wavelength between 760...800 nm, the value of T_0 is around 100...140 K [71].

The conversion efficiency η of a laser can be described with the ratio between optical output power P_o and the electrical input power P_{in}, whereas the difference between P_{in} and P_o is the dissipated power P_d:

$$P_d = P_{in} - P_o = P_{in}(1-\eta) \tag{3.13}$$

$$= (I^2 R_s + I V_d + I V_s)(1-\eta) \tag{3.14}$$

As reflected in equation 3.14, the input power P_{in} can be expressed depending on the serial resistance R_s of the laser diode, the current-independent serial voltage V_s of the laser diode, and the ideal diode voltage V_d [82].

The dissipation power P_d, in turn, depends on the thermal resistance R_{th} of the diode, causing a temperature rise ΔT in the laser [82]. A simplified description of the thermal resistance takes the thermal conductivity ρ_{th}, the footprint of the laser diode A_{LD}, and the distance of the heat source (active region) to the heat sink H_{vert} into account.

$$R_{th} = \frac{\Delta T}{P_d} \tag{3.15}$$

$$= \frac{H_{vert}}{\rho_{th} A_{LD}} \tag{3.16}$$

With an expression for the thermal resistance, the temperature in the active region can be described with

$$T(t) = \Delta T + T_{WP} = R_{th} \cdot P_d + T_{WP} \tag{3.17}$$

where T_{WP} is the temperature to which the laser is exposed externally.

With rising temperature, the optical output power decreases beyond a certain threshold. This effect is called thermal roll-over [71]. The optical power, as given in equation 3.11, can be complemented with its temperature dependency:

$$P_o = \frac{h\nu}{q} \eta_d e^{-\frac{\Delta T}{T_1}} [I - I_{thr} e^{-\frac{\Delta T}{T_0}}] \tag{3.18}$$

T_0 and T_1 are characteristic temperatures for the device. T_0 was already introduced in equation 3.12. T_1 typically is three to five times the value of T_0. The parameter set $(T_0, T_1, I_{thr}, \eta_d)$ is defined for operation at room temperature. As shown in equation 3.17 and 3.18, higher operation temperatures cause a higher thermal resistance,

which limits the optical output power and increases strongly the temperature in the active region [71]. This underlines the necessity of a good thermal conduction of the high power diodes to ensure low operation temperatures in order to maximize the optical output power.

3.1.3.3 Modulation Behaviour

The stability of a laser diode in terms of optical power and frequency can be influenced by the injection current and the temperature in the environment. Direct modulation of the diode laser is a technique not only used in optical communications but also relevant for frequency stabilization of a laser. In direct modulation techniques, the injection current of the laser diode is modulated, resulting in variation of the carrier density, which causes a modulation of the refractive index, of the temperature in the active region, and of the number of photons in the resonator [84]. A modulation of the photon number S in the resonator influences the optical output power directly, as shown in equation 3.10. Hence, the modulation of the injection current causes a modulation of the output power, and the frequency and phase of the optical field.

The modulation of the injection current also affects the temperature of the active region. We assume the quasi-stationary case

$$I(t) = I_s + I_m, U(t) = U_s + U_m \rightarrow T(t) = T_s + T_m \tag{3.19}$$

where the subscript "$_s$" symbolizes the static bias value whereas the subscript "$_m$" indicates the modulation variation. According to equation 3.13 and 3.17 and the quasi-stationary assumption that $U_m = I_m R_s$, in the first order of current modulation, the temperature modulation can be described by

$$T_m \approx Z_t \cdot I_m \cdot (I_0 R_s + U_0) \cdot (1 - \eta) \tag{3.20}$$

where Z_t is the thermal impedance of the laser diode, R_s is the serial resistance of the laser diode, U_0 is the bias voltage, and η is the conversion efficiency of electrical power into optical power.

Current modulation is directly proportional to temperature changes. The change in temperature changes both, the resonator length and the refraction index as described in [85]:

$$L_m \propto L \cdot T_m \tag{3.21}$$

$$n_{r,m} \propto n_r \cdot T_m \tag{3.22}$$

With rising temperature, the resonator length and the refraction index increase, and hence the emission frequency decreases, since

$$f_m \propto \frac{c}{2 n_r L} \propto -T_m. \tag{3.23}$$

In summary, it can be stated that the modulation of the injection current causes a modulation of the emission frequency due to modulation of the temperature and of the carrier density, as well as a modulation of the output power.

However, modulating the injection current I and thereby inferring a modulation of the carrier density n_c causes a modulation of the refraction index n_r in the active region. The linewidth enhancement factor (or Henry factor) α describes the inverse proportionality between the change in carrier density n_c and the change in the refraction index n_r:

$$\alpha = -\frac{4\pi}{\lambda a}\frac{dn_r}{dn_c} \tag{3.24}$$

Therefore, one has to differentiate between the thermally induced and the carrier density induced modulation on the emission frequency. Thermal effects can only be observed at sufficiently low modulation frequencies. According to Kobayashi [85] maximum modulation frequencies at which thermal effects dominate are approximately at 10 MHz, due to the slow thermal reaction time of the system. For larger modulation frequencies the carrier density influence dominates.

3.1.3.4 Linewidth

The intrinsic spectral stability is limited by the emission of incoherent photons, generated by spontaneous emission, which add phase and power noise to the coherent part of the optical field. This effect was first described by Schawlow and Towns in 1958 [62] and extended by Petermann [86] and Henry [87] to the description of diode lasers. According to them, the linewidth is proportional to the spontaneous emission enhancement factor K, to $(1+\alpha^2)$ (α is the Henry factor, see equation 3.24), the threshold gain g_{thr}, and carrier losses α_m, as well as the inverse optical output power P_o:

$$\Delta\nu_{sp} = \frac{v_g^2 h\nu\beta_{sp}}{8\pi}\frac{g_{thr}\alpha_m}{P_o}K(1+\alpha^2) \tag{3.25}$$

v_g is the group velocity, $h\nu$ is the photon energy, and β_{sp} is the spontaneous emission factor. α_m can be estimated with [81]

$$\alpha_m = \frac{1}{2L}ln\left(\frac{1}{R_f R_r}\right) \tag{3.26}$$

As seen in the equations above 3.25 and 3.26, the linewidth can be decreased by improving the quality of the resonator, e.g. by increasing the resonator length L (an alternative argumentation is delivered by Kojima [88]), the reflectivity of the front and rear facet R_f and R_r and by increasing the output power. Increasing the reflectivity of both facets would reduce the output power, since less photons are able to leave the cavity. Increasing the cavity length does decrease the linewidth proportionally but this comes at the cost of lower efficiency due to decreased carrier density in the cavity [89] for constant injection currents. For applications which demand for excellent spectral stability, laser concepts with an extended or external resonator, e.g. an extended cavity diode laser (ECDL), as described in [90] and [73], can be applied. Still, ECDL setups are more complex and the spectral tuning range typically is limited to the free spectral range (FSR).

3.1.4 Example: Distributed Feedback lasers

For many applications, such as laser cooling or atom interferometry, single frequency emission of lasers is mandatory and a mode selection of longitudinal modes is required. In this work, we focus on distributed feedback (DFB) diode lasers, a widely used laser type, first realized by Kogelnik and Shank in 1971 [91]. In DFB lasers, a longitudinal mode-selective grating is grown along the entire length of the active region, typically implemented in the epitaxial structure of the diode. That results in a periodic modulation of the effective refraction index in the active region allowing only the propagation of two modes adjacent to the Bragg wavelength. The Bragg condition itself forms a stop band where light with this wavelength cannot propagate in the active region.

Distinctive irregularities in the grating and unsymmetrical reflectivity at the facets of the diode are used to prefer only one of the two modes located next to the stop band in the laser. Since the integrated grating behaves like a distributed reflector, discrete mirrors at the facets are not required, the front facet can be anti-reflection (AR) coated. However, the rear facet is commonly high-reflection coated to support only one mode and to direct the output power mainly to the front facet.

The DFB diodes, used in this thesis, are optimized for low linewidth emission and high output power. This is done by optimizing the epitaxial structure of the device, as well as the lateral confinement of the ridge waveguide [92].

3.1.5 Example: Power Amplifier Chips

There are applications which require a CW optical output power in the range of 1 W or more, for example in inter-satellite free space communication [5] or in laser cooling [56], as described in chapters 1 and 2. In order to provide high optical output power in combination with spectrally stable single mode emission, light has to be generated by means of a master-oscillator-power-amplifier concept (MOPA). The output power of the master oscillator (MO), which is optimized for spectral stability rather than for high output power, is amplified by a power amplifier (PA) without the loss of spectral stability. The spectral behaviour of the original MO beam shall not be influenced by the amplification.

This demand can be satisfied with a semiconductor optical amplifier (SOA) [93], a semiconductor chip having a similar structure as a Fabry-Pérot laser. The population inversion is, again, created with electrical pumping, but both facets of a SOA are AR coated so they do not serve as resonator. The MO laser beam is coupled into the rear SOA facet and triggers stimulated emission while travelling through the gain material of the SOA. By doing so, the output power of the beam increases by a gain factor of g_{usat}. However, with increasing input power of the signal beam, the gain amplification decreases. This effect is called gain saturation and is caused by depletion of the carriers in the active region at the signal's saturation power. The gain of a saturated amplifier can be described with

$$g_{amp} = \frac{g_{usat}}{(1 + \frac{P_o}{P_{o,sat}})} \tag{3.27}$$

with g_{usat} as the unsaturated small signal gain, P_o as the output power of the amplifier and $P_{o,sat}$ as the saturation power. The saturation power of the output beam is defined as output power where the gain of the amplifier has reduced by 3 dB compared to small signal gain [93] and is marked in figure 3.3 with $P_{o,sat}$.

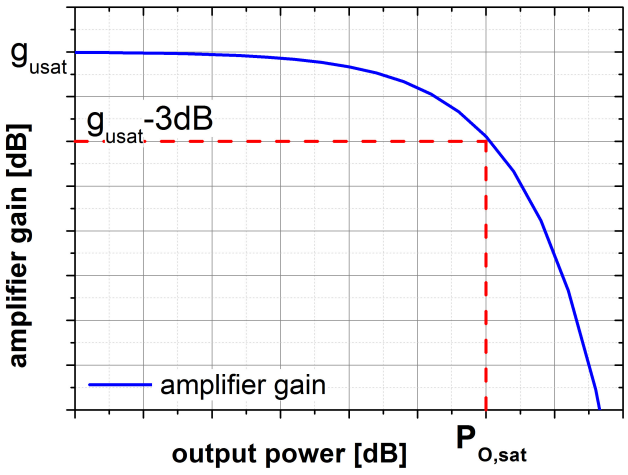

Figure 3.3: Example of amplifier gain vs. output power

The saturation power $P_{o,sat}$ is limiting the output power of the amplifier and is given by [93]

$$P_{o,sat} = \frac{A}{\Gamma}\frac{h\nu}{\tau}\frac{(n_c - n_{c,0})}{g_m} \tag{3.28}$$

with A/Γ denoting the amplifier mode cross-section area, with $h\nu$ describing the photon energy, τ giving the lifetime of the carriers, the material gain coefficient g_m, and the difference of the carrier density n_c and the transparency carrier density $n_{c,0}$.

Since the saturation power is limiting the output power, a large saturation power is desirable. According to equation 3.28 the saturation power can only be increased by increasing A/Γ at a given wavelength and material system, since the photon energy $h\nu$ includes the wavelength, and the gain coefficient g_m, and carrier densities n_c and $n_{c,0}$ depend on the material system of the laser diode. τ saturates for high injection currents. Only A/Γ is given by the design of the active region of the amplifier. An approach to increase the saturation power by design of the amplifier will be described in paragraph 3.1.5.2.

To every output saturation power $P_{o,sat}$ an input saturation power $P_{i,sat}$ can be assigned. For a signal input $P_{in} > P_{i,sat}$ the amplifier is saturated, the gain of the amplifier is reduced. $P_{i,sat}$ is dependent on the coupling efficiency of the input power into the amplifier and can be influenced to a certain degree by the design of the laser module.

Operation of the amplifier in saturation reduces the rate of spontaneous emission and thereby reduces amplified spontaneous emission (ASE) noise. In addition, the saturation of gain causes the suppression of small fluctuations in input signals power, which improves the power stability. However, this is a disadvantage when the amplitude of

the master oscillator is modulated on purpose to implement a power modulation. The amplitude modulation will be suppressed as well.

At large population inversion the emission of spontaneous photons, the ASE, increases as well. The incoherent and non-polarized emission is amplified and adds noise to the power and phase of the optical field. This limits the number of amplifiers that can be cascaded, e.g. in optical communication applications. In high power operation, high power density, both in the gain medium and at the facets, can exceed the damage threshold of the SOA [94], causing catastrophic optical damage (COD). With passivation of facets [95] these damages are less probable nowadays. However, the optical output power of the SOA is limited by design as shown in equation 3.28.

As described in section 3.1.3.2 and shown in equation 3.18, the output power decreases with increasing temperature in the active region. Due to high SOA injection currents, which contribute quadratically to the dissipated power over an ohmic resistor as shown in equation 3.14, thermal roll-overs [93] often can be observed when working with SOAs. Sufficient thermal conduction of the diode therefore is necessary to dissipate the accumulated heat in order to defer the thermal roll-over effect.

In the following sections two designs of a SOA are discussed, addressing both the question of output power and of beam quality.

3.1.5.1 Ridge Waveguide Amplifiers

The ridge waveguide (RW) amplifier is a typically 4 mm to 6 mm long double heterostructure chip with a mode selecting grating and with AR coated front and rear facets. The waveguide can be tilted [96] or partially bent [97] to suppress the effect of facet reflection and prevent the chip from starting to act like a laser itself.

Due to the strict confinement of the optical wave in the chip, the output beam characteristics are expected to be nearly Gaussian. This is an advantage, when the output beam has to be coupled into a fibre. With a Gaussian beam profile and compatible beam widths most of the beam power can be coupled into the fibre, and thus result in a good coupling efficiency. Thermal exposure of the coupling components, which is caused by non-coupled beam power, is reduced the better the beam profile of the laser matches the in-coupling interface of the fibre. The good beam parameters are achieved with the mode confining by the RW, which is typically only few micrometres wide. However, this comes at the cost of limited saturation power $P_{o,sat}$, as the size of the active area is reduced, and with that A/Γ, as denoted in equation 3.28. The achieved output power of a RW amplifier therefore is reduced as well.

3.1.5.2 Tapered Amplifiers

Expanding the gain region towards the output facet as described in [98] is a common approach to increase the saturation power $P_{o,sat}$ of an SOA as it increases A/Γ, shown in equation 3.28. Figure 3.4b illustrates a tapered amplifier with a RW pre-amplifier on the right side of the optics-block. The RW shaped pre-amplifier can be included

for filtering the incoming modes, providing a Gaussian input for the tapered amplifier section and thereby improving the beam quality of the amplifier.

Still, a tapered gain section results in the deterioration of carrier confinements and potentially allows for other modes than the fundamental mode, because the lateral carrier confinement decreases with increasing width of the active area. That results in a decreased beam quality, and decreases the fibre coupling efficiency. In addition, the difference in divergence of the output beam between the fast axis and slow axis increases due to the elliptical shape of the active area at the output facet, which makes beam collimation more complex.

3.2 Monolithic and Hybrid MOPAs

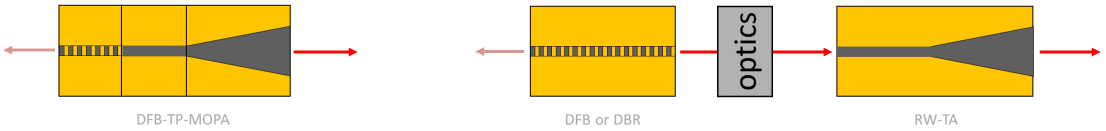

(a) Monolithic MOPA (b) Hybrid MOPA

Figure 3.4: Concept of monolithic and hybrid semiconductor laser MOPA

Compact design is a key benefit of diode lasers and qualifies them for mobile applications. As discussed in section 3.1 single mode, narrow linewidth lasers can be processed and diode lasers can achieve an output power larger than one watt CW, fulfilling the requirements listed in table 2.2. Combining a mode selective section with a gain section on one chip, as shown by Fiebig in [99] and explained in [100], will reduce complexity of the system and decrease the production costs radically. This approach is called monolithic integration and is depicted in figure 3.4a. However, this system suffers from poor spectral stability due to reduced lateral carrier confinement in the gain section and internal feedback, which disturbs the mode selection of the chip. Although diodes with high CW output power of 1 W and a narrow linewidth of 1.4 MHz were reported in [101], the continuous tunability is reduced by spectral unstable behaviour for low injection currents.

An alternative approach to monolithic integration is the hybrid integration of laser diodes, as shown in figure 3.4b. A master oscillator (MO) is decoupled from the amplifying section, optical feedback from facets or internal section transition is prevented by an external optical isolator. The laser beam emitted by the MO is coupled into the active region of a semiconductor amplifier, keeping the spectral behaviour but increasing the optical output power. This assembly increases the complexity and costs of the laser module. However, it preserves the spectral properties of the MO, providing a laser system with high output power, narrow linewidth, and large continuous frequency tuning range.
For that reason, we chose a hybrid MOPA concept for our laser sources.

Chapter 4

Concept and Assembly of Micro-integrated Laser Modules

In order to obtain laser modules with an optical output power larger than 1 W in combination with an emission frequency stability in the lower MHz range, as demanded in table 2.2, we combine the spectral properties of DFB laser diodes with semiconductor power amplifiers. In addition to the electro-optical properties, the mechanical stability and compactness of the laser modules are important to guarantee operation of the laser module in the harsh experiment environment. In the first section of this chapter the concept and design of the laser modules, which addresses all requirements given above, will be introduced. The second section tackles the demands for reproducibility and documentation of the assembly process by explaining the overall processes in general and the process of integration of optics in the laser modules in particular.

4.1 Concept and Design of the Hybrid Integrated Laser Modules

This section introduces the design of the laser module that shall be used in the FOKUS and MAIUS missions. In the design two aspects were taken into account, the functional aspect, reflected in the electro-optical design, and the physical aspect, presenting the mechanical structure and interfaces of the laser module.

The electro-optical design discusses the choice and arrangement of the semiconductor diodes and optical components, such as optical isolator and lenses. This design is chosen to fulfil the electro-optical requirements of the laser modules.

The mechanical structure satisfies the mechanical and environmental requirements of the laser modules, hosts the optics and provides the electrical and mechanical interfaces. A fully integrated laser module is shown in figure 4.1. The paper clip next to the laser module gives an idea of the size of the module, which has a footprint of $80 \times 25\,\mathrm{mm}^2$.

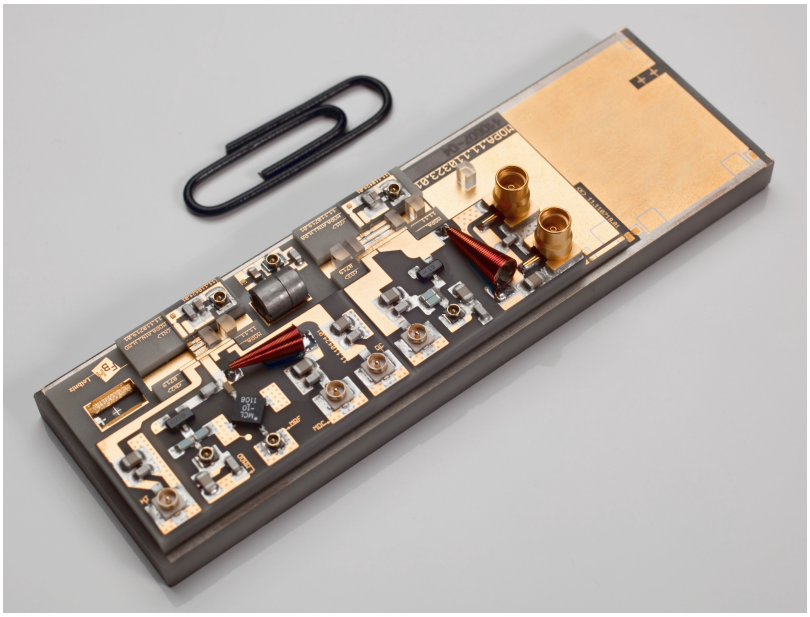

Figure 4.1: Hybrid integrated MOPA module on AlN MIOB with integrated electrical interface. A modified version published in [102]

4.1.1 Electro-Optical Design of the Laser Modules

Laser modules with a separate optical master oscillator (MO) and optical power amplifier (PA) are called MOPAs. The optical design of the MOPA module is shown schematically in figure 4.2, featuring, from left to right, an optical isolator, collimation lenses for the rear output of the MO, the MO-DFB diode itself, collimation lenses for the front output of the MO, a second optical isolator, coupling lenses for the rear input of the PA, the PA itself, and collimation lenses for the PA front output. The upper part of figure 4.2 depicts the lateral view of this ensemble, meaning the view from above. The vertical view in the lower part of the figure shows the projection from the side of the optical ensemble.

As described in section 3.2, the hybrid integration approach allows the integration of optical isolators, protecting the DFB laser from optical feedback and thus from distortion of the propagating wave. In order to guide the beam through the optical isolator, the beam has to be collimated to be able to propagate through the aperture of the isolator device. To couple the beam into the amplifier chip the beam has to be focused onto the active area of the chip, meeting the divergence properties of the chip. The output of the amplifier is collimated to compensate for the PA chip's divergence and prepare the output beam for further usage. The beam collimation and isolation at the rear output of the DFB laser make an additional output available that can be used for monitoring of the condition of the DFB laser, or as an additional light source with low output power. The beam guiding, such as collimation and focussing, is done by the miniaturized glass lenses. The choice of the lens parameters, such as the numerical aperture and the focus length, depends on the aimed beam diameter and the divergence angles of the diodes.

In the following section the laser and amplifier diodes are introduced, and the cho-

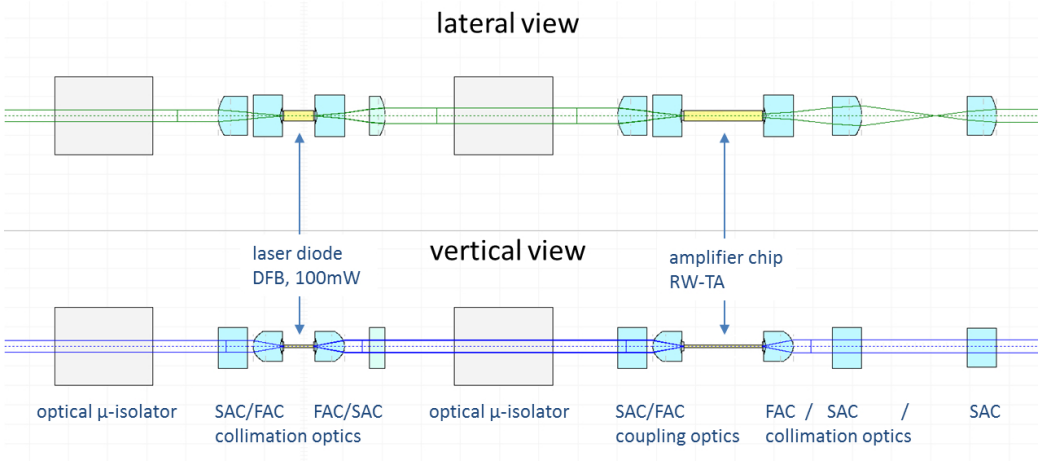

Figure 4.2: Lateral and vertical view of optical configuration on MOPA

sen lenses and optical isolators are presented.

4.1.1.1 Laser Diodes

In this work, we use DFB diodes optimized for narrow linewidth emission at 767 nm and 780 nm, designed and processed at the "Ferdinand-Braun-Institut, Leibniz-Institut für Höchstfrequenztechnik" (FBH). Emission wavelengths below 870 nm are demanding for the designing and the epitaxial processes of GaAs based semiconductor lasers. The high aluminium (Al) content in the cladding results in oxygen contamination during the growing steps of the grating, as described in [92]. In addition, the material composition and thickness of the grating layer has to be adapted to obtain non-absorbing gratings for wavelengths below 870 nm.

MO diodes with an optimized grating are fabricated as DFB diodes with a RW for better lateral wave confinement. DFB diodes with two different lengths, 1.5 mm and 3 mm, were tested. The 1.5 mm long diodes fulfil the linewidth requirements for laser cooling. 3 mm diodes, however, can achieve an even narrower linewidth [89] at the cost of higher threshold currents and decreased efficiency.

The facets of the DFB lasers are coated with AR coating on the front facet and 95 % reflection coating on the rear facet. That results in a higher optical output power at the front facet compared to the rear facet, because 95 % of the photons are reflected at the rear facet. The asymmetrical coating of the facet also supports the mode selection of one of the two competing DFB modes.

In addition to the DFB diodes amplifier chips for 767 nm and 780 nm with a RW pre-amplifier section, serving as mode filter, and a tapered section of an optical amplifier (TA) for power boost, are fabricated. Both facets of the amplifier chip are AR coated, because photons are supposed to pass the amplifier and shall not be reflected at any facet.

In order to be able to perform an optical simulation of the MOPA design it is necessary to know the divergence angle and the beam waist at the chips facet for both DFB lasers and PAs. The simulation verifies the design and choice of lenses, as described in

the next section.

The beam propagation properties of the diode lasers used in this work are listed in table 4.1. With these properties it is possible to estimate the lens parameters, required to manipulate the beam propagation in a hybrid laser module, as shown in figure 4.2 and described in the following section.

Table A.1, located in in appendix A, lists the laser and amplifier diodes integrated into laser modules and used in this thesis.

Type	$\Theta_{vertical}$ front/rear	$\Theta_{horizontal}$ front/rear	$d_{0,vertical}$ front/rear	$d_{0,horizontal}$ front/rear
DFB	34.8 ° / 34.8 °	17.6 ° / 17.6 °	1.6 μm / 1.6 μm	3.2 μm / 3.2 μm
RW-TPA	38.8 ° / 40.8 °	13.0 ° / 23.2 °	1.6 μm / 1.4 μm	4.4 μm / 2.5 μm

Table 4.1: List of beam propagation properties of DFB lasers and amplifier diodes used in FOKUS and MAIUS modules. Values behind "/" refer to rear facet properties.

4.1.1.2 Optical Components and Design

In hybrid laser modules, beam guiding optics are required to couple the beam, which is emitted by the MO, into the amplifier chip, and to collimate the beam outputs. The beam propagation, illustrated in figure 4.2, was simulated beforehand with the software WinABCD [103]. The simulation helps to identify the lens types and lens properties that qualify for micro-integration and to find the approximate positions of the lenses along the optical axis within the spatial limitations of the MIOB. The MIOB, described in the next section, provides a 2.2 mm wide and a maximal 30 mm long channel for the placement of the optical components. This limits the size of the lenses and the size of the beam. Other frame conditions for the simulation are the laser diode divergences, as listed in table 4.1, and the aimed beam diameter of 0.6 mm providing a power content of 95 %, resulting in a free aperture of the lenses of > 1.2 mm. A free aperture of more than the double of the beam diameter is recommended to avoid clipping and deformation of the beam at the edges of the optics.

The simulation revealed that cylindrical lenses are suitable to compensate of the different horizontal and vertical divergence angles of the semiconductor diodes, when aiming for a round beam shape, because the horizontal axis and the vertical axis can be collimated separately. Another advantage of cylindrical lenses, compared to round lenses, is, that they provide a degree of freedom (DOF) in positioning of the lens. The vertical position of a lens forming the horizontal beam propagation can be chosen freely as long as the beam is within the free aperture of the lens. This DOF can be used for mounting of the lenses in the MIOB. Shrinkage in the direction of the DOF of the adhesive that is used to fasten the lens into the MIOB will not affect the beam shape as long as the lens is not tilted. Since there are no adhesives with zero percent of shrinkage, this aspect has to be taken into account in the design as well.

In this work the beam guiding is accomplished by cylindrical plano-convex microlenses, provided by the manufacturer Ingeneric. The lenses feature a numerical aperture of 0.8 and an aspheric design to avoid optical aberrations. The front and the rear

facet of the lenses are AR coated for a wavelength of 780 nm. The fast axis collimator (FAC) takes over beam shaping in guiding in the vertical plane, while the slow axis collimator (SAC) is guiding the horizontal plane of the beam. To shape the beam, there is always a combination of FAC and SAC required. The output of the amplifier is collimated with a three lens system, including a FAC and an SAC-SAC-telescope in order to form a round, non-astigmatic beam. The rear output and guiding within the MOPA is realized with a FAC-SAC pair. Figure 4.3 shows a detailed picture of the MO main beam collimation and isolator. In this picture, the rear output is not collimated.

The simulation shows a vertical beam diameter of 0.583 mm behind the DFB front output, formed with the FAC lens FAC-08-900. However, for the slow axis collimation of the MO, the nominal beam diameter could not be realized with the available lenses. Since both the FAC and SAC lens have a thickness of 1.5 mm, the minimal focal length of the SAC should be > 2 mm, since the two lenses cannot overlap physically. A focal length > 2 mm results in a beam diameter of 0.8 mm. The horizontal diameter of 0.814 mm was generated with the CLY-PL-CX-2.67 lens with $f = 2.6$ mm and coupled into the amplifier with an ACYL-F2.1 lens with a $f = 2.1$ mm. For output collimation we again chose the FAC-08-900 for FAC collimation and pick a telescope configuration with ACYL-F2.1 and ACYL-F2.5 lenses in order to form a symmetric, round beam with a simulated diameter of 0.628 mm. The beam diverges to 0.8 times 0.83 mm in 300 mm distance to the amplifier.

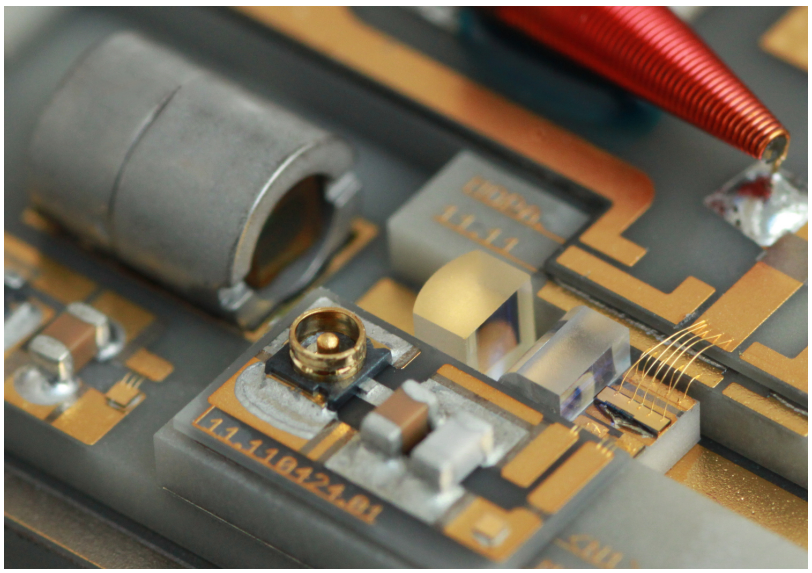

Figure 4.3: Detailed picture of a MOPA: DFB on submount with temperature sensor, coax connector for temperature sensor, collimating lenses and optical micro-isolator

The optical isolators are placed at the rear and at the front output of the DFB diode, as illustrated in figure 4.2. In the front output path, we use a semi-double stage micro-isolator, type I-78-LM-SD-1.4-4, provided by Isowave. It has a specified isolation of > 55 dB and a specified insertion loss of < 7 dB. Pre-integration characterization of the isolators confirmed these specified values, revealing an average isolation of 56.8 dB and an average insertion loss of 6.3 dB. The components inside the isolators are tilted by

4° to prevent back reflection of the beam. The clear aperture is 1.4 mm, fitting twice the size of the nominal beam diameter.

Due to high insertion losses of the micro-isolators and low output power available at the rear output of the MO, a single stage isolator I-780-MM-1.4-4-WP-0 provided by Isowave with only <4 dB specified insertion loss but also only > 35 dB isolation was chosen for the auxiliary beam output.

An issue with the optical micro-isolators is that the power which can pass the isolator without thermal degradation of the isolation is limited due to heating of the thin film components inside the isolator. The manufacturer recommends a maximal power of <50 mW per 1 mm^2 aperture per isolation stage, allowing for only 30 mW input power with a beam diameter of 0.6 mm (and 57 mW with d=0.8 mm) in the isolator. Our DFB diodes provide an output power up to 120 mW. The optical linewidth decreases with high output power and the tuning range increases. Since we are aiming for a large tuning range and narrow linewidth emission a limitation of the injection current of our DFB lasers in order to meet the recommended maximal optical power input into the isolators would restrict the performance of our laser system. However, the experimental verification of the isolation with an input power in the range of 100 mW has shown that the isolators maintain their performance beyond the specified input power range.

4.1.2 Structural Design of the Laser Modules

The optics described above are mounted on a ceramic micro-optical bench which is clamped onto a copper (Cu) mount adapter that provides mounting holes for system integration. A MIOB with a mount adapter is shown in figure 4.4. Both MIOB and Cu mount adapter are described in this section.

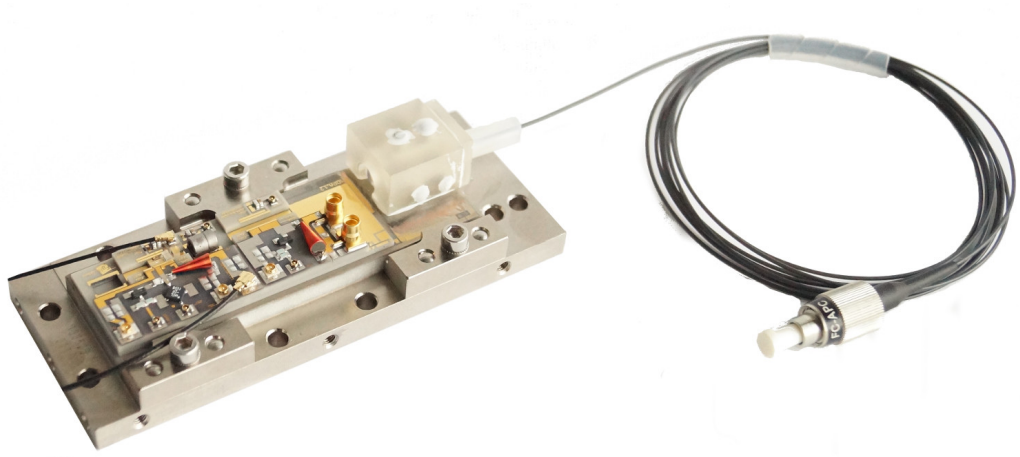

Figure 4.4: MIOB with integrated DFB and fibre coupling on a Cu mount adapter (Image courtesy of V. Schkolnik [104])

4.1.2.1 Micro-optical ceramic bench and Submounts

In order to design a laser module that fulfils the mechanical requirements, listed in table 2.2, a structure is chosen that hosts the electro-optical and optical components by omitting movable parts and being small in size. A good thermal conductivity of the structural material is required for thermal stabilization of the laser diodes and to dissipate heat generated by the thermal resistance of the diodes, as explained in section 3.1.3.2.

High stiffness is very important for the structure hosting the optics and the laser diodes. A deformation of the MIOB may result in a degradation of the MO-to-PA coupling. This in turn may cause a reduction of the output power, excess ASE or a degradation of the PA output beam quality. Further, a potential deformation will deflect the PA output beam which may result in a degradation of the fibre coupling efficiency (see section 4.1.3.2). All the effects mentioned above reduce the available optical output power and potentially degrade the spectral performance of the laser module. A deformation-induced variation of the output power could be observed with previous modules described in [105], when applying asymmetric pressure on the only 1 mm thick AlN MIOB.

To overcome the issues mentioned above, the MIOB, designed for this work, is based on a 4.5 mm thick AlN base plate which is 25 mm wide and 80 mm long. AlN was chosen for its good thermal conductivity of close to 200 W/mK and its high stiffness with a Young modulus of > 300 GPa. On top of this AlN base plate several functional AlN ceramic plates are mounted, proving frames for isolators, mount structures for lenses, and the electrical interface. The ceramic plates are soldered on top of each other in sequenced processing steps. Some layers, especially the ones hosting the electrical interfaces, are lithographically structured in thin film processes, allowing for the implementation of printed circuit board (PCB)-like electrical networks and the mounting of discrete electrical components directly on board the MIOB ceramic.

The laser and amplifier diodes are mounted on AlN submounts, which also are lithographically structured so they can host a temperature sensor (see section 4.1.3.1) and allow for separate control of different sections of the diodes. In addition, the submounts come with a layer of gold tin (AuSn) solder to support p-down mounting by minimizing the risk of shortening p- and n-contact of the flipped diode by seeping out of surplus solder. DFB diodes are mounted with the p-side pointing up, as illustrated on the left in figure 4.5, in order to reduce mechanical stress close to the active region that could disturb the stable single mode propagation and may reduce the polarization purity. The amplifiers, in contrast, are mounted with the p-site facing the submount, also called p-down mounting and illustrated on the right in figure 4.5, to reduce the thermal resistance between the active volume and the heat sink and with that to allow for maximum heat extraction.

There are individual submounts for each chip length allowing to interface both main and rear output of a diode. Submounts for p-up mounting have a height of 1.0 mm. P-down submounts have a height of 1.125 mm to compensate for the bulk height of the semiconductor diode itself so the beam height on the MIOB can be maintained.

The MIOB provides a channel for optics integration, formed by rails to hold the FAC

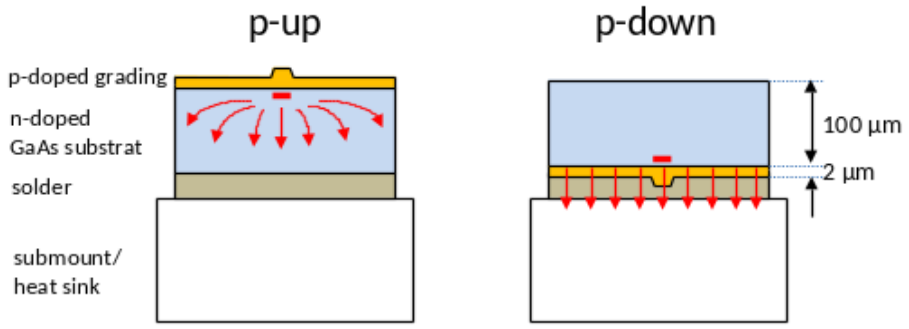

Figure 4.5: Concept of p-up and p-down mounting

lenses in lateral direction, and a plane bottom to host the SAC lenses. The submounts are adhesively bonded to the bottom of this optical channel as well.

The MIOBs and the submounts are manufactured by an external manufacturer. Integration of submounts and optics as well as wire bonding are carried out at FBH.

4.1.2.2 Electrical Interface on MIOB

The MIOB hosts several electrical interfaces to address multi-section laser and amplifier diodes, as well as several sensor read-out interfaces. The electrical interfaces and sensor read-outs are organized on AlN based PCBs, they are highlighted in figure 4.6. The electrical interface PCBs provide gold finished bonding pads to be able to connect the laser and amplifier diodes, mounted on submounds. The submounts also provide bonding pads, they are connected to the interface PCBs by wire-bonding. The bond wires, connecting the submount with the electrical interface are clearly visible in figure 4.3 on the right hand side of the lenses. The short bonding wires left to the beam axis connect the temperature sensor. The longer bonding wires right to the beam axis connect the laser diode to the electrical interface of the MO.

The MIOB can be connected to supply electronics with miniature, UHF coaxial connectors. Most of the coaxial sockets are Radiall micro-miniature coaxial (MML) interfaces, as depicted in figure 4.3, left to the lenses. An exception is the TA injection current interface, where micro-miniature coaxial (MMCX) sockets for higher current capability were chosen.

There are in total five electrical interfaces on two interface PCBs. This enables the supply of a maximum of three sections of a MO chip, and two sections of an amplifier chip. Two of these interfaces also provide a modulation capability, allowing modulating the injection current, one for the MO injection current, and the other one for modulating the amplifier section of the PA diode.

Figure 4.7 depicts the modulation interface of the MO, featuring a DC port for modulation operation (MDC), and two ports for a modulation signal, the RF modulation port (MRF), capable of radio frequency (RF) modulation, and the transistor modulation port (MMOD), suitable for low frequency (LF) modulation frequencies. The MMOD port delivers the gate voltage to a common source transistor circuit, reducing the injection current, supplied by MDC, for the laser every time the transistor opens. The transis-

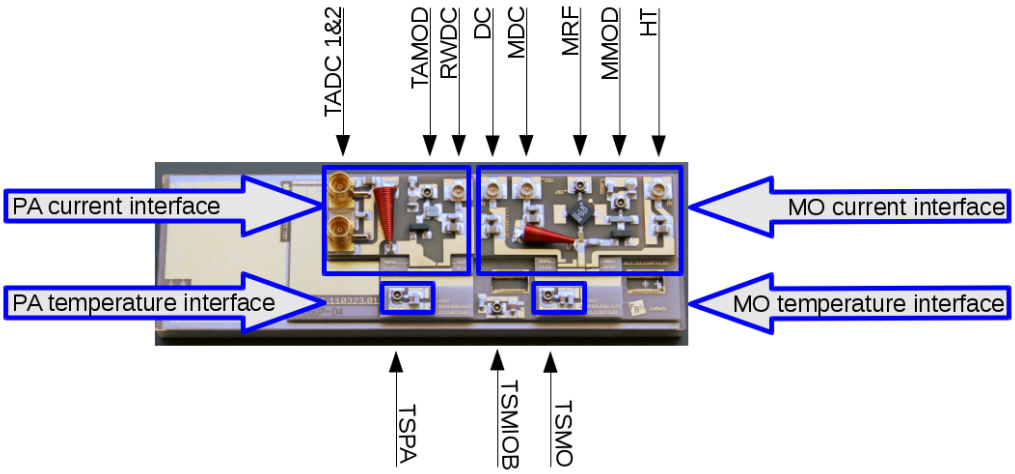

Figure 4.6: Electrical interface provided by a MIOB. TADC: DC injection current of PA gain section, TAMOD: modulation of PA gain section, RWDC: DC injection current of PA pre-amplifier section, DC: DC injection current of MO (bypassing modulation electronics), MDC: DC injection current of MO (to be modulated by modulation electronics), MRF: RF modulation port, MMOD: LF modulation port, TSMO: MO temperature sensor port, TSMIOB: MIOB temperature sensor port, TSPA: PA temperature sensor port

tor T1 is a N-channel junction gate field-effect transistor (JFET), normally open, when no distinctive gate voltage is applied. The modulation method of reducing the injection current allows very low modulation frequencies down to direct current (DC) range and is therefore capable of LF modulation. In addition, the laser diode is protected against reverse biasing, since the current direction cannot be inverted accidentally. Still, the modulation bandwidth is limited by the bandwidth of the transistor which corresponds to about 500 MHz. The MMOD input provides a pull-down resistor R1 that defines the gate input of the transistor to be low when there is no signal connected to the MMOD port.

The MRF port adds an attenuated modulation voltage onto the DC injection signal. The input signal is attenuated by a factor of 10 to minimize the risk of accidentally reversing the bias of the laser diodes injection current. Over-driving the input at MRF can cause a reverse bias at the laser diode, which may lead to fatal damage of the diode. However, the direct combination of the modulation signal with the DC signal allows for modulation frequencies in the GHz range. Both, the MDC and MRF port together with the output interface for the laser diode, form a simple bias-tee, including the inductor L1 and capacitor C1. L1 protects the current source attached to the DC current port MDC against disturbance caused by the applied modulation frequencies. Whereas the capacitor C1 protects the signal generator connected to the MRF modulation port against the DC loads. In addition there is the inductor L2, filtering RF frequencies, supplied by the MRF port, from the drain of the LF-modulation transistor T1. With these protection components, the MRF port contains a high pass filter formed by C1 and the resistance of the laser diode, opening at 1 MHz. But since the MMOD port is available for LF modulation, the high pass filter does not minimize the functionality of

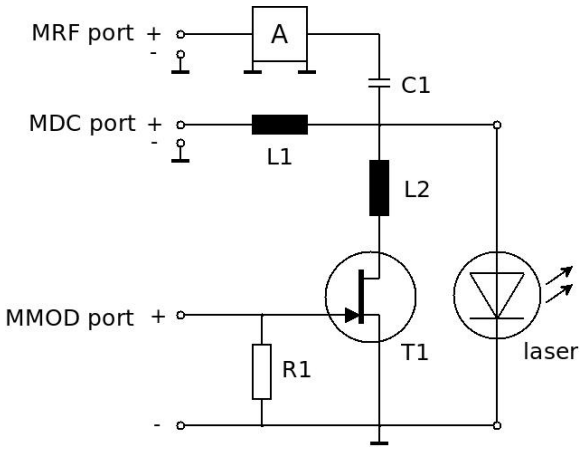

Figure 4.7: Electrical interface on MO-MIOB: the DC port supply can either be modulated with a common source circuit (MMOD with T1) or with a bias-tee path (MRF).

the interface.

The electrical interface PCB for the MO also provides an additional port that is not connected to the modulation ports. This port simply is called DC (in contrast to MDC) and guides the applied signal directly to the laser diode. This port does not contain any filters and therefore is used when the injection current is modulated externally or if a multi-section chip requires the excitation of an additional amplifier section.

The third supply input of the MO interface PCB is marked with "HT". It can be used to supply another section of the MO, act as redundant input, or drive a heater section, if the MO device provides one.

The current supply PCB of the amplifier hosts a DC port for the RW pre-amplifier section (RWDC) and the high current interface TADC for the gain section of the amplifier, tolerating several Ampere of current. The DC port for the tapered section (TADC) interface provides two MMCX connectors to share the current load and to increase the effective diameter of the current guiding pins and cables. The injection current of the gain section of the amplifier can be modulated by applying a signal to the modulation port for the PA gain section modulation (TAMOD). The current modulation is again realized with a common source transistor circuit, comparable to the MMOD port on the MO interface PCB as illustrated in figure 4.7.

The complete schematic of the electrical interface PCBs and a component list is provided in appendix B.

In addition to the electrical interfaces of the laser diodes the MIOB provides three temperature sensor read-outs for temperature monitoring close to the laser diodes and on the MIOBs optical bench. The temperature read-out interfaces host a MML connector and two filter capacitors to read out the value of the temperature sensors. In addition, they allow for mounting of an extra sensor measuring the temperature of the MIOB close to, but not on the submount, in case there is no temperature sensor available on the submout. The temperature read-out PCBs of the MO, the PA, and the MIOB are identical in design.

4.1.2.3 Mechanical Adapter

To be able to mount the ceramic MIOB in the assembly station, characterization assembly, or users system, a mechanically stable and thermally conductive adapter is required. This adapter is referred to as conductively cooled package (CCP) and is made of Cu for its high thermal conductivity of 400 W/mK. The surface is protected against oxidation and minor mechanical damage with a 3 μm thick layer of galvanically applied nickel (Ni). A CCP is depicted in figure 4.8. To ensure thermal contact and to avoid bending of the ceramic body upon mounting, the top and bottom surfaces of the CCP have a specified planarity of 10 μm maximal bow over full length and width – a challenge in production of the CCP. Therefore, the CCPs were manufactured with electrical discharge machining (EDM) and individual characterized with a 3-dimensional optical surface profiler. Each CCP has a serial number, which is engraved by laser, highlighted in red in figure 4.8.

The thermal expansions of Cu (16.5 μm/mK) and AlN (5.3 μm/mK) do not match. Therefore the MIOB cannot be mounted on the CCP by adhesive bonding, since thermal expansion differences e.g. between storage and operation at WP temperature, would add mechanical stress to the system, causing deformation or even loosening of the MIOB. The AlN-MIOB therefore is mounted on top of the CCP by three vertical clamps, positioned on the long edges with dowel pins and screws to with a well-defined torque is applied. The clamps are also manufactured by EDM, guaranteeing a chip free, well-defined round contact surface where the clamp presses on the MIOB. Loosening of the screws, both of the ones holding the clamps and of the screws attaching the adapter to the experimental system, is prevented by SCHNORR safety spring washers.

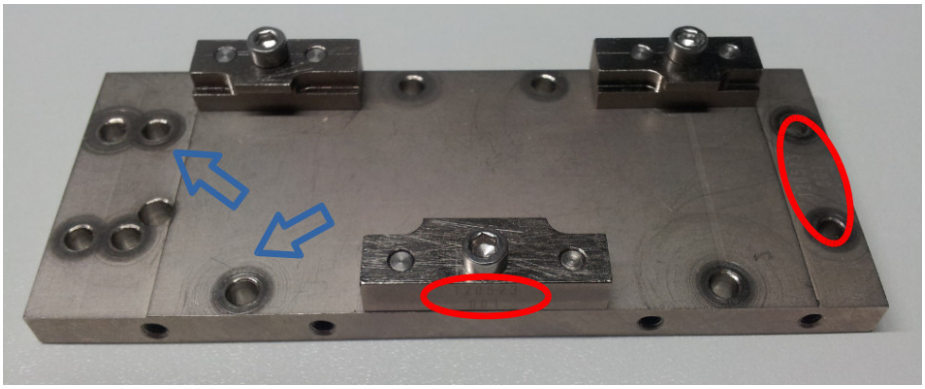

Figure 4.8: CCP with serial number (marked red) and imprints of the safety spring washers (marked blue)

4.1.2.4 Housing with Electrical Interface

Although the MIOB already hosts coaxial interfaces, it is recommended to convert the MML and MMCX connectors to SubMiniature version A (SMA) connector or some other standards common in laboratories. Since most supply electronics neither provide a MML nor a MMCX interface, an adaptor is required. Apart from the availability of common connectors like SMA, a conversion on the MML interface is useful due to the limited

length of available MML cables, which are not longer than 100 mm. Another reason is the fact that MML sockets are specified only for approximately 10 re-connections. To limit the chance of damage to the laser module or degrading performance due to exceeding the number of re-connects, it is recommended to keep the MML cables attached to the MIOB and mount them to an electrical adapter. In addition, long levers, formed by cables, can cause the sockets to break off from the MIOB.

In addition to providing an electrical adaptor within < 100 mm of the sockets of the MIOB, the optical setup needs to be protected against dirt, physical impact, e.g. induced by user, as well as for streams of air that may cause frequency distortion. To protect from both, the electrical adaptor is integrated into a housing package, as shown in figure 4.9. In our package design, we are able to integrate the adaptor PCBs directly on the sides of the CCP, forming the long side covers of the housing. The electrical adaptor side panels of the housing are depicted in figure 4.9. The adaptor PCBs provide various SMA interfaces and a Sub-D interface, compatible to ILX temperature controllers used in our laboratory.

The cover lid and side panels of the short side of the housing are formed by Al parts and provide holes for the optical beam, as well as screw threads for the mounting of the long side panels. The Al parts have a black anodized finish in order to prevent reflection and reduce the scattering of light inside the housing, which may disturb the laser.

In the MAIUS and FOKUS laser system, this housing is not necessary since the laser systems in both experiments are optimized for low weight and are designed to provide one housing solution for all laser system components.

(a) (b)

Figure 4.9: Housing package with integrated electrical adaptor (a) on left side, and (b) on the right side of the optical axis

4.1.3 Features of the Laser Modules

4.1.3.1 Temperature Monitoring

Since the emission wavelength of the DFB laser depends on the temperature, the temperature of the DFB laser has to be stabilized in order to minimize drifts in wavelength.

A feature of the MIOB is the integration of multiple temperature sensors, both on the submount of the MO, on the submount of the PA, and on the optical bench of the MIOB. The MO sensor close to the DFB chip and the MIOB sensor left to the isolator are depicted in figure 4.3.

The output of the sensors can be used as control value for temperature stabilization. The sensor on the MO submount will deliver a temperature value very close to the actual temperature of the MO diode, enabling a more precise temperature control of the diode.

The sensor at the PA submount also is an indicator for the coupling efficiency of the to-be-amplified beam into the PA. Since the input energy is constant, the lesser photons are injected into the optical amplifier, the more of the incoming photon energy has to be converted to heat, as long as the amplifier is not saturated.

With the MIOB sensor the thermal resistance of the MIOB can be estimated. In addition, it serves as a redundancy sensor for temperature controlling and offers clues on the temperature gradient between MIOB and the diodes on the submounts.

4.1.3.2 Fibre Coupling

To be able to use the laser beams in the experiments described in section 2.1 and 2.2, fibre coupling of the modules output beam is required.

To minimize fluctuation of the power coupled into the fibre due to thermal expansion of the mounting structures, the fibre coupler and the laser optics are placed on the same mount, the MIOB. With that, miss-alignment due to thermal expansion of the integrated materials are reduced to the expansion of the miniaturized optical components themselves, and the system will not suffer from different expansion rates of different mounts. This increases the stability of the system.

In addition, an on-board coupling is a more compact solution than external coupling. For this reason the MIOB provides a 20 mm long and 25 mm wide section behind the optical bench on the base plate. The fibre coupler itself was designed and is integrated by the project partner "Universität Hamburg", Institut für Laserphysik (UHH), details are described in [43]. A fibre coupled MIOB is shown in figure 4.4.

4.2 Laser Module Assembly Process Flow

In the previous section all components of a laser module were introduced. The following section deals with the assembly of the components in order to finalize the laser module.

A reproducible integration of mobile optical setups is a complex process with several in-between-characterizations and qualification tests as shown in figure 4.10. Before integration all active and passive optical components pass through a qualification process, as described in chapter 5. The most complex one is the semiconductor diode chip qualification, see step 1.1 in the general process flow chart in figure 4.10, including spectral and power characterization as well as a burn-in phase for 120 h. The optical microisolators (step 1.2) are characterized optically for isolation and transmission, and their

facets are controlled for defects. The MIOBs (step 1.3) are cleaned and undergo a visual and electrical inspection, and for the CCPs (step 1.4) the surface condition and deformation (bow) of the surface are determined and evaluated. When all necessary components are qualified, the integration process can be initiated, starting with the optical master oscillator integration (step 2) before continuing with the optical power amplifier integration (step 3).

The integration of the optical components into the MIOB takes place at an especially designed assembly station, described in section 4.3.1. After the selected DFB laser is integrated into the MIOB, the module is placed on the assembly station and connected to the current source. The laser diode is tested electrically before the collimation lenses and the isolators are integrated. The spectrum and optical power of the laser is recorded, which serves as reference of the performance of the laser during the assembly of the optical components close to the DFB laser. After integration of each optical component group the output power and the optical spectrum is recorded. If the spectrum of the DFB laser shows any deviation of the previous spectral behaviour during the MO assembly, the integration process is aborted and the chip is replaced.

After the integration of the collimation lenses of the MO and the optical isolators, the selected PA chip is placed into the module. Since the PA mounting is done in another laboratory, the module has to be temporarily removed from the assembly station. After re-installation into the assembly station, the electrical connections of the chip are tested before the coupling and collimation optics are integrated.

After integration of all required optics, the module undergoes extensive electro-optical tests, step 4 in the process flow in figure 4.10, in order to document that all electro-optical requirements can be fulfilled. Chapter 6 presents the corresponding measurement methods and representative results achieved with the laser modules in this step. If a module does not perform according to the requirements, single optical components have to be manipulated or replaced.

In a last visual inspection, step 5, the module is controlled for visual defects, such as deformed or broken bond wires, and dirt. Particles are removed and broken bond wires may be replaced. Pictures taken in this step belong to the documentation as well as the measurement results of steps 4.

The module is then mounted into a transport box, the packaging in step 6. The electric cables remain attached to the module in order to reduce de- and re-connecting the sockets and to avoid damage of the electrical interfaces. Finally the modules are delivered to the project partners together with an individual user manual, including documented performance values (step 7).

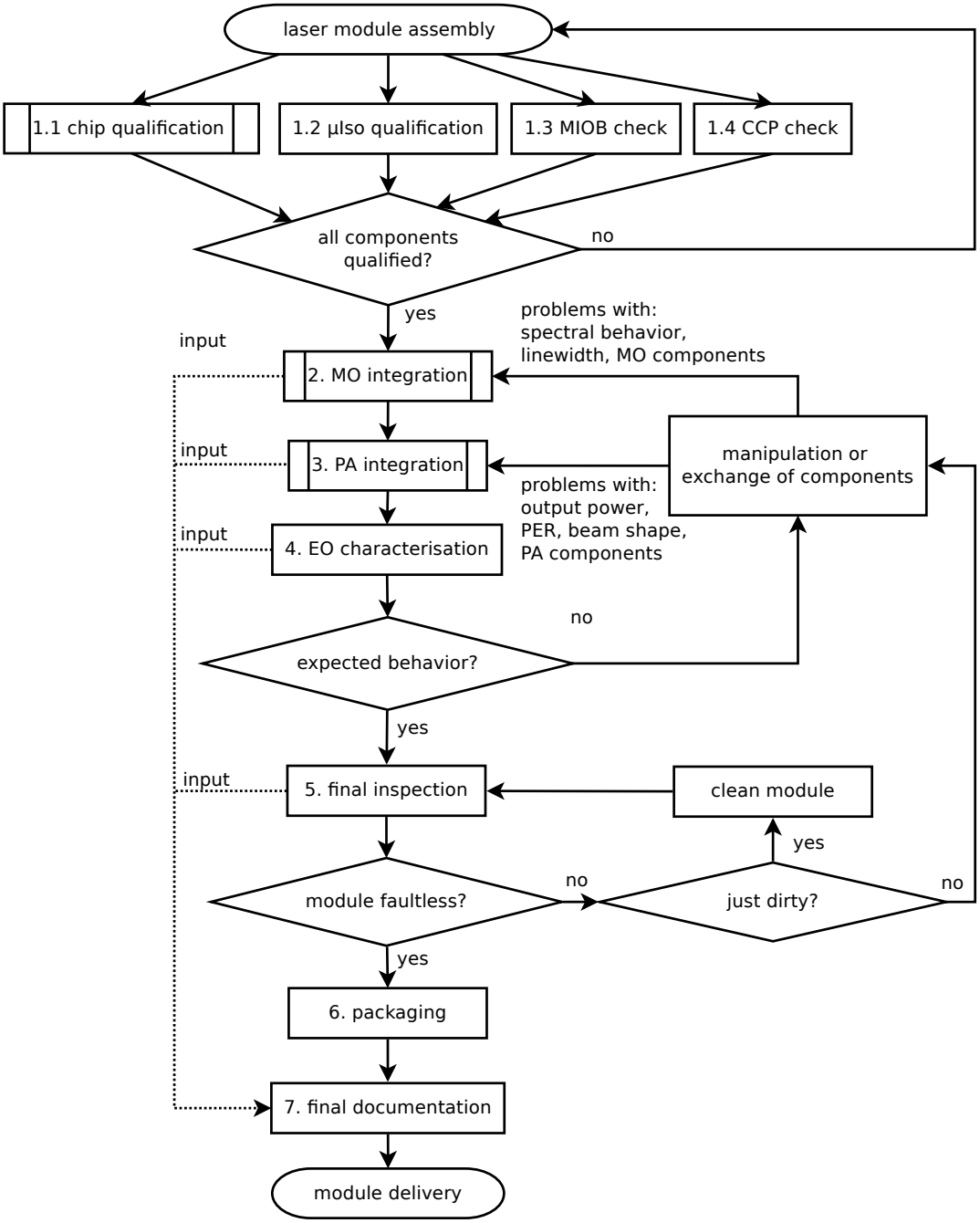

Figure 4.10: Overview of laser module integration process flow

4.3 Integration of Optics

The assembly process is divided into two sub-processes, denoted as "2." and "3." in the process flow chart in figure 4.10. The first process is the assembly of the optical master oscillator, including beam collimation and the integration of the micro-isolators. The second process is the integration of the optical power amplifier and the beam shaping of its optical input and output. The assembly procedure follows a process definition, defining the steps to be taken and documentation to be carried out. Each assembly step is accompanied by visual documentation and characterization of the electro-optical properties. This enables the detection of problems early in process and allows for analysis and corrective measures in case of potential malfunctions.

4.3.1 Assembly Setup

The optics assembly setup is depicted schematically in figure 4.11. All optical components, except for the submounts that host the semiconductor chips, are integrated onto the MIOB with this setup. The positioning of the lenses and isolators is carried out with a Physics Instrument Hexapod F-206.S, a manually controlled robot with a spatial and angular resolution of 0.1 μm and 2 μrad, respectively. The components are kept in place with a vacuum interface made of Macor, a glass-ceramic with very low thermal expansion to keep the position when exposed to ultra violet (UV) light or heat. The Hexapod host an electrical interface to connect the electro-optical components to electrical supply sources. Also a Peltier element in integrated to the setup to stabilize the MIOBs temperature. The assembly station (ii) also hosts a microscope and a cold-light source for monitoring the manipulation of the components via the robot. The UV light source Omnicure 1000 with two light pipes each providing 230 mW of light is curing the adhesive after active alignment of the optical components.

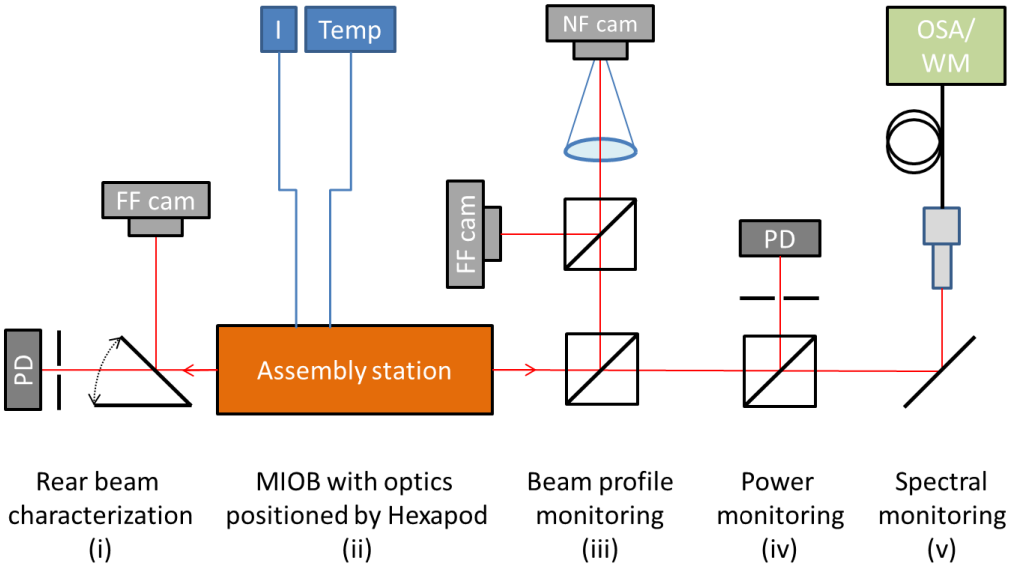

Figure 4.11: Schematic of assembly station and monitoring

The beam, exiting the assembly station, is monitored with two cameras, positioned within one Rayleigh range of the collimated beam according to the optical simulation, described in section 4.1.1.2. A fraction of the beam is separated with beam splitters and guided to two cameras in order to monitor the beam profile, see (iii) in figure 4.11. One camera monitors the far field while the other camera, positioned in the focus of a bi-convex lens with a focal length of 10 cm, maps the near field of the laser beam. The near field camera is used for beam collimation which is done by minimizing the spot size on the camera, the far field camera can be used for monitoring the actual beam diameter and shape as well as power content in the central lobe.

Besides the beam monitoring, the assembly setup allows for simultaneous characterization of electro-optical properties of the laser, namely the optical output power, recorded with a power meter (iv), optical spectrum, recorded with an optical spectrum analyser (OSA) and the emission wavelength, monitored with a wavemeter (v). In addition, path (iv) provides pinholes with a diameter of 1 mm at a distance of 1 m from the laser for adjusting the beam position on the MIOB with an accuracy of 63 mrad. For this pinhole aiming, the power passing the pinhole is maximized. This beam guiding facility guarantees a reproducible pointing of the beam on the MIOB.

The rear output of the laser can be collimated using the pinhole and far field camera installed at the rear site of the assembly station, denoted by (i). Since the rear output is only used with photodiodes or shall be dumped directly to avoid scattered light, focussing on a distant point is a sufficient method of collimation. The camera for rear collimation has a distance of 2 m from the chip.

4.3.2 Integration of Master Oscillator Optics

The integration of the optical master oscillator optics is divided into several steps, as shown in figure 4.12. After burn-in and pre-characterization, as described in section 5.1, a qualified chip on submount is chosen. Again, the facets of the chip are controlled visually because they could be affected by dirt or damage during pre-selection process. If the facets passed visual inspection again, the submount is placed into the MIOB, aligned along the rails framing the optical path of the MIOB. A thermal adhesive with bonds the submount assembly to the MIOB. The chip on submount is than wire-bonded to the electrical interface of the MIOB.

With the DFB laser integrated and connected, the MIOB is installed into the assembly station, described in the previous section. The MML cables are attached to the electric interface ports driving the DFB laser and reading the available temperature sensors. These cables remain on the module to minimize mating stress on the connectors. During the first electrical test of the module, the voltage required to drive 2 mA through the chip is documented as reference value. The voltage typically is in the range between 1 V and 2 V. If not, the cable connection or bond wires do not work properly and have to be checked. The minor current of 2 mA was chosen to prevent damage to the diode in case there is a slack joint in the connection.

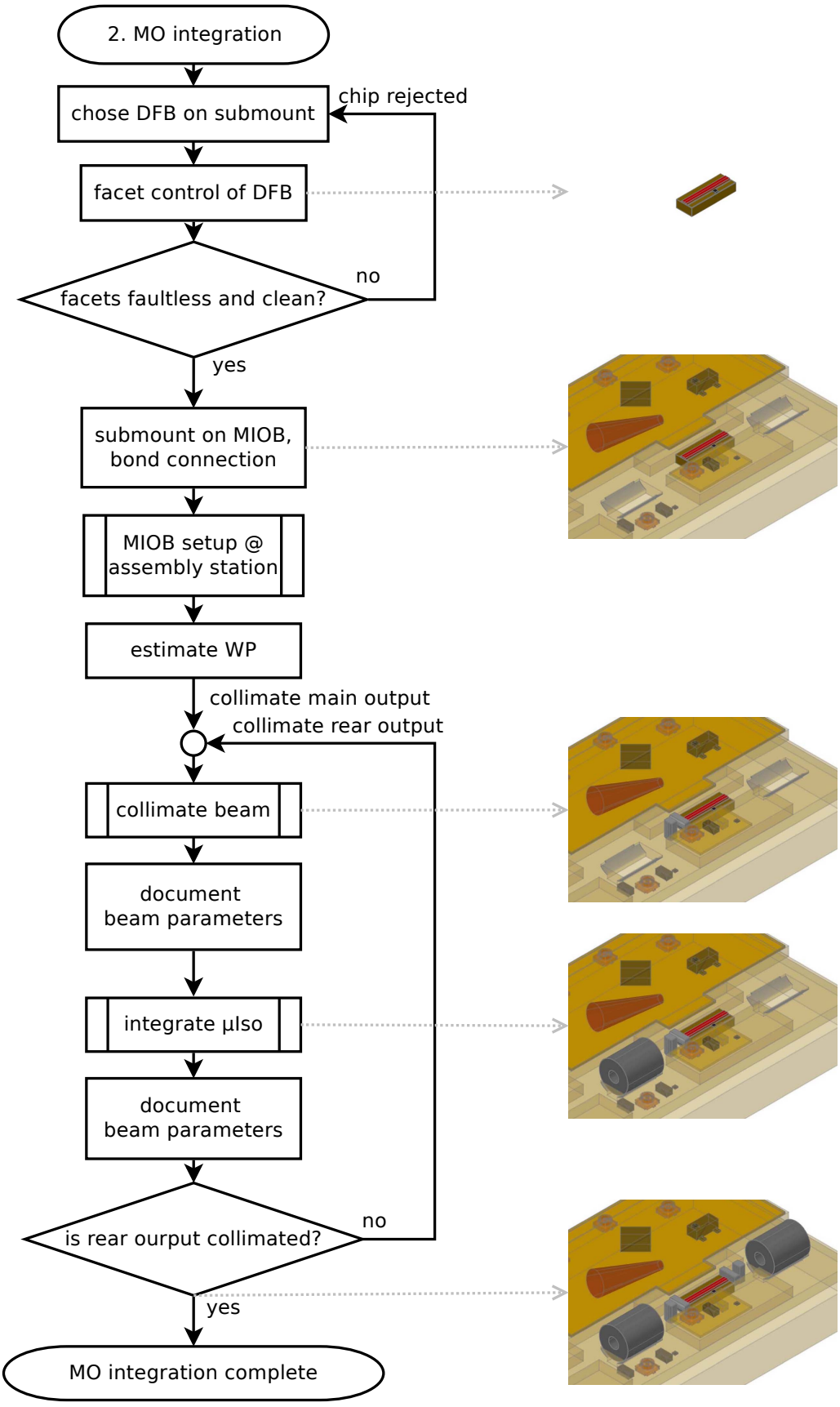

Figure 4.12: Overview of master oscillator optics integration

With inserting a temporal collimation, the working point (WP), including DFB injection current and operating temperature, is determined with help of the wavemeter, according to the targeted wavelength. In this thesis the targeted wavelength is either 767 nm or 780 nm. During the integration process, the DFB laser is operated at the identified WP to optimize the alignment of the optical components at the same conditions the laser module will be operated at later on.

The collimation process of the beam starts with adjusting the FAC, followed by the SAC. The lens position is adjusted actively by minimizing the spot size of the beam on the near field camera. The near field camera, as shown in figure 4.11, is positioned in the focus of a lens. This lens reverses the effect of the collimation lens, causing collimated rays to converge to a spot [106]. The spot size will be at its minimum when the beam rays are collimated because rays diverting from the parallel direction of propagation will be projected aside the focus point. Since the FAC and SAC lenses are cylindrical lenses, they only manipulate either the vertical and horizontal beam propagation, respectively. The pointing of the beam is adjusted by maximizing the power fed through the pinhole in 1 m distance to the chip. Before curing of the FAC, the vertical size of the near field beam projection is recorded for different FAC-lens positions along the optical axis, as shown in figure 4.13a, to document the optimal position. The parabolic shape of the values in figure 4.13a also hints that there are further distortions in the beam line blocking or bending the light and that the lens is not tilted.

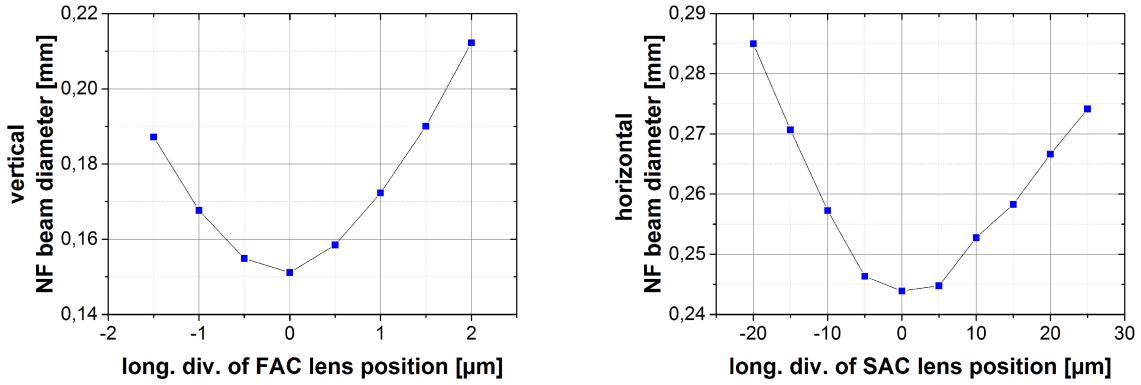

(a) FAC (b) SAC

Figure 4.13: Variation of near field beam diameter by varying the position of the (a) FAC and (b) SAC lens. The beam is collimated at the Zero-position in this plot.

FACs are glued laterally to the rails of the MIOB to be able to adjust the vertical position of the lens and to minimize distortion effects, introduced by the shrinking of the adhesive under curing. However, non-symmetrical curing may wrap the FAC-lens, causing miss-alignment. The positioning of the UV-arms for curing therefore has to be chosen carefully. All optical components are glued with a low out-gassing UV adhesive that has been used for space applications before. The adhesive is cured with approximately 120 Ws/cm^2.

The SAC lens is placed the same way the FAC was adjusted, only, they are glued directly onto the bench to allow lateral position adjustment. A sweep of the SAC lens position along the optical axis with resulting beam diameters on the near field (NF) camera is shown in figure 4.13b. Variations of the SAC position in the μm range along the optical axis do not affect the beam diameter as strong as the FAC position. This can be explained with the longer distance from the source and the larger focal length of the SAC lens.

After collimation of the DFB, the optical output power, emission spectrum, and voltage for various injection current settings are recorded. This documents the DFBs behaviour after collimation and ensures that the DFB has not been damaged or disturbed under the integration process. Additionally, the beam profiles of the far and near field are saved as reference.

The next step addresses the integration of the micro-isolator. The isolator is placed into the corresponding cut-out in the MIOB and is coarsely adjusted by rotating it around the optical axis of the beam in order to maximize the power propagating through the device. For precise alignment, a PBS, oriented to reflect the nominal polarization, is placed on the bench. The power behind the PBS is minimized by rotating the isolator before the isolator is glued on one side to the bench. The other side of the isolator is only accessible after turning the MIOB by 180 ° around the vertical axis. The optical power behind the PBS is documented after each curing step to ensure that the isolator's alignment is maintained throughout the adhesive bonding. After integration of the isolator, optical power and spectrum are recorded again and compared with the measurement before isolator integration. The power behind the micro-isolator is reduced by 3-4 dB compared to the output power of the laser diode, due to the insertion loss of the isolator. The spectral characteristics should be maintained.

The rear output of the laser is collimated by minimizing the spot size on a far field camera, placed in a distance of 2 m to the chip and illustrated in figure 4.11. The output power of the rear exit is documented before and after integration of the rear micro-isolator. The integration of the rear isolator is comparable to the integration of the front isolator.

With the front and the rear output collimated, the micro-isolators in place, and the beam characterized, the MO integration is complete. The following step would either be the integration of the PA, described in the next section, or the integration of the fibre collimator, performed by the UHH and mentioned in section 4.1.3.2. A module without optical amplifier can be used for applications where less output power is required, e.g. the master laser in MAIUS or the laser source in FOKUS.

4.3.3 Integration of Amplifier Optics

For applications with a demand on output power higher than 20 mW, an amplifier can be integrated. The sub-processes for integration of the amplifier are shown in figure 4.14. The amplifiers undergo a burn-in and pre-characterization process and get qualified with the criteria defined in section 5.1.

The selected amplifier-submount assembly are aligned, adhesively bonded, and wire-bonded the same way as the oscillator chips. Heating the module up to 100 °C during the wire-bonding process of the submount does not affect the positioning of the optical components that have been integrated during the previous integration steps, as long as no mechanical stress is applied to them.

After re-installing the MIOB onto the assembly station and connecting the MML cables for the RW pre-amplifier section, for the tapered main-amplifier section, and for the temperature sensor located on the amplifier submount, an electrical test of the laser module and its connection to the current drivers is performed. This is done by logging the voltages that is applied to the diodes while driving the MO diode and the RW section with 2 mA and the TA section with 20 mA. These values are reference values for electrical tests and should be in the range between 1 V and 2 V. The value of the MO diode has been recorded earlier (before the MO lenses and isolators were integrated) and is now compared to this reference value. If the voltage is out of range, the electrical connections have to be checked.

Before the beam emitted by the MO can be coupled into the amplifier, the output of the amplifier has to be collimated, in order to be able to monitor the amplifiers output power. This is required to judge the quality of the coupling.

Since the beam profile of a semiconductor amplifier in ASE operation differs in its characteristics compared to when a seeding beam is coupled into the amplifier, the positioning of the collimating lenses cannot be finalized before establishing an in-coupling into the PA. Therefore, a temporal collimation of the output is required. This is done with an aspheric round lens and a cylindrical SAC lens to compensate for the differences in divergence. The round lens has an optimized height, so it can be placed on the bench but achieves roughly the vertical position of the FAC. Both lenses are placed loosely on the bench to obtain a fairly good collimation and will be removed for final collimation after finishing the coupling process.

The next step aims at coupling the MO emission into the PA chip. For an efficient mode coupling between the MO output and PA input the beam parameters of the MO output have to be matched to the beam parameters of the PA input. This is done by focussing the beam with appropriate lenses as determined in the optical simulation (see section 4.1.1.2) into the active region of the RW section.

For coarse alignment of the coupling lenses the RW section of the amplifier chip is operated as a photo detector and the photo current, generated by photons stimulating the doped materials in the active volume, is monitored. The alignment is achieved by maximizing the photo current.

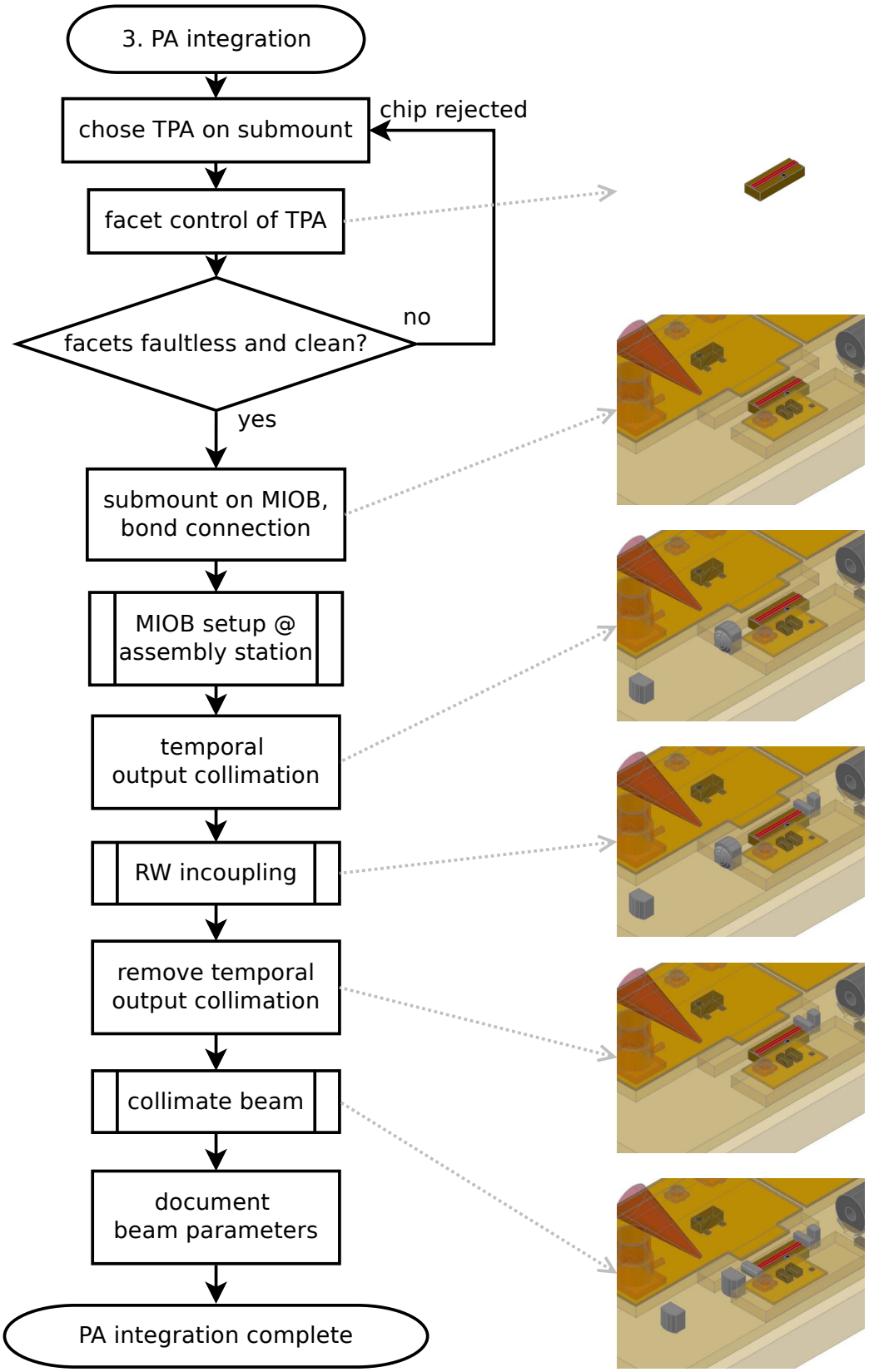

Figure 4.14: Overview of power amplifier optics integration

The beam in-coupling process starts with the SAC that is put down onto the bench in order to ensure that the MO beam roughly overlaps with the active area at the input of the PA chip. The SAC position cannot be finalized until the FAC is in place, since the FAC interferes in the beam propagation between the laser and the SAC, therefore the SAC position can only be approximated. The FAC is adjusted coarsely by maximizing the photo current until a value of several mA is reached, and fine-tuned by maximizing the output power of the amplifier. The vertical lens position at maximum photo current usually differs from the vertical lens position at maximum output power due to thermally induced distortion of the setup when the PA is driven with a total current of 2200 mA during fine alignment of the FAC and SAC focussing lenses.

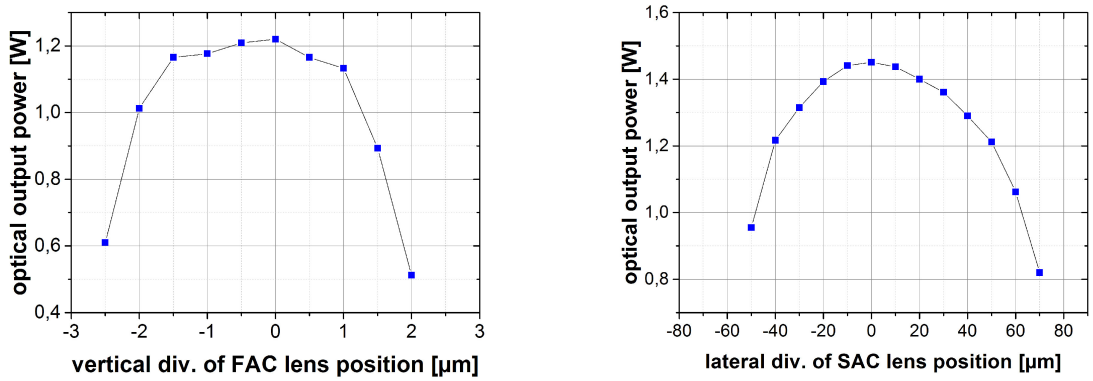

(a) FAC (b) SAC

Figure 4.15: Variation of amplifier output power by varying the position of the (a) FAC and (B) SAC coupling lens. The MO-beam is coupled best into the the amplifier at zero-position in this plot.

Before gluing the lens it must be ensured that the main power contribution is caused by the seeding beam, not by ASE activity. This is done by checking the spectrum of the beam at working point parameters. In the spectrum the ASE should be suppressed by at least 30 dB. The output power for various FAC lens positions, as shown in figure 4.15, are recorded to document the optimal position and determine possible misalignment. Figure 4.15 shows the development of the output power of the amplifier when the vertical (FAC) and lateral (SAC) lens positions deviates from the optimum. The output power in the FAC lens adjustment is lower due to the approximated but not jet optimized position of the SAC lens. The maximal output power auf 1.22 W in the FAC lens adjustment suggests that the SAC lens was miss-aligned by about 40 μm. After SAC lens alignment, an optical output power of 1.45 W could be achieved. Typically, at the point of maximal output power the ASE background is suppressed most strongly.

After the coupling lenses are integrated, the temporal collimation lenses can be replaced with the collimation lenses. The collimation FAC is integrated first, the same way as the collimation FAC of the MO. The two SAC lenses are placed on the bench according to the simulated position and fine tuned until the near field camera shows a minimum for the spot size. The far field camera should show a round spot within

the specified beam dimensions and with more than 50% power content in the central lobe. The higher the power content in the central lobe, the better the fibre coupling efficiency.

After finishing the integration of the SAC telescope lenses, the module is complete and can be fully characterized. The results of the characterization of the laser modules are described in chapter 6.

Chapter 5

Pre-Integration Component Characterization

A hybrid integrated laser module consists of actively driven components and passive components that together make up a complex laser system. When integrating multiple lasers systems, reproducibility of the performance is a measure for process control. With high demands on the performance, as they are defined in chapter 2, reproducibility becomes indispensable for fulfilling the requirements. Another measure for process control is the yield of production. The higher the yield, the shorter the time until the products can be provided and the production costs are smaller.

For both a high yield and reproducibility of the performance, the components, integrated in the system, have to provide a stable quality and reproducible performance themselves. However, this cannot be guaranteed by production. The integrated components are highly specialized and thus are produced in rather small numbers, not allowing for process optimization. In addition, variations in production scatter the performance of the components as well. Therefore each critical component has to be tested and qualified before integration into the system. Table 5.1 lists the critical components and their characteristics that had to be verified.

In the following chapter the qualification process, the test criteria and the results of these tests are described.

component	**form**	**qualification property**
DFB lasers	active	spectral behaviour, output power, facet condition
tapered amplifiers	active	spectral behaviour, output power, facet condition
micro-isolators	passive	optical behaviour, facet condition
micro-lenses	passive	facet condition
optical bench	passive	electrical resistance of interfaces
mechanical interface	passive	planarity of contact areas

Table 5.1: List of components that are qualified before integration, and their qualification property

5.1 Laser Diode Pre-Characterization

The most critical parts in a hybrid laser module are the semiconductor laser diodes themselves, namely the optical master oscillator diode and the optical power amplifier diode. Any defect can cause deviation from the specified performance of the diodes, which reflects directly on the performance of the laser module.

Figure 5.1 shows measurement values of malfunctioning laser diodes that could be identified before integration. The measurement methods are described in chapter 6. The DFB spectrum for varying injection currents in figure 5.1a shows strong multi-mode behaviour and modes jumps. This particular DFB laser cannot be used in a laser module dedicated to the missions described in chapter 2, because the requirement of single mode emission cannot be provided for injection currents < 200 mA. This, however, is the current limit of the current drivers in the MAIUS mission apparatus. In addition, the stability of the frequency emission for > 200 mA of this laser has to be questioned. The spectral instability can be caused by defects in the material or tensions in the bonds. Both can lead to a further degradation of the laser performance and to an early loss of the laser module. With that, the laser diode is not qualified for integration.

The optical output power of a seeded amplifier shown in 5.1b does not exceed 15 mW before decreasing for increasing injection currents. Also, the peak optical output power is reached at 1000 mA. Taking into account that the specified optical output power should be at least 2000 mW, and the thermal roll-over should not set in for an TA injection current < 2000 mA, this PA clearly cannot fulfil the specifications.

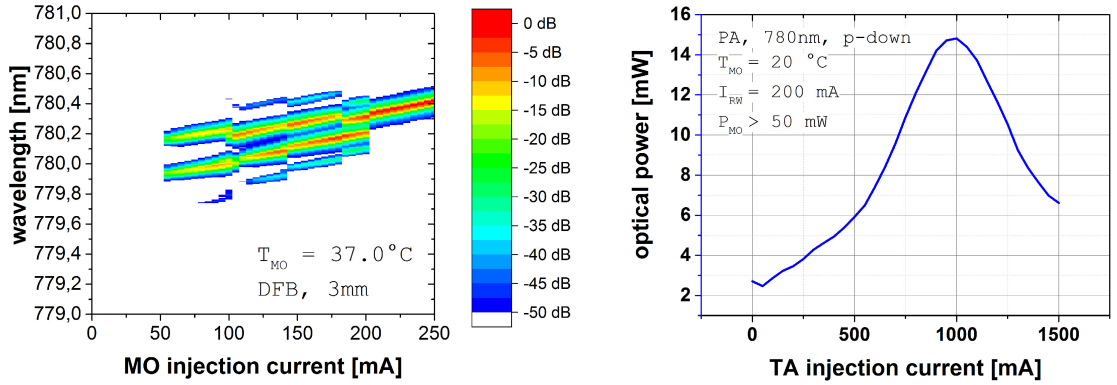

(a) (b)

Figure 5.1: Identified in component qualification: multi-mode spectrum of a DFB laser (a), and thermal roll-over of a PA(b)

There are a number of possible reasons for poor performance of laser diodes. Irregularities in processing of the doped layers under production, and coating of the facets, a disadvantageous splitting angle during wafer separation into diode bars, stress applied to the chip during assembly, or contamination of the facets with particles can cause disturbance in the propagation of a single optical wave or even can cause a COD.

There are a number of test methods available for identifying devices with defects or abnormal behaviour as early as possible in the production process. With the increased

demand on semiconductor chips for optical communication, automated methods were established to verify the performance of laser devices in mass production [107, 108]. However, for research and prototyping fully automated quality tests are too expensive and too specialized. Tests performed at the FBH during semiconductor processing are either manual or semi-automated.

Close inspection of the wafer can reveal areas that show irregularities which occurred during the etching, epitaxy, and galvanization, as well as particles or remaining coatings that nominally should have been removed. These defects lead to an increased risk of degradation of performance, reduction of lifetime, or even malfunction and potential restrictions during assembly, such as bondability of the device in further integration.

The inspection on wafer level is followed by tests on bar level. The wafers are separated by cleaving rows, so called laser bars, hosting laser diodes that are laterally still connected to each other. The facets of the laser bars are coated and a bar inspection is performed. In this measurement the single diodes are electrically contacted with needles, and the injection current is ramped per diode, revealing the current threshold, slope efficiency, optical output power, and the optical spectrum of the device. This test is not suitable for amplifier chips, because they do not provide a resonator. The optical output power of a PA in this test contains ASE only, amplifier chips will need a seeding beam for a performance test. However, the electrical test on bar level allows the detection of optical master oscillators with poor optical resonators, or malfunction of the facet coating but does not reflect on the actual performance of the chip on submount since the thermal conditions are not comparable and the recorded spectrum does not provide sufficient resolution to determine the side mode suppression ratio.

In order to verify the actual performance of a MO chip or an amplifier, the laser diodes have to be individually tested on submount level. To reach submount level, the chips are split of the bar, bonded onto a submount and wire-bonded to an electrical interface. During these steps, the chips are exposed to thermal and mechanical stress that can interfere with mode confinement in the chip. Therefore, and to identify diodes that do not perform according to specification (as shown in figure 5.1) pre-integration characterizations have to be executed.

However, identifying laser chips that do not perform within specification from the beginning of life might not be sufficient enough for pre-integration qualification. Especially the spectral behaviour of laser chips may change during the first hours of operation. Burning-in the chips before integration is therefore necessary to identify chips that change their behaviour depending on the time they have been operated. A negative example is given in Figure 5.2. It shows the optical spectrum of a chip after bonding to a submount and integration into a laser module. This chip was characterized (measurement on 23rd January 2012) and found to be a single mode chip before integration into the laser module. During integration a multi-mode behaviour appeared for injection currents $> 180\,\mathrm{mA}$. The spectrum of 21st February was recorded after approximately 50 hours of operation of the DFB. The spectrum recorded after another > 50 operating hours (12.03.12) verifies that the spectral performance degraded even further. Most likely the chip hosts defects in the wave-guide structure, propagating further into the active region with increasing operation time. These defects cannot be detected with a

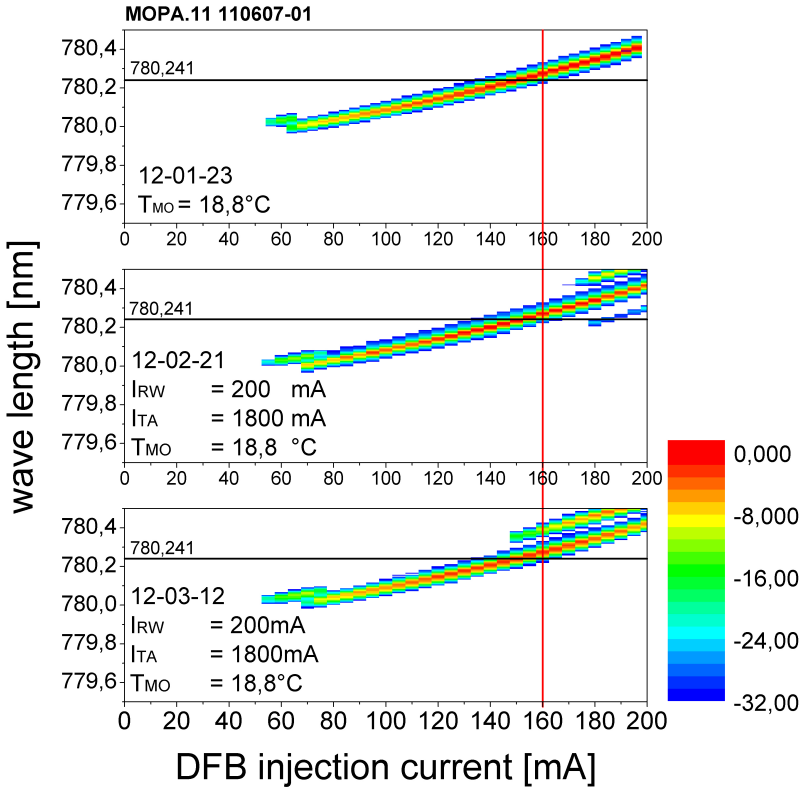

Figure 5.2: Degradation in the spectrum of a DFB diode over time

single measurement. However, most chips change their behaviour in the first operating hours and stay stable after "settling down" [109]. A burn-in phase of several hours before recording the initial characterization is therefore recommended [110]. This initial characterization is required to reveal changes in the chips optical behaviour after a longer burn-in of more than 100 operation hours. A chip without significant changes in the emission spectrum and optical output power can be considered as stable. The criteria of qualification are further defined in the following section 5.1.3.

Despite the electro-optical performance of the laser diodes, the facet conditions have to be qualified as well. The facet coating can already be inspected on bar level, but the inspection has to be repeated before chip integration because dirt can accumulate on the facet each time the device is handled.

To fulfil the strict requirements of the laser systems performance, as defined in table 2.2, a selection process on submount level was established, as described in the following sections.

5.1.1 Diode Selection Procedure

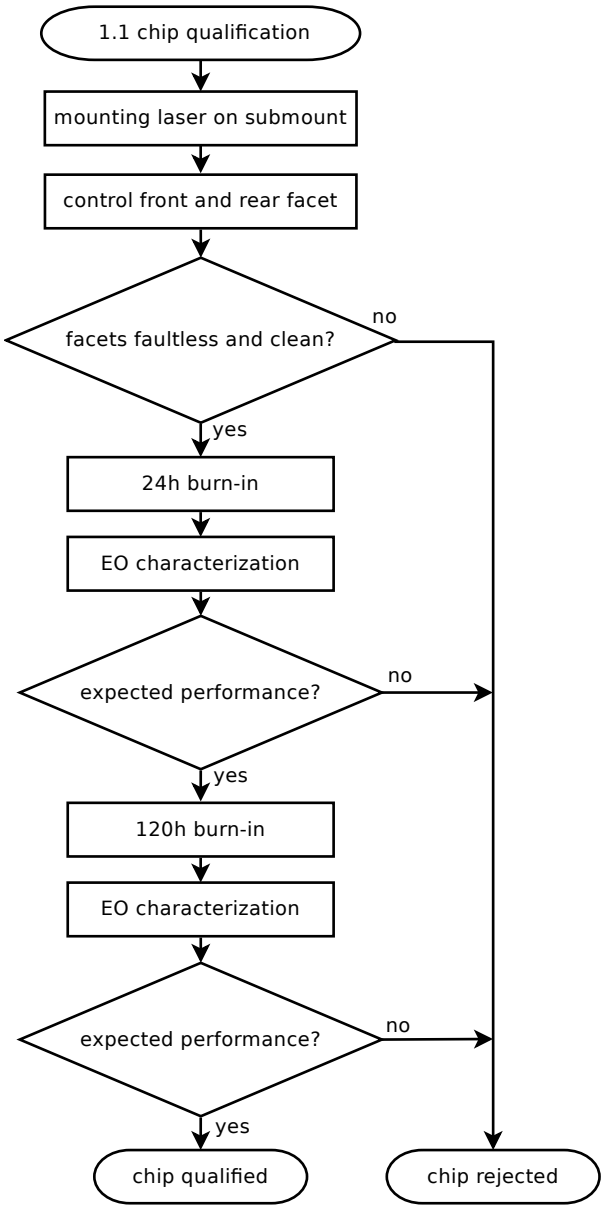

Figure 5.3: Overview of diode qualification process

Figure 5.3 illustrates the process flow of the chip qualification process. After submount assembly of the laser and amplifier chips, the condition of the facets are documented and evaluated. Devices passing the visual tests are placed into temporary mounts with electrical interface and undergo 24 h continuous operation [110]. After this initial burn-in, the optical power and spectral behaviour of the DFB-device under test (DUT) is characterized, both at 20 °C for statistical evaluation of all DUTs and at the expected working point temperature for individual verification. Chips passing the qualification criteria that are given in the following section, undergo a second, 120 h long continuous operation cycle. The electro-optical characterization after the long burn-in phase ensures that the performance of the chips has not changed significantly during five days of continuous operation. Diodes with a performance deviant from the initial measurement have to be rejected and will not be integrated into the laser modules.

For PA-DUTs the initial characterization is left out, the chips undergo a 120 h burn-in directly after the visual inspection. This is because the measuring process of PAs is more complex and yet not accurate enough to reveal degradation of the chips after 120 h operation. The burn-in process is nevertheless carried out to identify diodes with COD.

5.1.2 Pre-characterization and Burn-In Facility

The electro-optical qualification of the diodes is performed at a facility that was specially designed for that purpose during this thesis. In order to connect the diodes to a current driver and temperature controller, the chips on submount have to be temporarily placed into a mount with a specifically tailored electrical interface. This mount, depicted in figure 5.4a, is made of copper for good thermal conductance and is coated with a nickel layer against oxidation. On top, a bondable PCB is placed, hosting three MMCX interfaces, for interfacing various sections of a diode and for the temperature sensor on board the submount. The submount is fastened with a wedged wrangle placed in a notch in the mount. The diode is wire bonded to the PCB and can be placed both into a burn-in box, shown in figure 5.4b and into the pre-characterization setup, illustrated in figure 5.5.

For burn-in the diode mounts are placed into light-opaque boxes, so the burn-in process cannot be disrupted and does not disturb other work in the laboratory. Each box is capable of hosting four diode mounts and provides thermal stabilization. 4 mm-single-wire-connectors were chosen as electrical interface of the box, to obtain flexibility in controlling the single sections of each diode. In addition, 4 mm-singe-wire-cables are commonly available in most laboratories and are the common interface to consumer level voltage- and current sources. The burn-in box supports two sections per diode that can be operated separately. For thermal stabilization of the box either the internal temperature sensor or a sensor of one of the submounts inside the box can be used. Two Hameq HMP4040A are allocated as current sources during burn-in. An 1 MΩ resistor and a capacitor in parallel to the diodes avoid voltage peaks during switching of the current drivers.

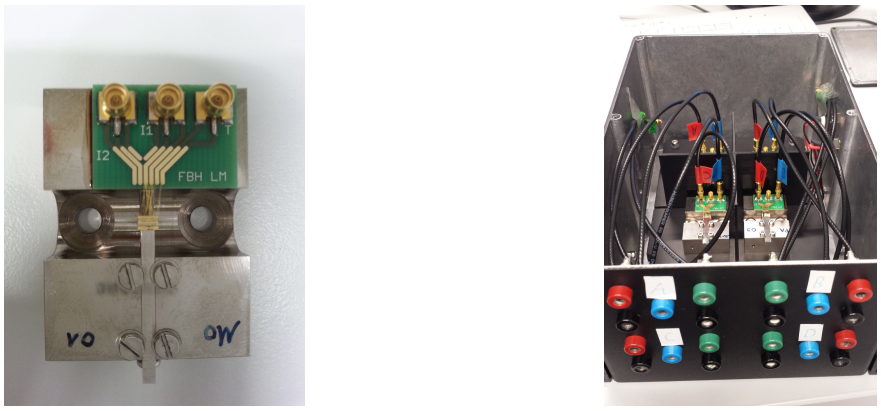

(a) (b)

Figure 5.4: Submount holder with electrical interface and a 3 mm DFB mounted (a), and an open burn-in box for four submount holders (b)

The pre-characterization setup, illustrated in figure 5.5, is designed to be compatible both for MO and PA operation. In MO operation, the main output of the DUT DFB ((ii) in fig. 5.5) is collimated with an aspheric lens with a focal length of 3 mm on a manual xyz-stage. A channel in the diode mount and the arm of the lens holder allow the lens

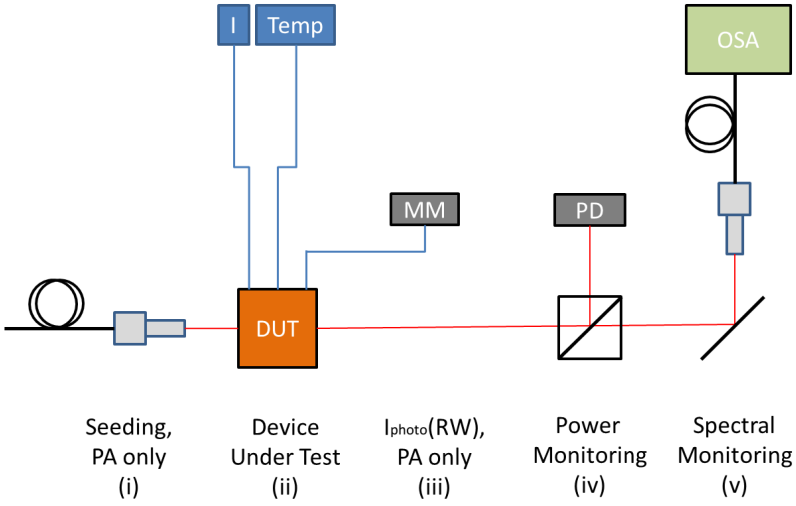

Figure 5.5: Schematic of pre-characterization setup in PA characterization configuration. (i) seed from PM fibre, (ii) DUT with current driver and temperature control, (iii) voltmeter for RW photo current measurement, (iv) power meter with Ulbricht sphere, and (v) fibre coupling for OSA.

to move freely and close in front of the diodes facet for beam collimation. The beam is guided through an optical isolator and to a 50/50 non-polarizing beam splitter. The beam splitter guides one half of the beam power to a photo detector in an Ulbricht sphere for power monitoring ((iv) in fig. 5.5), and the other half of the beam to a fibre coupling setup, which allows for spectral analysis simultaneously ((v) in fig. 5.5) with an OSA. The power measured by the Ulbricht detector is proportional to the true output power of the chip. The integrating sphere of the Ulbricht detector scatters the input beam uniformly on its inside surface, compensating for varying input angles and directions, and preventing saturation of the photo detector. This also allows for high optical input power such as a PA output beam.

For PA testing, a seeding beam and in-coupling optics are necessary, as shown as (i) in figure 5.5. The seeding beam is provided by one of the laboratories reference lasers via a polarization maintaining optical fibre with an output power of 20 mW. An optical isolator prevents the seed laser to receive optical feedback. Seeding an amplifier with a beam guided through a fibre ensures a Gaussian beam profile that is independent from the seed laser, and hence increases the reproducibility. Reproducibility of the seeding beam is important to be able to compare the results of several amplifiers, because the performance is strongly dependent on the seeding of the DUT. The seeding beam is guided with adjustable mirrors and a lens on a xyz-stage, comparable to the collimating lens at the output, into the RW facet of the DUT amplifier. The current through the tapered section of the amplifier is turned off in coarse seeding beam positioning to enable the monitoring of the RW photo current. The RW photo current allows for monitoring of the seed beam coupling into the amplifier and is suitable for coarse beam adjustment. It is measured with a multimeter, denoted as (iii) in figure 5.5. A RW photo current of > 6 mA is aimed at for the amplifiers used in this work. Fine tuning of the

seeding beam coupling is required when the TA current is switched on due to thermal deformation of the mounting setup and the diode during full power operation. The final position of the in-coupling lenses is determined in active alignment by maximizing the output power under working conditions.

The output beam of the DUT is collimated with the same lens used in MO operation, but in addition, a cylindrical lens with a focal length of 40 mm for SAC is required because of the differences in fast axis – slow axis divergence angles. The beam analysis setup in PA operation is identical to the analysis setup in MO operation, optical output power and spectrum can be recorded simultaneously.

5.1.3 Qualification Criteria for Laser Diodes

The MO and PA chip qualification procedure contains visual inspections and electro-optical characterization of the chips performance, including the monitoring of the optical output power at continuous operation and evaluation of the spectrum for various injection currents. The following qualification criteria for DFB and amplifier chips were established to reach the given performance within the given power budget of the experiments, as defined in table 2.2. According to their different functions, the criteria for DFBs and PAs have to be defined individually. The visual criteria are based on decades of experience with semiconductor chips at the FBH.

5.1.3.1 DFB Qualification Criteria

Visual Inspection:

- Surface: no scratches or other defects in the area 5 times the ridge width around the wave guide
- Facets: no particles and dirt, terraces, overlapping surface metal, coating releases, disruptions or other defects
  - within the area five times the ridge width in horizontal direction and three times the ridge width in vertical direction, typically 11 μm × 6.6 μm (*active area defect*)
  - exceeding the size of one fifth of the chip width, typically 80 μm (*bulk defect*)

  as depicted in figures C.3 and C.4.

Power versus Injection Current Characteristics:
Measurement conditions: at 20 °C chip temperature, current range 0 mA ... 200 mA.

- linear behaviour starting at threshold current, deviation from linear approximation <0.2 dB[1], jumps shall be related to mode hops
- minimum output power of 60 mW at 150 mA

Spectral Characteristics:
The targeted wavelength has to be reached at 150 mA for a working point temperature

[1] equals a deviation of 2 mW at 50 mW total output power

in the range between 15 °C and 40 °C.
Measurement conditions: at 20 °C chip temperature, current range 0 mA ... 200 mA.

- single mode behaviour, maximum two mode hops allowed
- no mode hops closer than ± 50 pm to the nominal operating wavelength at the WP setting
- the side mode suppression ratio (SMSR) to modes competing with the main mode has to be >30 dB (resolution bandwidth (RBW) 10 pm) for currents >25 mA behind the threshold current. (no multi-mode behaviour)
- intrinsic linewidth below 100 kHz, FWHM linewidth below 3 MHz (10 μs)

Characteristics after Burn-in Phase

- degradation in power less than 3%
- spectrum or features in the spectrum have shifted less than 15 pm compared to initial measurement

5.1.3.2 PA Qualification Criteria

Visual Inspection:

- Surface: no scratches or other defects in the area 5 times the ridge width around the wave guide
- Facets: no particles, dirt, terraces, overlapping surface metal, coating releases, disruptions or other defects
  - within the area five times the ridge width in horizontal direction and three times the ridge width in vertical direction, typically 11 μm × 7 μm, valid for RW facets at the rear side of the chip (*active area defect*)
  - within the area of wave guide width plus double of wave guide thickness in horizontal direction times double of wave guide thickness in vertical direction, typically 250 μm × 5 μm, valid for TA facets at the front of the chip (*active area defect*)
  - exceeding the size of one fifth of the chip width, typically 80 μm(*bulk defect*)

Power versus Injection Current Characteristics:
A critical value is the output power in seeded condition under realistic working point temperatures. For PAs that should amplify emission at 780 nm an output power of 1 W has to be reached while operating the diode at 35 °C ... 40 °C. 767 nm modules are expected to be operated at room temperature, these amplifiers therefore have less restricted temperature conditions.
Measurement conditions: at 20 °C (767 nm-PAs) and 30 °C (780 nm-PAs) mount temperature, seeding power of 20 mW, RW current 200 mA, TA current range of 0..2500 mA

- linear behaviour of output power for seeded operation, deviation from linear approximation <0.2 dB[2] no thermal roll-over for TA injection currents < 2200 mA [3]

[2] equals a deviation of 50 mW at 1000 mW total output power

[3] $P_{I=2200mA} > P_{I<2200mA}$

- minimal output power of 1000 mW for 2000 mA TA injection current, seeded operation

Spectral Characteristics
Measurement conditions: at 20 °C (767 nm-PAs) and 30 °C (780 nm-PAs) mount temperature, seeding power of 20 mW, RW current 200 mA, TA current range of 0 mA ... 2500 mA

- in seeded operation only spectral features of seeding oscillator observable, no additional peaks
- SMSR to ASE background larger than 40 dB (RBW 10 pm)

5.1.4 Results of DFB Diode Pre-Integration Characterization

In order to select the best suited DFB diodes for integration the qualification process is applied to all integration candidates. The qualification process contains a visual inspection of the surface and facets, and electro-optical (EO) characterizations. The EO characterization includes an optical output power analysis and an optical spectral analysis at various injection current settings. Optical power and spectrum are recorded simultaneously. The criteria for qualification are given in section 5.1.3. Measurements are performed at both 20 °C in order to have comparable measurement conditions in the following qualitatively analysis of the data, and at an expected working point temperature that can be up to 40 °C. Although the following analysis only refers to the 20 °C-data, diode lasers that do not meet the qualification criteria at the working point, e.g. they emit multi-mode, are rejected even if they meet the qualification criteria at 20 °C.

In total, 130 DFB diode lasers were inspected for integration into laser modules. The diode lasers were processed on four different wafers, some diodes were cleaved as 1.5 mm long diodes, the others were 3 mm long, as listed in table 5.2. One wafer was optimized for 767 nm emission, a wavelength not used in the MAIUS project but its predecessor QUANTUS II and presumably in subsequent experiments. The DUT-DFBs not only differ by their wafer but also by their coating process run, which, in this case, is individual per wafer. When referring to results of a certain wafer, this also includes the results of a certain coating run. A distinct statement to the performance of a coating run cannot be given independently of the wafer run.

Table 5.2 lists the number of DUTs and the number of incomplete data sets per wafer and chip length. Not all data sets could be completed. In 16 cases the facet data was missing but the EO characterization was complete. For these DUTs the facets were inspected and no critical defects were detected, however, the facet conditions were not documented, the diodes therefore are not counted in the facet evaluation. 7 DUTs only provided facet data. None of these 23 diode lasers passed the qualification, the data set therefore was not completed. For diodes which failed the facet inspection, the burn-in process typically was aborted to save time and resources since the diode already failed qualification. Diodes with facet defect were characterized only when the facet inspection was performed or re-evaluated after burn-in, or if the defect was caused by handling the chip during the qualification process, e.g. by touching a facet by accident.

Wafer	Wavelength	Chip Length	Total Number	Incomplete Data
C2610-6-2	767 nm	1.5 mm	26	2 (0; 2)
		3 mm	11	0 (0; 0)
C2213-6-2	780 nm	1.5 mm	6	3 (0; 3)
C2212-6-1	780 nm	1.5 mm	53	7 (1; 6)
		3 mm	24	3 (1; 2)
C1152-6-1	780 nm	1.5 mm	10	8 (5; 3)

Table 5.2: Overview of DFB integration candidates. Denotation in brackets: (incomplete facet data, incomplete electro-optical data)

In the following section the results of the visual inspection and the EO characterization after burn-in are presented.

5.1.4.1 Visual Inspection

The visual inspection included facet inspection and inspection of the galvanic surface of chips. Scratches close to the surface of the ridge wave-guide or galvanic surface damages were not observed on any of the DUTs. Therefore this criterion will be ignored further on.

Appendix C shows a selection of facet photographs, divided into qualified (section C.1) and not-qualified (section C.2) chips due to defects. As shown in section C.1.2, there are facets with defects that are not critical. These facets also count as qualified. According to section 5.1.3, facet defects can be classified as active-region-defects, as shown in figures C.3a-b and as bulk-defects, as shown in figures C.4a-b. An example of a facet defect arisen after a malfunction during handling the DUT is depicted in figure C.5.

In total 107 chips passed the visual inspection of both the front and rear facet. This corresponds to 82 % of all integration candidates, or 87 % of all chips with available facet data. The yield of the facet inspection is depicted in figure 5.6.

In 16 cases the facet was rated as ”failed”. The number of defects in the active region was, with 9 cases, almost twice as large as the number of bulk defects (5 cases). It is noticeable that all bulk defects were found on DUTs of the same wafer, the C2610-6-2 wafer, as shown in dark violet color in figure 5.7. The visual inspection of all 1.5 mm chips with bulk defects (4 in total) showed that the bulk material was broken on the edge as shown in figure C.4a, resulting in lose parts and large flaking of the coating. These defects might have been introduced during cleaving of the single chips from the bar. The 5th bulk defect was found on a 3 mm chip only after burn-in and characterization, depicted in figure C.5. It is assumed that during handling of this chip a macroscopic object, such as the collimating lens, touched the facet and destroyed it completely. The destroyed facet corresponds to the decreased output power (41 mW at 200 mA[4]) of this chip, disturbing the emission in the chip and hindering the photons to leave the gain material via the damaged facet.

[4]An expected output power value for 200 mA injection current would have been 90 mW.

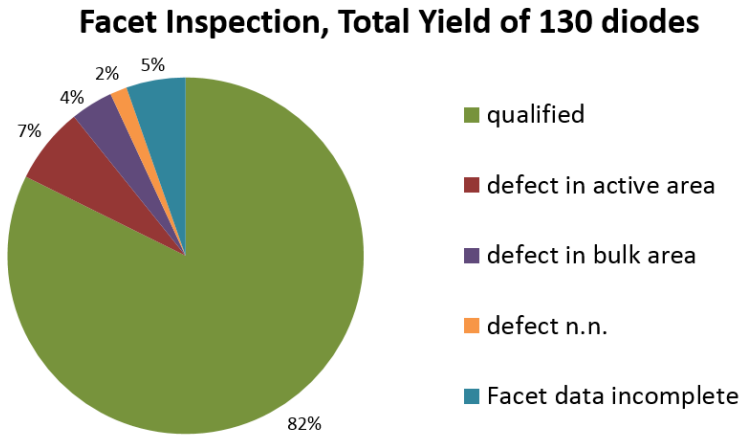

Figure 5.6: Total yield of facet inspection and failure causes

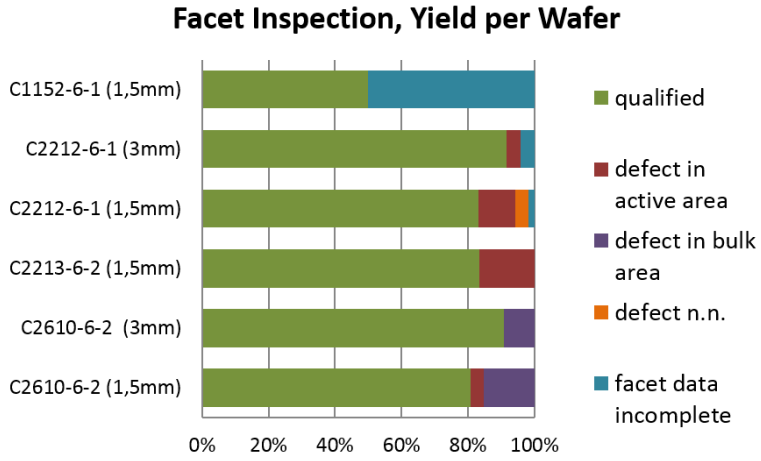

Figure 5.7: Yield of facet inspection for each wafer and length

The active-region-defects, on the other hand, are mostly distributed on wafer C2212-6-1, with 6 chips of 1.5 mm length and one chip with a length of 3 mm, mostly caused by particles close to the ridge area. The wafers C1152-6-1 and C2213-6-2 were only represented with 6 or less candidates in the facet inspection, not allowing for a statistical analysis.

5.1.4.2 Electro-Optical Pre-Integration Characterization

The EO characterization evaluates output power and spectrum before and after a 120 h burn-in phase. Pass and fail criteria, as well as measurement conditions are listed in section 5.1.3. 65 DUTs passed the EO evaluation, which corresponds to 50 % of all 130 available diodes, and to 57 % of all DFB diodes with available EO data.

49 diodes failed the EO characterization, this is 38 % of the total number of diodes and 43 % of all diodes tested. The distribution of rejection causes is depicted in fig-

ure 5.8. Figure 5.9 shows the yield distribution per wafer.

Some of the rejection causes are specific to certain wafers, such as for the wafers C2213-6-2 and C1152-6-1 with 100% and 43% failing rate, respectively, due to non-matching wavelength ranges. For both wafers, the emission wavelength at room temperature is too long compared to the wavelength aimed at in the experiment. To compensate the wavelength offset, the diodes have to be cooled down. If the aimed wavelength cannot be reached at 150 mA and 15 °C, the diode is rejected for the risk of damage due to water condensation.[5]

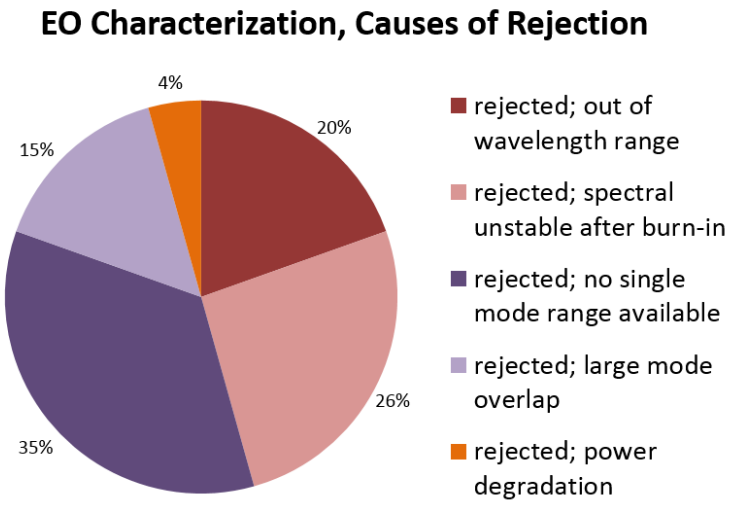

Figure 5.8: Causes of failure in EO characterization

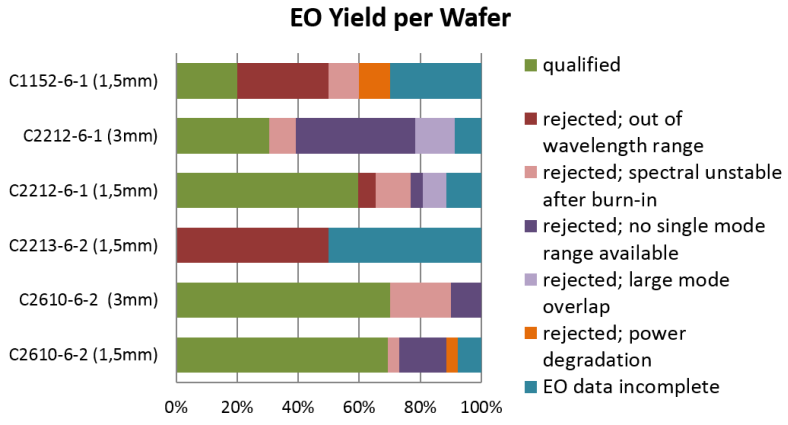

Figure 5.9: Yield of EO characterization for each wafer and length

However, the wavelength of the diodes of C2212-6-1 are slightly too short compared to the targeted emission wavelength. The blue-shift of the emission wavelength results

[5] At 25 °C room temperature and 50% humidity, water condensates on 14 °C cold surfaces. This condition has been present in the lab during autumn and spring. 1 K is a safety margin.

in the necessity to heat up the diode to reach the designated Rb D2 transition wavelength. 3 out of 49 of the 1.5 mm diodes have to be heated up to more than 40 °C in order to emit at the designated Rb wavelength. MIOB operation temperatures higher than 40 °C are an issue for the power amplifier, because the output power decreases with increasing operating temperature.

Spectral non-stabilities, such as multiple mode hops, multi-mode behaviour and frequency drifts after burn-in, are the main reason for rejection, with a total of 76% of all rejected diodes, as shown in in figure 5.8. 26% of all rejected diodes showed a significantly different emission spectrum after 120 h of burn-in operation, in a way that available mode hops have shifted to other injection currents, in some cases multi-mode behaviour appeared for certain injection current ranges. This effect can be observed for all remaining wafers. For 35% of all rejected diodes it was not possible to identify a working point that provided a tuning range of ± 50 pm in single-mode emission around the targeted wavelength. 15% of all rejected diodes showed current ranges of 50 mA and higher with SMSR smaller than 30 dB (RBW 10 pm), resulting in multi-mode behaviour for these current ranges. All of these diodes were processed on wafer C2212-6-1. Multi-mode behaviour is caused by weak mode selection in the resonator which may be caused by irregularities in the grating or on the facets. Two chips failed the qualification process due to power degradation, one from wafer C1152-6-1 and the other one from C2610-6-2.

5.1.4.3 Summary Pre-Integration DFB Characterization

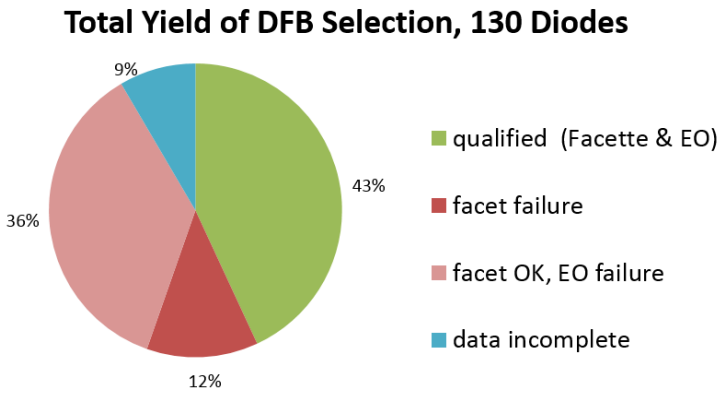

Figure 5.10: Total yield of pre-characterization of DFB diodes.

The overall yield of the qualification is depicted in figure 5.10. A chip failed the qualification if either the facet or the EO performance could not be qualified. In total, 43% of all 130 characterized chips passed both evaluation steps, the visual inspection and the burn-in with characterization of the EO performance. Ignoring the chips with incomplete data sets, the yield of DFB diode qualification is 47 %.

The rejection rate of 53% of the tested diodes underlines the necessity of the pre-characterization process before integration. Removing diodes from the MIOB comes

with the risk of damaging the MIOB due to scratches in the metal finish, and increases the production costs. Therefore integrating a non-qualified laser diode should be avoided.

20 laser modules were integrated during this thesis. Due to this selection process, only one case occurred where the DFB diode had to be replaced. The replaced diode was a 3 mm C2212-6-1 diode that became multi-mode after integration. Probably, the thermal stress applied during integration and wire-bonding damaged the diode or triggered the development of internal defects that were undetected until then. The diode was replaced with a 1.5 mm diode from the same wafer. The module operates faultless ever since.

5.1.5 Results of Power Amplifier Pre-Integration Characterization

Goal of the qualification process of the PAs is the identification of diodes with decreased life time expectancy, or diodes that are not capable to deliver the required output power in the given temperature range. The visual inspection and burn-in process is carried out to find defects that decrease the life time, the EO characterization reveals whether the performance of the DUT fulfils the requirements. The qualification criteria can be found in section 5.1.3.2.

In total, 100 power amplifiers were characterized, summarized in table 5.3. The 71 amplifiers for 780 nm are all provided by the same wafer, C2358-3. They are 4 mm long with a 2 mm RW mode filter section and a 2 mm long tapered section with an opening angle of 6 °. In addition 29 diodes for 767 nm amplification were characterized. They were processed on two different wafers, C1030-3 and C2850-3. Diodes extracted from wafer C1030-3 provide only 1 mm of RW mode filtering section and 3 mm of tapered amplifying section. The remaining diodes have the same design as the diodes for 780 nm. The diodes were either mounted with p-side facing the submount for better thermal conduction to the laser module, called "p-down" mounting and depicted on the right of figure 5.11, or with the p-side pointing away from the submount, called "p-up" mounting, see left picture in figure 5.11. P-up mounted diodes host an additional heat spreader on top, made of copper-tungsten (CuW) for a better matching of thermal expansion with the GaAs diode substrate.

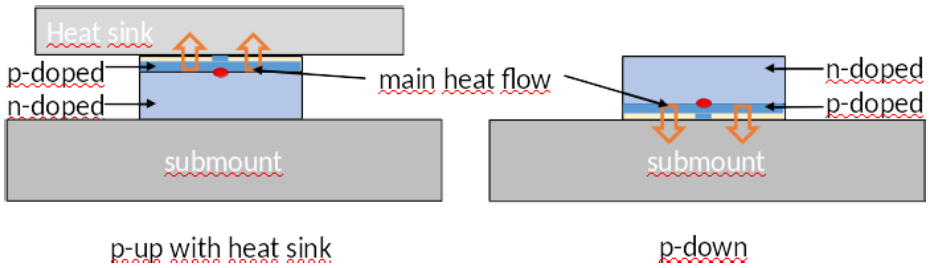

Figure 5.11: Mounting of the PAs: either p-up with heat spreader (left) or p-down with the submount as heat sink (right)

As denoted in table 5.3, the rate of incomplete data for certain amplifier types is with 30 of 58 diodes (780 nm, p-down) and 7 of 10 (767 nm, 2 mm long RW, p-down)

Wafer	Wavelength	RW Length	Mounting	Total	Incomplete Data
C1030-3	767 nm	1 mm	p-up	12	1 (0; 1)
			p-down	3	1 (0; 1)
C2358-3	780 nm	2 mm	p-up	13	4 (3; 1)
			p-down	58	30 (2; 28)
C2850-3	767 nm	2 mm	p-up	4	1 (0; 1)
			p-down	10	7 (0; 7)

Table 5.3: Overview of PA DUTs. All testes chips are 4 mm long. Denotation in brackets: (incomplete facet data, incomplete electro-optical data)

very high. In most cases the data of EO characterization is missing. This is due to the fact that diodes that failed the visual inspection were not characterised electro-optically to save resources. In addition, the electro-optical characterization was stopped after enough amplifiers for integration were qualified.

5.1.5.1 Facet Inspection

The visual inspection includes the inspection of the surface of the diodes as well as the evaluation of the front and rear facet. As for the DFBs, no defects on the surface of the DUTs could be observed, further discussions therefore are focused on the facet inspection. Examples of qualified PA facets (figure C.1c-d) and facet defects (figures C.3c and C.4c) are given in the appendix C. Again, the facet defects are divided into bulk area defects and active are defects.

65 % of all PA-DUTs passed the facet qualification, as shown in figure 5.12. This is less than the qualification rate of the DFB diodes (82 %). One reason for the decreased qualification rates for amplifiers is the special mounting. PAs are mounted either p-side-up with a heat spreader on top of the p-side or p-side-down on the submount, as shown in figure 5.11. Both mounting concepts include a soldering process on the p-side close to the active area, combined with a higher risk of damage of the facet due to overflowing solder, stress close to the active region of the facet and increased handling of the chips. In addition, the active area of the output facet of the tapered power amplifier (TPA) is enlarged due to the tapered waveguide, increasing the risk of active area defects.

However, p-up mounted chips passed the facet inspection with a rate of 85 % of all diodes with available facet data (76 % of all p-up mounted diodes), as shown in figure 5.13. This rate is slightly lower than the visual qualification rare of the DFBs (82 %, all diodes) and indicates that the p-down mounting increases the risk of damaging the facet.

This tendency can also be observed in the facet failure rates. 15 % of the p-up diodes failed the facet inspection, compared to 12 % failed DFBs, but 38 % of the p-down mounted amplifiers failed, resulting in a total failure rate of 30 % for amplifier chips.

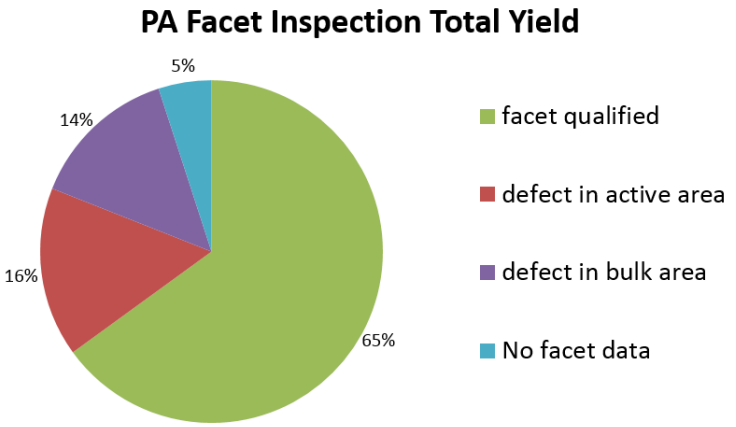

Figure 5.12: Total yield of facet inspection of PA diodes.

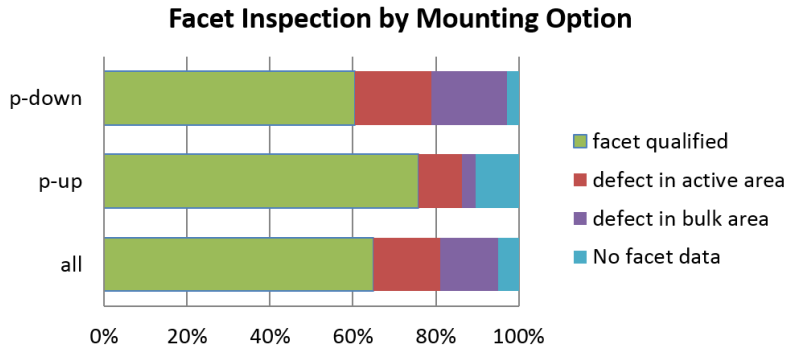

Figure 5.13: Distribution of facet defects due to mounting configuration.

Active area defects and large area defects are equally distributed. Active area disturbances were mostly caused by particles or solder splashes at the output facet, as depicted in figure C.3c. These failures disturb the beam profile and may decrease the lifetime of the diode due to local heat development on the particles. Main reason for large area defects is the formation of terraces on the coating on wafer C2358-3. In small numbers other problems with the coating, namely an inhomogeneous colouring of the coating of a facet and shadowing of facets during coating occurred, as well as defects due to handling and processing of the coated chips, such as damages caused by contact with the facet, lose bulk material that are broken out under cleaving, and solder and dirt. All these defects can decrease the life time of the chip or the integrated module.

5.1.5.2 Electro-optical Pre-Integration Characterization

61 out of 100 amplifiers were characterised electro-optically. 77 % of the characterized diodes (47 % of all available PA diodes) passed the EO qualification. The remaining 23 % of the characterized amplifiers could not provide the requested optical output

power at the designated working point temperature. For these diodes thermal roll-over appears for TA injection currents $< 2000\,\text{mA}$, as shown in figure 5.1b.

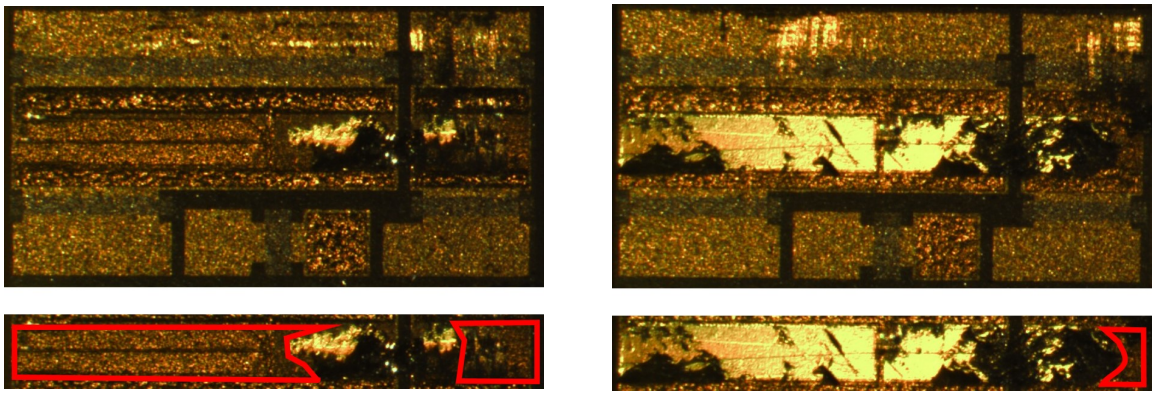

(a) (b)

Figure 5.14: PA submounts after shearing of the diode. Areas where the solder did not wet the diode surface are marked in red. On the left: Bonding without Ar-cleaning process, wettability: 40 %. On the right: submount was cleaned with Ar before bonding, wettability: 95 %.

As reason for low optical output power and thermal roll-over for relatively small injection currents bad thermal coupling between amplifier chip and submount could be identified. When shearing a not qualified PA laterally from the submount, wettabilities of the solder down to 40 % of the diodes surface were detected. For good thermal contact a wettability of $> 90\,\%$ of the surface is required. An example of poor wettability is shown in figure 5.14a. The figure shows a submount and the remains of the diode after shearing off the diode. Areas where the solder wetted the submount surface remained on the submount and can be detected either as shiny golden areas (golden galvanic finish of the diodes) or black areas (bulk material of the diode). In figure 5.14a the areas with no remains of the diode are marked red. In order to increase the wettability of the solder, the bonding temperature was increased by $10\,^{\circ}\text{C}$ and the surface of the submount was cleaned in an ultrasonic bath with argon directly before bonding of the diode. The argon treatment removes organic material and oxidations that constrains the wetting of the solder on the diodes surface. The increased temperature increases the responsiveness of the materials. The shearing result of a submout with increased bonding temperature and argon treatment is shown in figure 5.14b. The wettability of the solder could be increased to approximately 94 %. Diodes that were bonded to submounts after argon treatment showed an improved thermal conductivity between chip and submount and fulfilled the requirement of optical output power.

For characterizing the amplifier, the mount temperature of the structure holding the submount was stabilized to the temperature named in the measurement conditions. For some amplifiers, the actual submount temperature was recorded during characterization as well, allowing conclusions of the thermal behaviour of the amplifier independent of the thermal conductivity of the measurement setup. In figure 5.15 the optical output power at $I_{TA} = 2000\,\text{mA}$ is plotted against the temperature of the submount

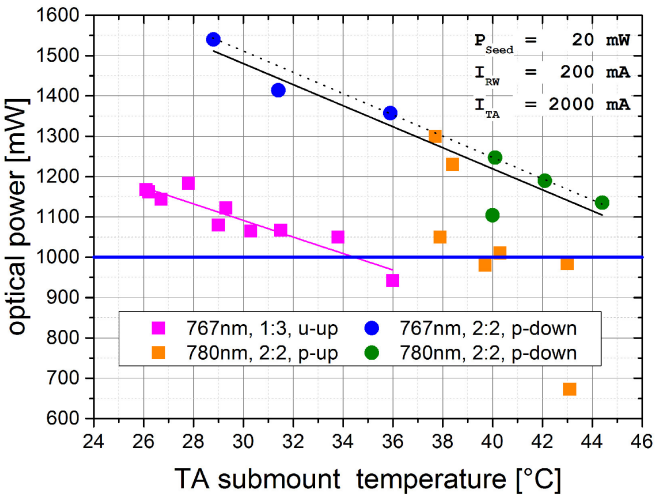

Figure 5.15: Output power dependent on submount temperature for various PA chips

of the PAs. The blue line marks the output power qualification criterion of 1 W. The evaluation includes diodes with both RW-section lengths, 1 mm and 2 mm, and both mounting options, p-up and p-down. According to figure 5.15 p-down mounted amplifiers with 2 mm RW section (illustrated as blue and green dots) reach higher output power values for comparable submount temperatures than p-up mounted amplifiers. The p-down mounted diodes show a linear decrease of output power for increasing submount temperatures with - 26 mW/K (black line), independent of the wavelength they amplify. At 40 °C 1250 mW can be achieved, with a deviation of 4.3 mW/K. The black dotted line shows the linear fit of p-down diodes with an offset of + 30 mW. The dotted line captures all but two measurement points of the p-down values that show up underneath the linear fit. Probably the wettability of the solder to the submount of these two diodes is not as high as for the other p-down diodes in this sample. As described above decreased wettability results in decreased thermal coupling and thus increased thermal resistance and decrease in optical output power.

The p-up mounted diodes of the 780 nm 2 mm long RW-section chips are illustrated with orange squares. All of them, with one exception, are below the power-temperature line estimated for the p-down mounting, indicating that p-down mounted amplifiers are able to emit more power than p-up-mounted diodes for the same temperatures. This can be explained by the limited thermal capacity of the heat spreader on top of the diodes. However, the distribution of the p-up mounted diodes is scattered, a meaningful prediction of the power-temperature behaviour could not be found based on this data.

The data points of the p-up mounted 767 nm amplifiers with 1 mm RW-section (in pink), however, decrease with 20.5 mW/K (± 2.8 mW/K) and show an offset of approximately - 400 mW compared to the p-down mounted PAs. The offset can both be explained by the mounting and by the increased length of the TA-section. A longer active area results in decreased carrier density for identical injection currents, resulting in decreased current-to-optical power conversion efficiency. The p-up mounting, again

increases the thermal resistance of the device, resulting in lower output power.

All characterized diodes that emitted more than 500 mW optical output power fulfilled the spectral qualification criteria of ASE suppression and distribution of the seeding beam spectrum. For the other diodes, having problems with the thermal conduction, the spectral behaviour was not evaluated because the output power criteria could not be fulfilled.

5.1.5.3 Summary Pre-Integration PA Characterization

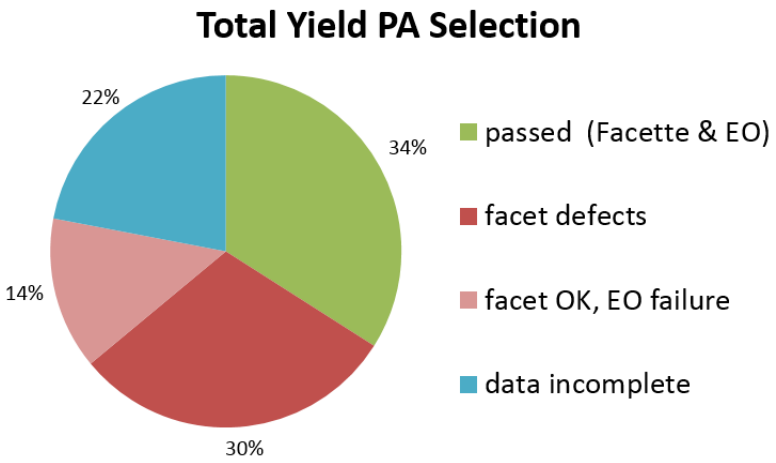

Figure 5.16: Total yield of the PA selection process

34 % of the 100 available amplifier diodes passed the qualification procedure. The main reason for rejection was defects detected during facet inspection with an error rate of 30 % (compared to 12 % for DFBs). This can be explained with the different mounting concept for PAs in order to increase the thermal conduction in the diode at the cost of higher defect rates of the facet. The rejection rate of the PAs after EO characterization, on the other hand, is only 14 % of all diodes, and with that small compared to 36 % for the DFB diodes. This is due to the fact that PAs are not expected to change spectral behaviour and therefore the qualification criteria for EO qualification of the PAs are less tight than for MO diodes.

The 22 % of chips with incomplete data are chips that passed the facet inspection but were not characterized electro-optically because the required number of amplifiers for integration into laser modes was reached. Due to this, the total yield of the PA qualification cannot be directly compared to the DFB diode qualification yield. If the distribution of qualification of the 22 not-characterized diode equals the qualification rate of the other 48 diodes that run through the EO characterization, than a total yield of 50 % for PAs could have been reached. If so, the yield of both the DFB and the PA qualification process would in the range of 50 %.

The PA qualification process revealed problems in the diode assembly that led to an adaptation of the assembly process. After the adaptation of the assembly process the yield of qualification improved. With that the qualification process could satisfy a controlling function of the production processes.

5.2 Passive Component Pre-Integration Characterization

Additionally to the semiconductor chips, the optical micro-isolators, lenses, the MIOBs themselves and the CCP are qualified before integration.

Micro-Isolators The qualification of the isolators includes an examination of the facets for dirt or defects, as well as an optical characterization of the isolation, the polarization extinction ratio (PER), the insertion loss and the rotation angle of the output beam compared to the input beam. The purpose of the optical characterization is to confirm the optical performance as it is defined in the data sheet. The characterization became necessary after it was discovered that some isolators came with a wrong waveplate, resulting in a poor PER and a rotated output polarization. Single stage and semi-double stage isolators have been tested, both for 767 nm and 780 nm. A semi-double optical isolator provides a better isolation on the cost of a higher insertion loss, compared to a single stage optical isolator.

For the isolator characterization, a specific measurement setup was designed with defined linear polarized light passing the DUT isolator. The DUT is placed on a V-grove between a polariser and analyser device, formed by two polarizing beam splitters mounted on motorized rotational stages. The optical power of the beam, passing the setup, is detected with a photodiode. Depending on the alignment of the polariser and analyser, and the orientation of the DUT, the isolation, PER, and rotation angle are determined.

An isolator passes the visual test, when the facets are free of dirt or scratches. To pass the optical characterization, single stage isolators have to provide isolation larger than 27 dB with an insertion loss less than 5 dB. The isolation of a semi-double isolator has to be larger than 50 dB with the insertion loss not exceeding 8 dB. The PER has to be larger than 27 dB, and the rotation angle of the output beam shout not exceed 10 °. The qualification criteria are based on the data sheets and the experience obtained with the micro-isolators.

In total, 198 micro-isolators were characterized. Visual checks show that 31 % of the DUTs facets were affected by dirt. In some cases, however, the dirt could be removed without touching the facets by turning the isolator upside-down or by blowing it off with a stream of pure nitrogen. The optical characterization is summarized in table 5.4.

The average isolation of a single stage isolator and semi-double isolator was measured to be 38.7 ± 6.5 dB, and 57.1 ± 5.5 dB, respectively. With that, the isolation of the single stage isolators were better than expected (30 dB). As expected semi-double stage isolators show a significantly higher isolation than single stage isolators, the measurement of the isolation of the semi-double isolators where limited by scattered photons in the measurement setup. The isolation performance of 767 nm isolators does not differ significantly from 780 nm. However, one batch of single stage isolators for 767 nm had to be rejected due to significantly less isolation (23.9 dB compared to 41.9 ± 2.6 dB for qualified batches of 767 nm single stage isolators). The cause of this failure could not

isolator type	isolation [dB]	ins. loss [dB]	PER [dB]	pol. rotation [°]
SiSt 780 nm	39.7 ± 5.2	3.5 ± 0.4	32.7 ± 4.5	3.1 ± 4.0
SDSt 780 nm	56.8 ± 4.7	6.3 ± 0.3	34.1 ± 6.7	3.1 ± 4.4
SiSt 767 nm	38.1 ± 7.7	4.0 ± 0.5	33.0 ± 8.8	4.1 ± 3.4
SDSt 767 nm	54.9 ± 3.2	7.7 ± 0.6	32.6 ± 4.5	3.5 ± 2.6

Table 5.4: List average performance of micro-isolators, classified into wavelength: 767 nm and 780 nm, as well as in design: Single stage (SiSt) and Semi-double stage (SDSt)

be determined. Still, identifying this batch as faulty proves the necessity of the optical qualification of the isolators.

In terms of insertion loss, the 767 nm isolators show higher absorptions of the incoming beam than the 780 nm isolators. This can be explained with the material properties of the thin film plates inside the isolators. They were once optimized for higher wavelength (> 1000 nm), resulting in the effect of increasing absorption for decreasing wavelength of the input beam. In contrast, isolators tested with 1070 nm input beam showed an insertion loss of 2.4 ± 0.2 dB.

The average PER value of the tested isolators, independent of wavelength and design, is consistently larger than 32 dB, as shown in table 5.4. However, there were in total only 7 isolators with a PER less than 27 dB. 5 of those were characterized with a different wavelength than specified. When using a wavelength other than the specified wavelength of the device, e.g. 767 nm for 780 nm isolators, the PER drops to approximately 17 dB. This behaviour is expected due to the wavelength dependent characteristics of the optical materials of the isolator.

In average, the absolute value of the rotation angle of the polarization was $3.1 \pm 3.8\,^{\circ}$. 767 nm isolators have a slightly higher excursion of the rotation angle, compared to 780 nm isolators. 7 % of all isolators rotated the polarization more than $5.5\,^{\circ}$. The uncertainty of this measurement was $< 1\,^{\circ}$. Again, the cause of the different beam rotation angles might be due to varying alignments during production.

In summary it can be stated that the performance of 767 nm isolators is constricted, compared to the 780 nm isolators. This can be explained with the wavelength depended performance of the materials used in the isolator design. However, the isolator's isolation is not affected and they are generally suitable for integration into micro-integrated laser modules emitting at 767 nm. The results of the single isolators allowed to identify a faulty batch that was returned to the manufacturer. 54 % of the revised micro-isolators passed the qualification. The majority of isolators that did not apply to the qualification criteria in the optical test were either in the faulty batch or were characterized with a wavelength other than the specified wavelength. The visual check allowed the improvement of the facets of the isolator before integration. Still, 30 % of the isolators failed the visual qualification of the facet.

Micro-Lenses The lenses are only examined visually for dirt, scratches or flaking at the edges. None of the lenses failed this test before first integration, but some lenses had to be replaced after their facets were contaminated with adhesive during the integration process.

Micro-optical Bench The MIOB itself has to be checked electrically and visually before integrating the submounts. The benches are cleaned either with pure nitrogen or with vacuum tweezers to avoid damage on the bonding or gluing areas. The electrical interfaces are tested for their input resistance and the connection to the bond pads. All 30 MIOBs were tested. One MIOB was rejected for not providing electrical contact of the pre-amplifier section. This MIOB was replaced by the manufacturer. All other benches passed the test.

Mechanical Interface The planarity of the top and bottom surface of the mechanical adapter CCP is fundamental to avoid mechanical stress and misalignment of the optical components. The fail criterion was therefore defined as a maximal bow of 10 μm over the entire length of the CCP. All CCPs are characterized with a non-contact, optical profilometer Zygo NewView 6300. After adjusting the manufacturing process the CCPs showed an average bow of 3 μm of the bottom site and 1.4 μm bow on the side carrying the MIOB. All CCPs could be qualified for usage with MOPA modules.

5.3 Conclusion of Pre-Integration Qualification

This chapter shows that a pre-integration qualification process is highly recommended to increase the yield of module production and decrease costs and working hours. Without the qualification, the bonding problems for the PAs would have been undetected until after the first chips had been integrated onto the MIOB. In that case the MIOBs hosting a PA with poor thermal contact would have turned into rejections, negating the work of MO collimation and increasing the demand on the customized MIOBs. With a yield of around 50 % each for DFBs and PAs, the number of modules that would have to be built in order to fulfil the delivery demands, would have quadrupled, since some of the defects would have affected the performance of the module only after some time of operation. Possibly, some modules could have degraded over time or failed spontaneously in the customers experiment, increasing the assembly time or stopping the experiment.

However, the measurement setup, described in section 5.1, revealed problems with the handling of the heat dissipated by the amplifiers into the submounts. Hence, the temporary mount should be redesigned in order to guarantee a larger contact surface with the submount. The mechanism, holding the submount in place, has to be strong enough to withstand the resilience of the bond wires but may not touch or puncture the gold (Au) wire bond surfaces. With a submount size of 2 mm width and 150 μm distance of bond Au to the edge, this is a challenge. Adjustment pins can be used to guarantee a reproducible positioning of the mount in the setup for each measurement. A positioning robot can help to reproduce the position of the in-coupling lens of the

seed laser, an automatized robot may optimize the seeding for each measuring point, based on the output power of the amplifier.

Although the chip setup has potential for optimization, as shown above, it served its purpose for the MAIUS mission.

Also the qualification of the passive components revealed variations in the performance due to production uncertainties and failures, as seen for the micro-isolators. The qualification of all components is therefore recommended.

Chapter 6

Characterization and Qualification

In the course of this thesis, 20 modules were assembled, designed and integrated as described in chapter 3 and 4. Out of these, 18 modules, of which 5 modules host a master oscillator only, have been delivered to project partners to be used in various experiments such as the missions described in chapter 2. This chapter deals with the individual performance and behaviour of these laser modules. The electro-optical characteristics describe CW behaviour at working point operation parameters, as optical output power, spectrum, linewidth, and modulation capabilities. The environmental characterization compares the performance of the laser modules after an intense mechanical and thermal stress test, relevant for the operation of the laser modules in the field and in space.

6.1 Electro-optical Characterization

The electro-optical characterization results describe the behaviour of the laser modules for certain operation temperatures and injection currents. With that the suitability of the laser modules according to the experiment's requirements can be verified and the performance of the laser modules can be predicted.

6.1.1 Optical Output Power

The output power of a MOPA is dependent on the injection current applied to the amplifier section, the temperature of the device and the seeding power of the master oscillator. Figure 6.1 plots the output power against the injection current into the amplifier section for various operating temperatures. The MO input power corresponds to 25 mW behind the isolator. For all temperatures, the optical output power increases exponentially for an input current < 750 mA, then develops linearly with 0.95 W/A (35°C) up to 1.16 W/A (15°C). For currents > 2500 mA an increasing thermal resistance (see equation 3.15) results in a minimized increase of the optical output power. However, no thermal roll-over could be observed for amplifier injection currents < 3500 mA. Even for 30 °C an optical output power of > 3 W can be achieved.

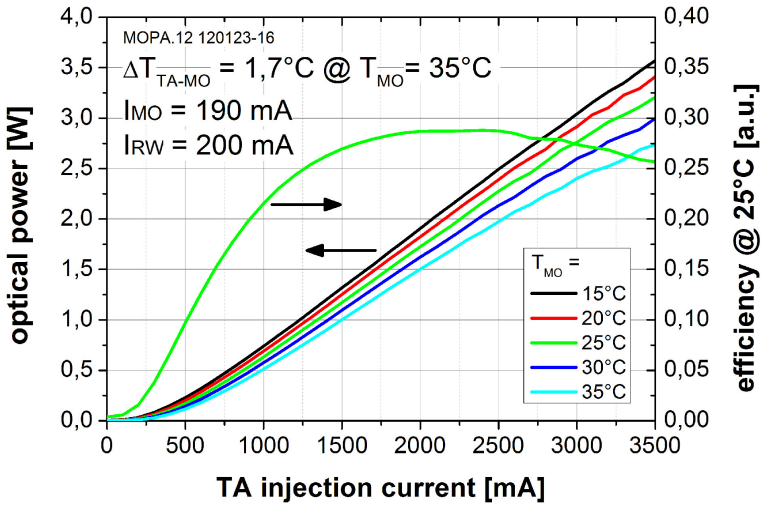

Figure 6.1: Relation of output power and MIOB temperature against amplifier input current (left axis), and conversion efficiency for 25 °C (right axis)

The thermal dependency of the output power can also be derived from figure 6.1. At 2000 mA the power decreases linearly with 20 mW/K.

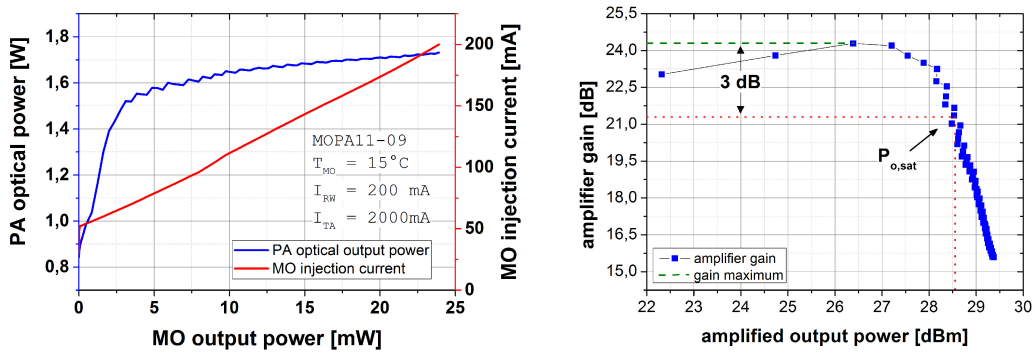

(a) (b)

Figure 6.2: Optical output power of MOPA module (a) and amplifier gain (b) against MO optical output power.

The green graph belonging to the right axis in figure 6.1 shows the conversion efficiency of the MOPA system at 25°C for various TA injection currents. The maximal efficiency is reached at 2000 mA with 29% and decreases when thermal resistance in the amplifier increases, affecting the power performance. The power consumption of the MO and RW section is included in this calculation. The power consumption of a MOPA can be estimated by the injection current and voltage over the semiconductor section, including the electrical interface. The MO voltage typically is in the range of 2.3 V, the RW voltage typically is around 2.0 V and the TA voltage is around 2.4 V. With

a maximum of 200 mA for the MO and RW section and 2000 mA at the TA section, the power consumption of a MOPA typically will be around 5.7 W.

The dependency of the output power and the seeding power is shown in figure 6.2a. The blue curve depicts the output power of the MOPA system versus the output power of the DFB behind the optical isolator, corresponding to the seed power of the amplifier, the red curve is the injection current of MO diode. The power emitted for $I_{MO} \leq 55$ mA is the ASE output of the amplifier. 55 mA is the threshold current of the DFB in this module. The maximal gain of the MOPA is 24.1 dB. The gain saturation is reached for an input power of 5.2 mW with a saturation power of 1577 mW. In figure 6.2b, depicting the gain of the amplifier, the ASE background of 850 mW was subtracted in order to show the gain caused by the input power of the master laser. However, this is just an approximation, because the ASE background also decreases with increasing seed power.

The required optical free-space output power, as defined in table 2.2, can be achieved also for WP temperatures $> 35\,^{\circ}$C and for PA injection currents < 2000 mA within the defined power consumption boundaries.

6.1.2 Optical Spectrum

The optical spectrum of a MOPA is dependent on the MO current and the MO temperature. Since the laser modules are designed to operate at a certain wavelength, the working point, the combination of I_{MO} and T_{MO} which allows for operation at the aimed wavelength, has to be defined.

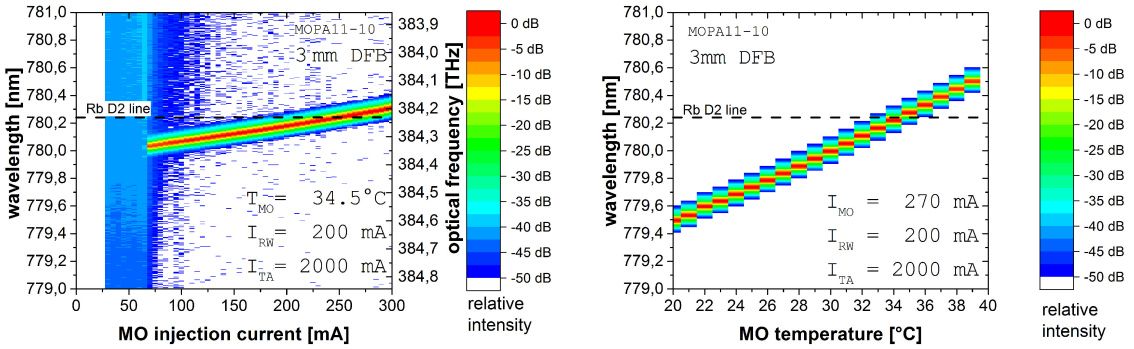

(a) (b)

Figure 6.3: Wavelength of a MOPA, hosting a 3 mm long master laser versus (a) MO current and (b) MO temperature. The spectra are normalized to the global peak of all emission spectra in the figure.

Figure 6.3a shows a false colour plot of the emission spectrum versus the MO injection current of a 3 mm long DFB diode. It was recorded with an Advantest Q8384 OSA with a resolution bandwidth (RBW) of 10 pm (FWHM) and calibrated with a High Finesse WS-7 wavelength meter. The spectra in the figures are normalized to the global

peak of all emission spectra. Red colour indicates high power spectral intensity, values below –50 dB are shown in white. There were no values taken in the range of zero to 30 mA since the threshold current of the MO in this laser module is >30 mA. This protects the fully pumped amplifier (with I_{RW}=200 mA and I_{TA}=2000 mA) from overheating, since the carriers in the PA cannot be cleared without an optical input. The dashed line indicates the desired emission wavelength, in this case 780.241 nm as defined by the Rb D2 line. This emission wavelength can be provided by the laser module. The laser module shows stable single mode behaviour, no mode hop can be observed. The wavelength shifts with an average of 1.2 nm/A. However, a DFB laser with a 1.5 mm long resonator shows a current tuning of 2.7 nm/A due to the higher carrier density in the shorter active region.

Figure 6.3b shows the dependency of the wavelength on the temperature of the optical master oscillator on the same laser module. MO and PA currents are kept stable at the designated values. A linear tuning of 0.053 nm/K can be observed for this 3 mm DFB laser. A 1.5 mm DFB laser provides with 0.056 nm/K a temperature tuning coefficient that is in the same range as the temperature tuning coefficient of a 3 mm diode. With that, the length of the diode has only a minor influence on the temperature tuning.

Since the operating temperatures of the MOPA are limited by the dew-point of the environment (typically 15 ° C) and by the thermal roll-over of the output power, a typical temperature range of 15°C – 40°C allows for approximately 1.4 nm thermal wavelength tuning. The current tuning range is limited in order to decelerate the ageing process of the laser chip, and contributes to a longer life time of the laser. Hence, the MO current tuning range in the MOPA module typically spans 150 mA for a 1.5 mm DFB, which corresponds to 0.4 nm current tuning range, and 300 mA for a 3 mm DFB, which corresponds to 0.36 nm current tuning range. With that, the total spectral tuning range of a DFB laser module is approximately 1.8 nm or 880 GHz for 1.5 mm short laser chips and approximately 1.7 nm or 740 GHz for 3 mm long chips. These values do not differ much, since the smaller current tuning coefficient of 3 mm DFBs is compensated with a larger current range that can be applied to the chip due to the longer active area in order to reach the same energy density in the active area. The requirement of a tuning range > 100 GHz could be achieved with current tuning alone. However, the enhanced tuning range due to thermal tuning also guarantees that the desired wavelength can be provided in spite of production variances of the DFB laser wafers and stimulation of competing optical modes in the laser's resonator.

The amplifier currents have no significant influence on the optical spectrum as long as the amplifier is saturated. Without an optical input, the PA emits non-coherent ASE with a peak emission at its gain maximum. When saturated, the ASE background of the PA is reduced and the MO signal is amplified. Figure 6.4a shows the single spectrum for $I_{MO} = 0$ mA and $I_{MO} = 270$ mA. In the blue curve, the broad ASE output is clearly visible but is significantly reduced when the MO signal is injected. However, the red curve also reveals that the gain maximum of the amplifier at 787 nm is red-shifted compared to the carrier signal at 780.241 nm. This causes an increased ASE emission because carriers at the gain maximum wavelength are not entirely cleared. The ASE power will not exceed - 40 dB suppression compared to the carrier emission. In the

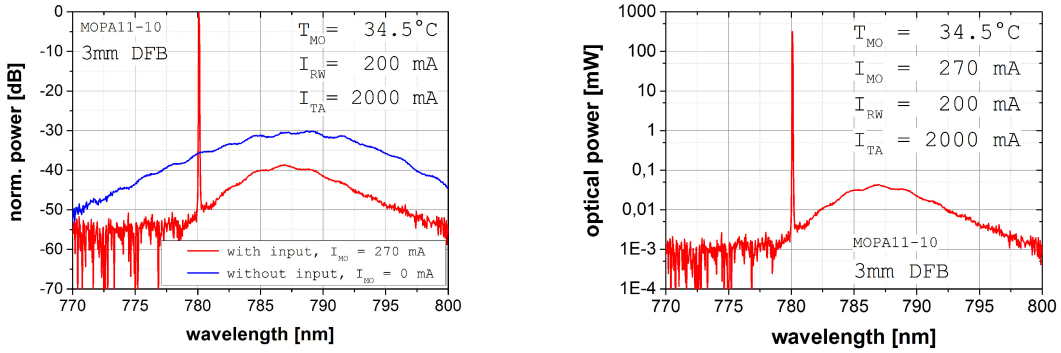

(a) (b)

Figure 6.4: (a) Comparison of spectral output with (red) and without (blue) input from the master oscillator. (b) MOPA spectrum calibrated, optical power in mW vs. wavelength.

range of ± 1 nm around the MO carrier emission, the SMSR is even at 50 dB. Emission outside this range is not of interest due to the nature of quantum experiments as the atoms will not be influenced by these wavelengths. The single-spectrum measurement in figure 6.4 allows for the estimation of the total ASE power when the total emission power is known, which in this case was 945 mW. Figure 6.4b shows the same curve but calibrated in mW. It has to be mentioned that the maximum peak power shown in this plot does not reflect the actual beam power because the linewidth of the MO is much smaller than the resolution of the OSA, see section 6.1.3. However, the calibration is based on the assumption that the integrated power of the spectrum matches the power measured with the power meter. With the calibrated power in mW, the ratio between the total ASE emission power in the wavelength range between 770 nm and 800 nm and the peak emission power can be estimated. The ASE emission adds up to be in total 16 mW, the ratio between peak power and ASE power is 17.5 dB. With that, the ASE is clearly not dominating the laser module's emission and can be neglected.

6.1.3 Linewidth

The laser linewidth, introduced in section 3.1.3.4, indicates the spectral stability of a laser. A detailed analysis of the spectral stability can be done by measuring the frequency noise power spectral density (PSD) of the laser and is described in [111, 112]. Based on the PSD of the frequency noise, the FWHM of the linewidth and the white noise floor of the linewidth can be determined. From that the technical linewidth, based on the FWHM value, and intrinsic linewidth, based on the white noise level, can be calculated.

6.1.3.1 Measurement Setup

Various methods exist to measure the linewidth of lasers. Fabry-Perot interferometers [113] and beat note measurements [114] are the most common techniques. How-

ever, both suffer from the problem of frequency drifts that are typically larger than the linewidth of the lasers on the time scales that are typical for linewidth measurements. In optical frequency discriminators the frequency resolution is dependent on the long-term frequency stability of the laser, requiring active frequency stabilization in order to be able to measure the linewidth. However, frequency stabilization affects the PSD for frequencies smaller and equal the servo bandwidth of the servo loop, distorting the frequency noise analysis for low Fourier frequencies.

In the heterodyne measurement method, the laser beams of two comparable lasers, the device under test (DUT) and the optical local oscillator (OLO), are mixed on a high speed photo diode, the photo diode signal then is processed by a RF spectrum analyser, as shown in figure 6.5a. However, RF spectrum analysers cannot cope with frequency drifts of the carrier frequencies of both lasers. The spectrum at various RF frequencies is recorder sequentially, resulting in the problem that different parts of the RF spectrum belong to different beat note carrier frequencies. With that, the RF spectrum analysis shows systematic deviations. In addition, amplitude noise can be misinterpreted as frequency noise.

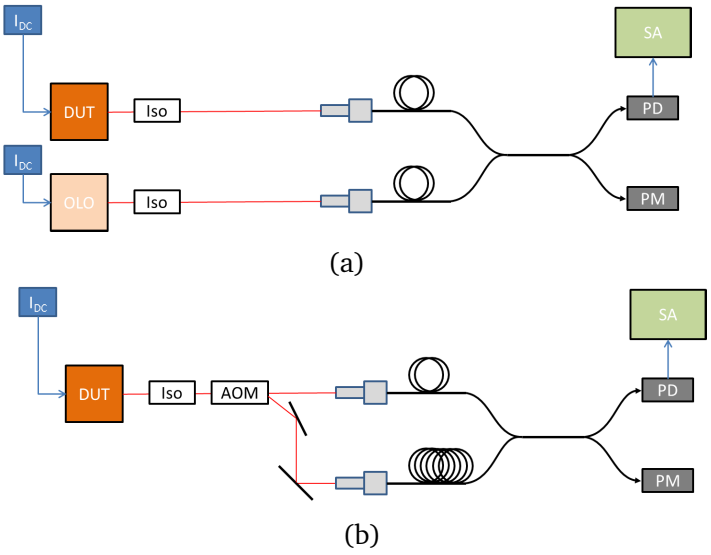

Figure 6.5: Measurement setup for linewidth measurement: Beat note with frequency difference capable for photo diode (PD) detection is created either with (a) lasers DUT and OLO or (b) self-delayed with a DUT, modulated with an AOM, first order output of AOM is delayed with a long fibre. PD signal is analysed by signal analyser (SA) which delivers IQ-data.

For beat note measurements, the self-delayed heterodyne (SDH) technique [115] is an approach to overcome frequency drifts. With the SDH technique only the DUT laser is required, as depicted in figure 6.5b. An acusto-optical modulator (AOM)[1] splits the DUT laser beam, shifting the frequency of the first diffraction order beam output

[1]We use the AOM Intra Action ATM-804DA2B

by several MHz [2]. One of the beams is delayed by a long fibre in order to provide an incoherent reference beam for the analysis, both beams are mixed again on a high speed photo diode. The measured frequency noise PSD values have to be divided by $2\times(1-\cos(2\pi f\cdot T_{delay}))$ in order to compensate for the superposition of two electrical fields on the photo diode [116], and to obtain the laser's PSD. That requires the exact knowledge of T_{delay} and excludes frequencies from the analysis which are integer multiples of $1/T_{delay}$ due to division by zero. This, again, leads to an incomplete frequency noise PSD analysis. With a $L = 2\,\mathrm{km}$ long polarization maintaining fibre as delay line and a refractive index n of 1.5 for the fibre material the $T_{delay} = nL/c$ would be $10\,\mu\mathrm{s}$. A resolution limit for SDH measurements is the inverse delay time, resulting in a limit of 100 kHz. However, for the determination of the technical and intrinsic linewidth values, these limitations are not relevant.

Instead for recording a PSD with a spectrum analyser to estimate the white noise floor and to record the beat note spectrum separately in order to estimate its FWHM, we chose the I-Q data approach described by Schiemangk in 2014 [112]. Only a single measurement is required to acquire a data set from which both the phase noise and the beat note spectrum for various integration times can be reconstructed. Also the misinterpretation of amplitude noise can be avoided. A heterodyne measurement setup, as depicted in figure 6.5, can be used without frequency stabilization being necessary. In addition, the I-Q method allows the linewidth characterization over all frequencies of the aimed bandwidth of free-running laser modules when using a heterodyne setup, as shown in figure 6.5a.

In our measurements a beat note signal was generated by superimposing the beams in an x-coupler either of an OLO and the DUT, or self-delayed, which then are sent to a fast photo detector (New Focus NFO-1554-B). The voltage of the photo diode corresponds to

$$V_{beat}(t) = V_0(t)\cdot\cos(\Delta\omega t + \varphi(t)) \tag{6.1}$$

with voltage amplitude V_0, the differences of the angular frequency of the two laser beams $\Delta\omega$ and phase $\varphi(t)$.

The second output of the X-coupler can be used for power or spectrum monitoring. The beat note signal is then recorded by a RF spectrum analyser (Rhode & Schwarz FSW). The spectrum analyser down-converts the signal to an intermediate frequency, digitizes this signal, and generates the in-phase (I) and quadrature (Q) components:

$$I(t) = \tilde{V_0}(t)\cdot\cos(\Delta\tilde{\omega}t + \varphi(t)) \tag{6.2}$$

$$Q(t) = \tilde{V_0}(t)\cdot\sin(\Delta\tilde{\omega}t + \varphi(t)) \tag{6.3}$$

where $\tilde{V_0}$ is an adapted amplitude and $\Delta\tilde{\omega}t + \varphi(t)$ corresponds to the instantaneous signal phase. These I-Q components are recorded and can be accessed for further data analysis.

The instantaneous signal phase can be extracted from the I-Q data with $\arctan(Q/I)$. The linear component $\Delta\tilde{\omega}t$ can be subtracted from the signal phase after obtaining a linear fit to the remaining signal. The phase noise PSD $S_\varphi(f)$ is calculated from the

[2] 78 MHz in our setup

remaining $\varphi(t)$ with a fast Fourier transformation and finally can be transformed into frequency noise PSD $S_\nu(f)$ by multiplying with f^2, since

$$S_\nu(f) = S_\varphi(f) \cdot f^2 \tag{6.4}$$

The intrinsic linewidth of the laser module corresponds to the white noise floor F of $S_\nu(f)$ multiplied by $\pi/2$.

$$\Delta\nu_{intrinsic} = F \cdot \frac{\pi}{2} \tag{6.5}$$

The beat note spectrum can be reconstructed with a Fourier transform of the I-Q signal. With the beat note spectrum the FWHM linewidth can be determined. This is done by fitting a Voigt profile to the beat note spectrum. According to Mercer [116], the relationship between the Voigt linewidth $\Delta\nu_V$, the Gaussian linewidth $\Delta\nu_G$, and the Lorentzian linewidth $\Delta\nu_L$ can be described with

$$\Delta\nu_V = \frac{1.0692\Delta\nu_L + \sqrt{0.866639\Delta\nu_L^2 + 4\Delta\nu_G^2}}{2} \tag{6.6}$$

$$\approx \Delta\nu_G \tag{6.7}$$

whereas the Lorentzian linewidth corresponds to the intrinsic linewidth, $\Delta\nu_L = \Delta\nu_{intrinsic} \ll \Delta\nu_G$.

In order to achieve the FWHM linewidth of a single laser, the FWHM value of $\Delta\nu_G$ has to be divided by $\sqrt{2}$, since the FWHM of the two superimposed Gauss profiles is $\sqrt{2}$ times the FWHM value of a single Gauss profile.

$$\Delta\nu_{FWHM,Voigt} = \frac{1}{\sqrt{2}}\Delta\nu_V \tag{6.8}$$

6.1.3.2 Measurement Results

Figure 6.6a shows a frequency noise PSD of a MOPA (blue graph) and the reconstructed beat note spectrum of the self-delayed heterodyne measurement (red graph) with I-Q analysis. The analysis is limited to 100 kHz due to the limitations of the delay line, as explained earlier. The DFB laser in this laser module has a length of 3 mm and was driven with 270 mA at 34.5 ° C. The PSD shows a 1/f characteristic, as predicted by [116], for frequencies $<$ 1 MHz, the white noise characteristic is observed for frequencies $>$ 10 MHz.

The influence of the chip length on the spectral behaviour can also be found in the linewidth measurements. Figure 6.6b shows the FWHM and intrinsic linewidth for 1.5 mm diodes (marked with red lines) and 3 mm diodes (marked with black lines). The x-axis shows the DFB output power, measured before micro-isolator integration. Both depicted intrinsic linewidths show a 1/P behaviour, as predicted in equation 3.25. The 1.5 mm DFB has a minimum intrinsic linewidth of 106 kHz at an output power of 120 mW. The linewidths of the 3 mm chip are, expectedly according to [88, 89], even narrower due to the larger resonator length. The intrinsic linewidth is 14 kHz at a comparable output power. The FWHM linewidth remains constant at a level of 1.16 MHz for the 1.5 mm DFB module and 386 kHz for the 3 mm DFB module.

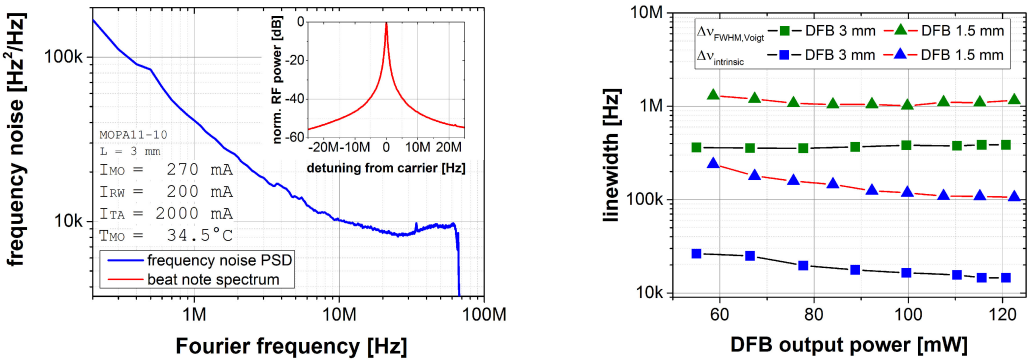

Figure 6.6: Linewidth of MOPA: frequency noise PSD and beat note spectrum (a) and linewidth distribution against MO output power (b)

6.1.4 Modulation Capability of the MIOB

As described in section 4.1.2.2, the MIOB provides an electrical interface that allows the modulation of the MO injection current on-board the MIOB through a transistor. By applying a signal at the transistor modulation interface (MMOD) and through that to the transistor's gate, the transistor branches off a fraction of the DC injection current, supplied by the MDC interface.

In order to test the effect of the transistor, a MIOB with an integrated 3 mm long DFB laser as MO but without an amplifier was chosen. A DC voltage in the range of + 0.5 V to - 2.5 V was applied at the MMOD interface additionally to the current input of 270 mA at the MDC interface. The output power and wavelength of the MO were recorded for varying transistor gate voltages, as depicted in figure 6.7. As expected for a normally-on n-channel JFET transistor, the optical output power is at its minimum when the gate voltage is maximized. If the gate voltage is smaller than the source voltage, the source-drain-current will be reduced. The transistor "closes", depleting less current from the laser diode supply. Since the source is connected to ground potential, the gate voltage has to be negative. Less injection current results in less optical output power, but also, as shown in section 6.1.2, in a tuning of the laser emission frequency. Both can be observed in figure 6.7, confirming the depletion of the injection current. Between - 1 V and + 0.5 V a linear tuning can be approximated. A linear fit of the emission frequency reveals a frequency deviation of 8.9 GHz/V for a 3 mm long DFB laser for modulation intensities in the range of - 1 V and + 0.5 V, depicted in red in figure 6.7. Since the spectral current tuning range is given in section 6.1.2 with 1.2 nm/A, corresponding to 591 GHz/A, the current depletion can be calculated to be 15 mA/V. With that and the known current tuning coefficient for 1.5 mm long DFB diodes the effect of the MMOD based current depletion can be estimated to be 18.6 GHz/V for shorter laser diodes.

For gate voltages smaller than - 2 V hardly any changes in either the output power or the emission frequency can be detected. It can be concluded that the transistor is closed completely at this gate voltage, the entire injection current is supplied to the

laser diode.

This test reveals that the common-source transistor circuit operates as expected. The recommended signal intensity for the modulation signal is in the range of 0 V to - 1 V.

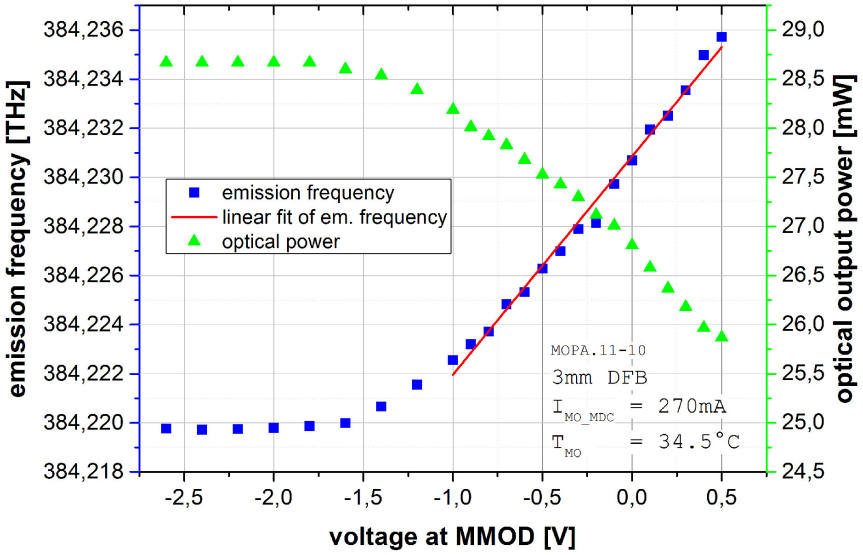

Figure 6.7: DC Influence on MMOD voltage on wavelength and output power of a 3 mm long DFB. The output power is measured behind a 60 dB μ-isolator.

6.2 Environmental Tests

Environmental stress tests are important to prove the suitability of a component for its operational environment. For operation in space very often the requirements are based on the environment in the transport vehicle, like the rocket, or the spacecraft, such as described in section 2.1.3. In addition to these mission requirements, there are general qualification specifications, e.g. the specifications of the European Space Components Coordination (ESCC) [117][3], which specify the test methods that should be used for qualification of the hardware. The mechanical stress tests with random vibration and shock are of particular importance for sounding rocket missions. Complex modules, using different materials and assembly technologies come with the risk of falling apart or simply breaking when being subjected to mechanical stress. Thermal loads become relevant during transportation and storage for sounding rocket campaigns. Different

[3]Not to be confused with the ECSS, the European Cooperation for Space Standardization which aims at "a coherent, single set of user-friendly standards for use in all European space activities" [118]. The ESCC, however, provides procedures and standards for "the production and use of electrical, electronic and electro-mechanical components suitable for use in space" [119]

materials come with different values for the coefficient of thermal expansion (CTE). A differential thermal expansion adds stress to the bond areas between parts, potentially causing damage to bonds or at least misalignment of the optical components. Both thermal and mechanical tests were performed and are described in this section. These tests exceed the requirements for the TEXUS [47] and MAIUS sounding rocket mission in order to find limitations and prepare for future space missions.

Besides mechanical stress tests and temperature stress tests, radiation stress tests are important in the qualification process towards qualification of a component [117]. Semiconductor elements that operate high above the surface where the Earth's magnetic field is weaker compared to the surface are threatened by ionizing particles, causing single event effects. For microprocessors this can result in bit-flips or latch-ups [120]. In semiconductor laser diodes the impact of radiation causes an increasing threshold current and a decreasing output power [121], hence a degradation of the electro-optical performance, but typically no fatal damage. However, radiation hardness tests are not relevant for sounding rocket experiments because the exposure time in space is, with approximately 15 minutes, very short compared to satellite missions with several years of operation times. With an apogee of 260 km the sounding rocket also does not reach the Van Allen belts. With a short operation time and the close vicinity to Earth the dose of radiation impact can be neglected.

6.2.1 Definition of Test Parameters

The random vibration test and temperature cycling test were performed with varying intensities in order to first ensure the performance according to the load specifications defined by the sounding rocket environment [47], and in a second step, to find the limitations of the technology. Additionally to the random vibration tests and temperature cycles, a mechanical shock test was performed. The specifications of the stress test campaign in the second step are based on the ESCC "Evaluation Test Programme Guidelines for Laser Diode Modules" [117]. These guidelines point out designated MIL specification methods and test parameters appropriate for qualifying diode laser modules. Table 6.1 gives an overview of the environmental tests performed in this work. The tests took place in the order given in the table, starting with an 8 g_{RMS} vibration test and finishing with the –55 °C ... +85 °C temperature cycles. The electro-optical performance of the DUTs was recorded before and after each stress test.

6.2.1.1 Random Vibration Tests

Two random vibration tests have been performed. The one is carried out at 8 g_{RMS} load level, which corresponds to the qualification level for the TEXUS sounding rockets. The load profile of this test was determined experimentally in a TEXUS mission. The profile of the second test, at 30 g_{RMS}, was defined by a more general test procedure, covering a broad band of vibrating frequencies. The profiles are given in table 6.2.

[4] +15 °C corresponds to the dew point of water on cold surfaces when the surrounding has a humidity of 50% a room temperature. +70 °C is the maximal temperature defined by the ESCC [117].

Test	Duration	Repetition	Specification
random vibration			
8 g_{RMS}	2 min / axis	1	DLR, TEXUS mission [47]
30 g_{RMS}	3 min / axis	1	MIL-STD-202 (Method 214; Condition I-H) [122]
half sine shock	0.5 ms / axis	3	MIL-STD-883 (Method 2002; Condition B) [123]
temperature cycles			
+15 °C ... +70 °C	≤ 12 K / min	10	laboratory storage[4]
–30 °C ... +45 °C	2 K / min	10	DLR, TEXUS mission [47]
–55 °C ... +85 °C	2 K / min	10	MIL-STD-883 (Method 1010; Condition A) [123]

Table 6.1: Overview of environmental tests performed in this chapter

In addition to the tests on system level, all modules integrated into the rocket payloads of FOKUS and MAIUS run through the same qualification test at 8 g_{RMS} on subsystem and unit level. Although it is not required by the TEXUS stress test specifications, one MOPA module was fully operated when performing the first vibration test. The output power was recorded before, during, and after the vibration test.

The second random vibration test specifications are based on the ESCC document [117], referring to the MIL-STD-202, Method 214 [122]. However, since the aim of this test was not the qualification according to ESCC regulations but to show the ability for future qualification, some details of the specification were modified in order to increase the chance of survival of the modules. The duration of the test phase was reduced from 7.5 minutes, as defined by the ESCC [117], to 3 minutes, as suggested in the MIL-STD-202 method 214-H test definition to which the ESCC test refers. In addition, the modules were not operated during this test.

Both tests were performed with a 35 kN TIRA shaker. Before and after the random vibration test, the vibration frequency was swept in order to identify resonances in the modules and verify that these resonances have not changed after the random vibration test. Each test was performed in the x, y and z-axis of the module.

Test	Frequency Range	PSD Component
8 g_{RMS}	20 – 400 Hz	0.0045 g^2 / Hz
	400 – 600 Hz	0.0675 g^2 / Hz
	600 – 1300 Hz	0.0045 g^2 / Hz
	1300 – 2000 Hz	0.0675 g^2 / Hz
30 g_{RMS}	50 – 100 Hz	+6dB/oct
	100 – 1000 Hz	0.6 g^2 / Hz
	1000 – 2000 Hz	-6dB/oct

Table 6.2: PSD loads per frequency range of random vibration test

During the $8g_{RMS}$ test, the output power of one MOPA was recorded. To do so a macroscopic collecting lens with a diameter of 2 inch compensated the movement of the vibration table by focussing the optical output beam to a photo detector mounted to an Ulbricht sphere. The Ulbricht sphere prevents saturation of the detector by distributing the insert beam equally to its inner surface. The data was recorded with a sample rate of 300 Hz, limited by the available recorder. The temperature of the MOPA was not stabilized during the test.

6.2.1.2 Shock Tests

Additionally to the random vibration tests, a half-sine shock test according to ESCC and MIL-STD-883; Method 2002; Condition B [117, 123] was performed. A pivot-mounted hammer applies a half sine shock with an amplitude of 1500 g and a duration of 0.5 ms to block that transfers the shock to the DUT mounted in a pre-defined direction. The shock is applied three times to each axis in each direction, resulting in 18 shocks per module.

6.2.1.3 Thermo Cylce Tests

The temperature cycles were performed with a CTS T-65/50 test chamber. The first test, testing for laboratory storage environments between +15 ° C ... +70 ° C, was performed with a dwell time of 40 min, but with the maximal slope of up to 12 K/min.

The second test parameters are given by the experimental environment of a TEXUS mission. –30 ° C might occur under transportation and recovery of the payload. The upper temperature limit of +45 ° C is the maximal operation temperature of the modules in the experiment. The dwell time was chosen to be 70 min, resulting in a slope of 1.9 K/min. The number of cycles was not defined in the TEXUS environmental specifications. However, a number of 10 cycles should exceed the number of temperature cycles the experiment is exposed to during the mission and therefore covers the stress limits.

The third test, again, is based on general qualification specifications, namely the MIL-STD-883; Method 1010; Condition A, giving a temperature range of –55 ° C ... +85 ° C. The slope, again, was 2 K/min, with a dwell time of 80 min for the rising edge and 100 min for the falling edge. The hold time at the minimum temperature was extended to make sure that the test chamber reaches the minimum temperature. This test is also suggested in the ESCC document, but with a maximal temperature of 70 °C. Since the modules have passed the 70 ° C in the first test, we decided to increase the temperature range even further to investigate the limitations of the DUT modules.

6.2.2 Results of Environmental Tests

All laser modules, integrated in the FOKUS and MAIUS experiment, passed through the qualification tests on system level as defined in the TEXUS specification [47].

Two additional laser modules were tested under more serve test conditions, such as higher random vibration loads in the vibration test, shock test, and temperature cycles.

Before and after each test, the output power and spectral behaviour were recorded.

6.2.2.1 Results of the Mechanical Stress Test

The visual inspection of the MOPAs did not reveal any changes on the module, the lenses and isolators as well as the cables attached to the electrical interface remained in place.

After the random vibration tests and shock tests no significant modifications of the performance could be observed. The MOPA output power remained stable at the WP, it rather increased slightly from 1.4 W before vibration and shock tests to 1.48 W after the tests.

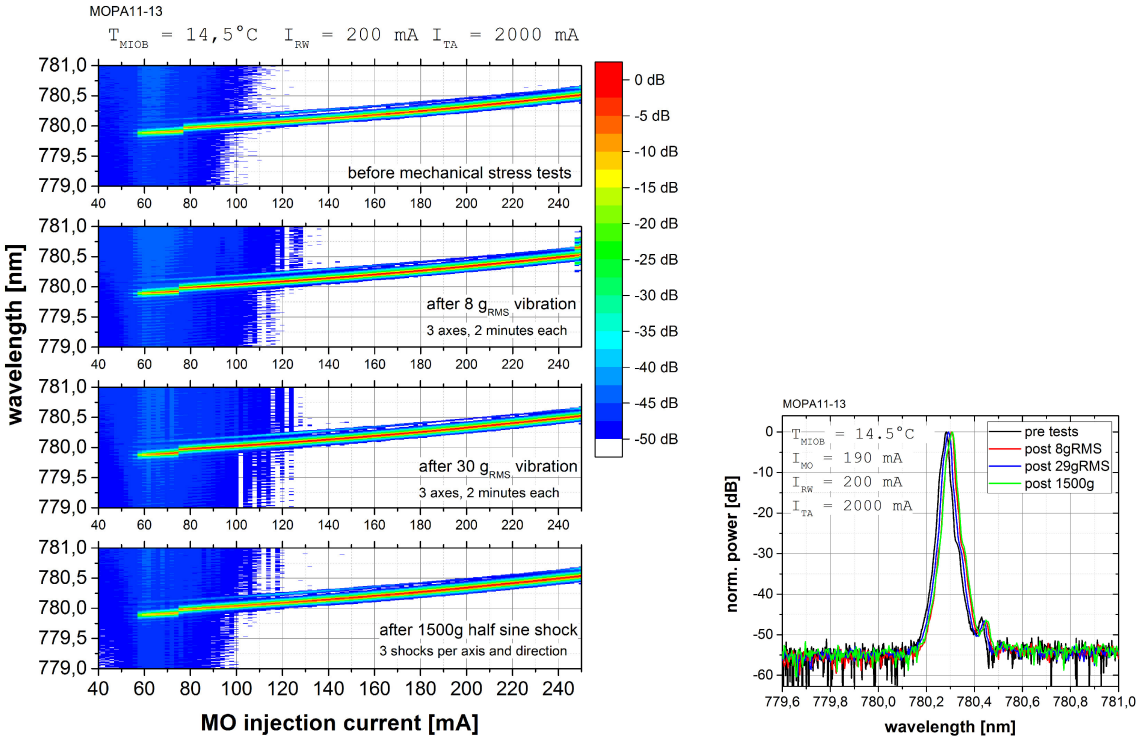

(a) (b)

Figure 6.8: Spectral performance of DUT before and after vibration and shock tests. (a) spectral map, (b) single spectrum at WP. Performance remained stable.

Figure 6.8a shows the spectral behaviour of the MOPA recorded after each random vibration test and the shock test. No changes, such as shifting of the mode hops, appearing of additional mode hops, and shifted threshold current, in the spectrum map could be observed. Figure 6.8b shows the single spectrum at the WP. It can be observed that the noise level for emitted light > 0.5 nm next to the peak is stable below -50 dB. The side-mode is suppressed by > 45 dB in all measurements. However, it also can be observed that the wavelength of the peak maximum is scattered by 26 pm, without a

tendency during the test series. The resolution bandwidth of the OSA is 10 pm, and the measurement step size of 2 mA, corresponds to approximately 6 pm according to section 6.1.2. This is not sufficient to explain this wavelength scattering alone. The main contribution to the variance of emission wavelength is based on different temperatures of the submount of the DUT. In module MOPA11-13 the thermal resistance of the MO submount to the MIOB appeared to be higher than in the other modules, resulting in a poor thermal dissipation of the heat generated by the laser diode, and in problems when stabilizing the temperature of the module to the measures of the submount based temperature sensor. Therefore the module was stabilized to the sensor at the MIOB, resulting in varying temperatures at the MO submount. The temperature difference between the measurements amount to 0.38 K, corresponding to 20 pm wavelength tuning, as described in section 6.1.2. With that, the module MOPA11.13 is not qualified for high precision measurement applications, still, together with the measurement uncertainties named above the emission wavelength variation can be explained. The FWHM and intrinsic linewidth also stayed stable after the tests.

Since the spectral deviations can be explained with the uncertainties in the measurement setup and the optical output power was stable after all mechanical stress tests, it can be stated that the mechanical stress tests did not influence the behaviour of the laser module.

As described in section 6.2.1.1, the optical output power of one MOPA module was recorded during the TEXUS launch qualification test at 8 g_{RMS}. The aim of this test was to show that the MOPA modules can be operated during the rocket launch.

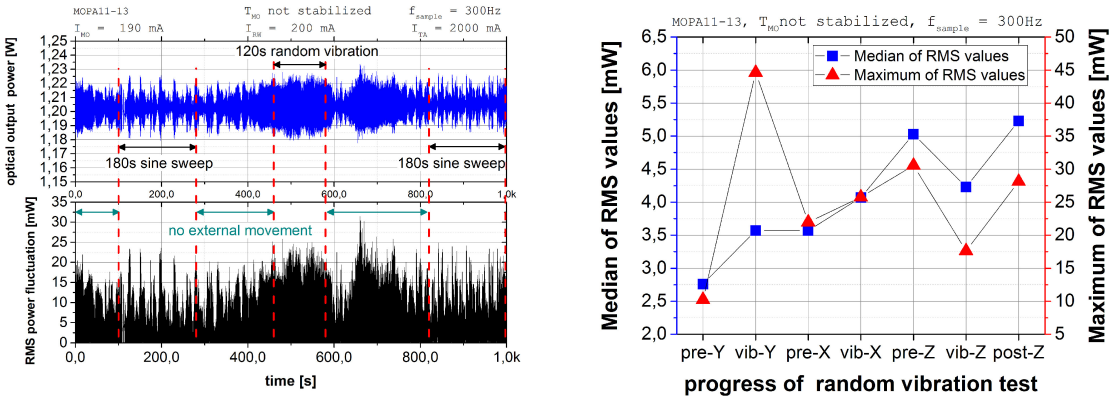

(a) (b)

Figure 6.9: (a) Power recording (above) and RMS deviation (below) of a MOPA emitting during lateral (along the x-axis of the shaker) vibration test of 8g_{RMS}, (b) RMS values of these power recordings before, during and after the vibration tests. pre: before the test, no external movement, vib: random vibration run, post: after the test, no external movement. X,Y, and Z are the directions of movement. The longitudinal (Y) vibration run was performed first.

In its upper panel, figure 6.9a shows in blue the raw data of the power measurement for the x-axis (lateral) vibration run, including the sine-sweep resonant search before

and after the random vibration run. In black, the root mean square (RMS) power fluctuation of this data is presented in the lower panel of this figure. The resonance search was carried out starting at second 100 and 820 and lasted for 180 s each. The random vibration test was performed between t = 460 s and t = 580 s. During the times marked with the green arrows, no external force was applied to the modules. Before, during and after the vibration test the MOPA emitted with a median of 1202 mW with a maximal peak-to-peak variation of 59 mW. It can be seen that the optical output power stayed stable also during the random vibration test, the coupling of the MO-beam into the power amplifier was hardly influenced by the external vibration of the environment. However, both the median and maximum RMS fluctuation of the power values increased slightly during the test, from a median of 3.5 mW before the random vibration tests to 4 mW during the random vibrations. The maximum RMS deviation of 22 mW before the vibration was overtaken with 25 mW during the test. However, the maximum RMS deviation of 31 mW appeared only after the random vibration run when the shaker was stood still. This shows that externally applied vibrations are not the main source of power fluctuations in this setup. The temperature of the MOPA module was not stabilized, and varying temperature has an influence on the output power, as described in 3.1.3.3. After the random vibration run, the DUTs were inspected visually. Draught arising from open doors and moving people can be the cause of the increased power fluctuation after the random vibration test of the lateral (X) axis as well as the internal cooling mechanisms of the shaker apparatus.

Figure 6.9b shows the evolution of the power fluctuation in RMS values during the 8 g_{RMS} test campaign. Also for the Y (longitudinal) and Z (vertical) axis the maximum deviation of the median power value did not exceed 45 mW, stating that there also was no interruption of the power emission during the random vibration runs of these axes. However, the power fluctuation increases during the test campaign, from 2.75 mW to 5.25 mW. This can be explained by displacements in the nm range of the optical components of the MOPA module due to the vibrational loads, influencing the beam coupling and the clearing of photons in the amplifier.

Unfortunately it was not possible to record the optical output power with a sampling rate higher that 300 Hz. Since the maximum vibration frequency is 2 kHz, a sampling rate of at least 4 kHz would have allowed a detailed analysis of the applied vibration frequencies on the power fluctuation.

6.2.2.2 Thermal Stress Test Results

Two MOPA modules were tested in a thermal test chamber according test parameters given in table 6.1. It was expected that thermal cycling causes misalignment between the optical and electro-optical components of the laser module due to CTE mismatch of the different materials and adhesives used. Both modules still fulfilled the specifications after the test campaign. However, a degradation in the in-coupling of the beam from the master laser into the amplifier could be observed for both modules, as shown in figure 6.10a. This figure illustrates the optical output power for various MO injection currents and with that the saturation behaviour of the amplifier. After the first thermal cycling the saturation behaviour, marked with red, follows the satu-

ration behaviour previous to the thermal cycling campaign, marked in black. But after the second thermal cycling the graph flattens, in green and blue, indicating that the amplifier saturation requires a higher MO injection current, reducing the in-coupling efficiency. Despite the reduction of the in-coupling efficiency the total optical output power remained stable, as depicted in figure 6.10b. The degradation of the in-coupling efficiency is likely caused by misalignment of the lens positions. The adhesive fixating the lenses to the MIOB is specified for a temperature range of - 15 °C to + 60 °C before ageing [124]. The DUTs were not aged before test. This may have caused a softening of the adhesive, allowing the lenses to change their position slightly.

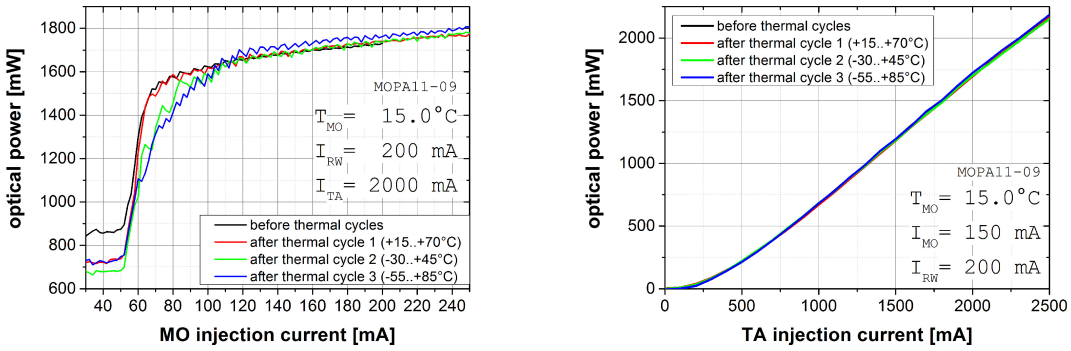

(a) (b)

Figure 6.10: Output power development after several thermal cyclings. (a) over TA injection current, (b) over DFB injection current

The thermal stress did not affect the spectral behaviour of the DFB lasers as the misalignment of the lenses did not affect the DFB operation. The saturation of the amplifier suppresses the ASE background on the same level as in prior tests at the WP settings. The linewidth also remained stable during and after the tests.

With the relatively small number of 10 thermal cycles per temperature range, the laser modules remained within the specifications and proved that they can withstand temperatures in the range of -55 °C ... +85 °C. This is more than enough for sounding rocket missions and would also be enough for short term space missions such as the (no longer existing) Space Shuttle experiments [125] or operation on the International Space Station. For long-term satellite missions however, the need for temperature stabilization of the laser module is inevitable also when not operated. Alternatives for the adhesive that keeps the optics in place, such as soldering the lenses [126], could be evaluated to avoid the thermal degradation of the laser modules performance that show an effect in these test.

6.3 Conclusion of Characterization and Stress Tests

The characterization process shall verify the performance of the laser modules according to the requirements of the application. Table 6.3 lists the characterization results

of the laser modules that correspond to the requirements listed in tables 2.1 and 2.2. Measurement conditions and additional analysis are described earlier in this chapter. As listed in table 6.3, all requirements can be fulfilled. This does not only apply to the laser modules presented in this chapter but to all laser modules produced in the course of this thesis.

parameter	**required value**	**achieved value**	**comment**
		electro-optical	
wavelength (λ)	780.241 nm	780.241 nm	with ± 0.2 nm current tuning range at const. T_{MO}
FWHM linewidth	$\leq$ 6 MHz	1.16 MHz	for 1.5 mm long DFBs
		386 kHz	for 3 mm long DFBs
tunability around WP	100 GHz	880 GHz	for 1.5 mm long DFBs
		740 GHz	for 3 mm long DFBs
optical power per MOPA	$>$ 1 W (CW)	1.5 W	at I_{TA} = 2 A, T_{MO}=35° C
optical power of MO	$>$ 10 mW (CW)	$>$ 20 mW	at $I_{MO} < 200$ mA, T_{MO}=36° C
max. power consumption	7.2 W	typ. 5.7 W	at WP operation
		environmental	
vibration loads	8.1 g_{RMS}	passed	also 29 g_{RMS} passed
shock loads	$\geq$ 250 g	1500 g passed	
WP temperature	$\geq$ 35 °C	achieved	
storage temperature	–30 °C ... +45 °C	passed	–55 °C ... +85 °C passed

Table 6.3: Results of laser module characterization and stress tests compared to requirements

For the environmental stress tests, the test parameters were enhanced in order to apply to recommended test specifications for future applications and to find the boundaries of environmental conditions of the laser modules. All laser modules that went through the mechanical and thermal stress tests kept their specified performance after each test. The qualification tests for the sounding rocket missions were passed without affecting the performance at all. The extensive mechanical stress tests also triggered no change in behaviour. However, the thermal stress tests for temperatures below zero revealed a degradation in the in-coupling of the MO beam into the amplifier. This degradation does not affect the performance at the WP and therefore is not critical. However, for storage under these conditions preventive measures should be taken to guarantee long-term performance of the laser modules.

Chapter 7

Evaluation of Sounding Rocket Missions

On 23rd of April 2015, the TEXUS 51 rocket was launched. One of the four payloads on board this rocket was the FOKUS experiment, including the first semiconductor laser frequency locked on an alkali transition line operated in space. The Rb spectroscopy was driven by one of the DFB-MO laser modules, developed in this thesis.

On 22nd of January 2017 the MAIUS rocket was launched and created the first BEC in space. This rocket hosted 5 fully integrated MOPA modules and one DFB-MO module that were developed and characterized in this thesis.

With FOKUS and MAIUS, our laser modules have proven their functionality in space operation and obtained technology readiness level (TRL) 9 for sounding rockets. The experimental setup and flight environment were already described in chapter 2.1. This chapter presents the performance data of the laser modules and results of the missions.

7.1 FOKUS Mission

7.1.1 Qualification and Ground Operation

The rubidium reference system consists of a DFB laser diode integrated in a MIOB and a Zerodur based spectroscopy module, hosting a Rb gas cell and photodiodes as described in section 2.1. After integration the system was subjected to random vibration tests with 8.1 g_{RMS}, thermal cycling tests between 5 °C and 40 °C. These tests were simulating launch conditions of the rocket and storage conditions of the assembled payload. The system passed all tests [42].

In order to perform a LPI experiment, precision measurements of the path differences of the two clocks are necessary. Long-term drifts of the clock frequencies limit the accuracy of the measurement. Main contribution to frequency drifts are the fluctuation of the locking point of the Rb laser, but also drifts of the reference clock (CSAC) and uncertainties due to the light shift and Zeeman shift [42]. In order to verify the stability and reliability of the overall system, a long-term measurement of the clock differences was performed prior to the mission launch. To do so, the DFB laser frequency was stabilized on the Rb transition frequency and compared to the CSAC by means of the

frequency comb. The frequency difference of the Rb laser and the CSAC, characterizing the overall stability of the FOKUS system, was recorded over a time span of 200,000 s (65 h). Figure 7.1 shows the absolute frequency shift in the time domain, and relative stability of this measurement.

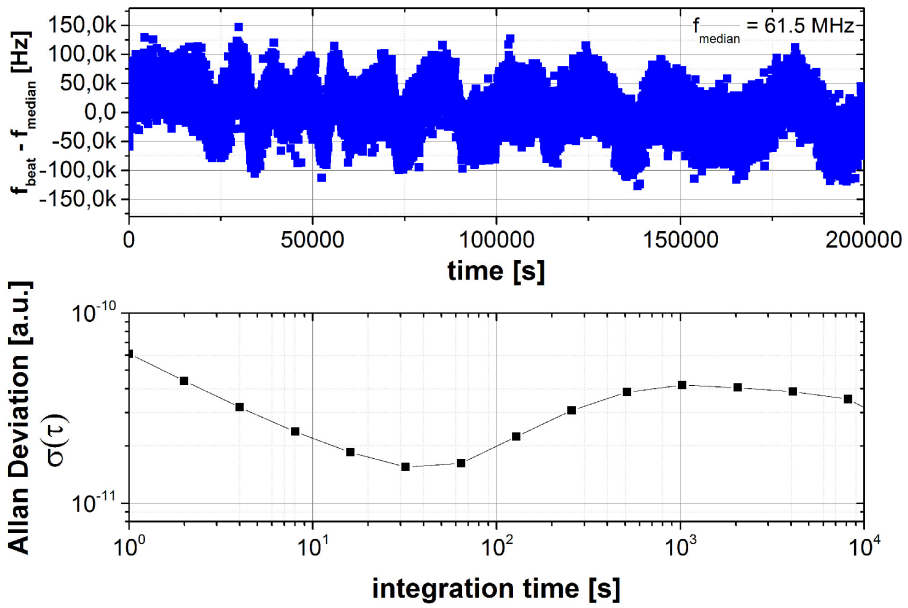

Figure 7.1: Frequency deviation of beat note signal from median (upper panel) and relative stability σ (lower panel) of long-term measurement of Rb reference system compared to the CSAC

In total, the frequency shifts by ± 150 kHz compared to the median frequency. The stability is estimated by calculating the Allan deviation. The Allan deviation is defined as the square root of the Allan variance, a widely accepted measure for frequency stability [127]. The Allan variance σ^2 is defined as

$$\sigma_y^2(\tau) = \frac{1}{2}\Sigma[(\bar{y}_{n+1} - \bar{y}_n)^2] \tag{7.1}$$

with $\bar{y}_n$ as the n^{th} average normalized frequency deviation from nominal frequency over a finite time interval with the length of τ [128]. With $\tau = 1\,s$ the systems instability corresponds to 6×10^{-11}, integrating with $1/\sqrt{\tau}$. However for the rocket flight, time scales in the range of $\tau = 1000\,s$ are relevant. The system provides a relative frequency instability of 5×10^{-11}.

The CSAC contributes to the instability with a specified Allan deviation of only 8×10^{-12} at 1000 s, the experiments stability therefore must be limited by the optical clock. The increasing Allan deviation for integration times > 60 s is caused by drifts in the analogue control electronics triggered by external temperature fluctuations [60]. Apart from this, the relative frequency instability corresponds to the frequency instability reported for other DFB laser system, as described in [129].

In order to improve the stability, the linewidth of the optical oscillator has to be improved. An approach could be to use an ECDL as optical oscillator as described in [130]. However, the improvement of the linewidth by factor 10 comes with the cost of spectral mode hops with distances of one free spectral range. This limits the spectral tuning range and demands a more complex locking scheme. The linewidth of the DFB laser diode matches the natural linewidth of the reference point for stabilization. To improve the stabilization, it is also suggested to choose another atom species, such as Al, transition ${}^1S_0, F = 5/2 \rightarrow {}^3P_0, F = 5/2$ [131], with a narrower natural linewidth and smaller sensitivity factor to minimize frequency shifts of the reference point. The stabilization can also be improved by optimizing the modulation bandwidth of the electronics and making use of the modulation interface provided by the MIOB. In FOKUS the modulation signal for frequency correction is added to the injection current externally. This limits the modulation bandwidth on a hardware level e.g. due to losses in the transmission cable.

The limited stability of the optical clock assembly also limits the accuracy of the experiment. However, the stability is sufficient to demonstrate the potentials of this technology.

7.1.2 The Flight Campaign

The FOKUS experiment is both a technology demonstrator and a proof of concept of a LPI experiment based on an optical clock in space. This section describes the mission process and the results of the flight campaign.

7.1.2.1 Mission Schedule and Performed Operations

The mission was launched at t_0 = 9:35:00 April 23rd 2015 CET from Kiruna Space Station. Table 7.1 gives a detailed overview of the flight events.

7.1.2.2 Results of the Flight Campaign

As described in table 7.1, the system was switched on and the DFB lasers frequency was stabilized on the Rb reference before launch. The frequency stayed stable until 330 s after launch, when frequency stabilization was deactivated on purpose. The peak accelerations during launch were 8.1 g and 12.6 g, through the first and second stage flight of the rocket. At t_0 + 330 s, a scan over the DFBs injection current was initiated to force the system out of the lock in order to test the auto-lock procedure during flight.

The graphs in figure 7.2 illustrate the PD readout signal (in blue) and the FMS error signal (in red). The constancy of the error signal and the photo diode signal together indicate that the frequency of the DFB laser remained stable and in lock over the launch period until the intended auto-lock test 330 s after launch. The dips in the error signal after 330 s are caused by ^{87}Rb F=2⇒F' transition. The frequency lock acquisition was achieved right after the scan was terminated and stayed in lock until shut down of the system at t_0 + 600 s. The Rb system performed as expected and without any problems,

mission time	**event**
t_0 - 5:30 h	switching on the system to thermalize
	locking of comb and Rb system, collection of ground reference data
t_0 - 10 s	system in secure state: Rb system locked, comb system unlocked
t_0	launch at 9:35:00 April 23rd, 2015 CET
t_0 + 13.4 s	separation of first rocket stage
t_0 + 59 s	separation of second rocket stage
	switching on the locking of comb system
t_0 + 72 s	μg regime reached, $< 10^{-4}$ g
t_0 + 84 s	comb frequency was locked
t_0 + 261 s	apogee reached
t_0 + 330 s	remotely controlled Rb spectroscopy scan
t_0 + 360 s	spectroscopy scan of Rb system finished
t_0 + 442 s	μg phase ended
t_0 + 600 s	system shut down for landing
t_0 + 884 s	touch down

Table 7.1: Time table of FOKUS mission flight

the technology demonstration of alkali references optical oscillators in space was hence successful.

In order to demonstrate a LPI experiment the fractional frequency difference $(f_1 - f_2)/f$ in a varying gravitational field ΔU has to be recorded. The frequency difference is related to ΔU through

$$(\beta_1 - \beta_2) = \frac{f_1 - f_2}{f} \cdot \frac{c^2}{\Delta U} \tag{7.2}$$

where β_i is a dimensionless parameter reflecting the sensitivity of each clock to a potential violation of the LPI.

$(f_1 - f_2)/f$ is the clock frequency comparison data which was collected until t_0 + 450 s, as long as both, the Rb system and the Er comb system were locked. The collected data is shown in blue in figure 7.3. A linear correction of a Rb lock drift of 122 Hz / s, probably caused by the increasing temperature of the payload, was subtracted from the data before plotting. The gap of data between 0 – 84 s is caused by the deactivated stabilization of the frequency comb system during launch. Between 330 s and 440 s after launch the Rb system was not stabilized due to the forced scan of the injection current of the DFB laser. At 478 s the frequency comp system was out of lock due to the landing procedure. The black line illustrates the gravitational potential $\Delta U/c^2$ the FOKUS experiment was travelling through, calculated from the altitude of the rocket and a spherical Earth model, using G as gravitational constant, M_{Earth} as Earth's mass, r_{Earth} as the radius of a spherical Earth, and h_{rocket} as altitude of the payload:

$$U(t) = \frac{G \cdot m_{Earth}}{r_{Earth} + h_{rocket}(t)} \tag{7.3}$$

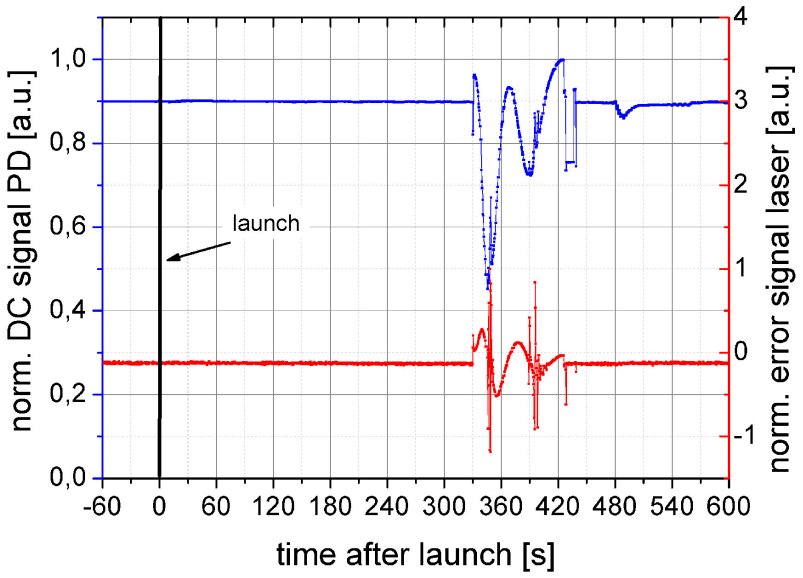

Figure 7.2: Photodiode read out (blue) and error signal (red) of the Rb reference system before and during flight. The laser frequency was stabilized before launch and stayed stable the entire mission except for the planned scan over the injection current.

The slow slope between 500 and 600 s is caused by the re-entry into the atmosphere. At 600 s the system was shut down for landing.

With the available data in figure 7.3, equation 7.2 and the least square method, the LPI violation indicator was estimated to be $(\beta_1 - \beta_2) = 0.186 \pm 0.260$. Although this estimation is orders of magnitude worse than state of the art experiments [1], the measurement principle, using optical clocks as references is not the limiting factor. The absolute clock evaluation is limited by long-term drifts of the reference frequencies, as discussed in section 7.1.1. The measurement accuracy can be improved by using state of the art optical clocks, and by enlarging the gravitational potential, e.g. with a space mission on a trajectory bringing the instrument close to the sun.

However, this was the first demonstration of an LPI test between two different types of clocks in space. The micro-integrated diode laser module performed as expected, providing the oscillator of the compact optical clock. This compact and robust optical clock is a pioneer in referencing frequencies in future spaceborne precision experiments.

7.1.3 Post-Flight Characterization of Laser Module

The DFB laser module, integrated into the Rb reference system in the FOKUS experiment, was characterized electro-optically before delivery (20th August 2012), after each of both 8.1 g_{RMS} vibration tests (4th and 10th October 2012) and after the flight

[1] $\Delta\beta = \beta_1 - \beta_2 < 10^{-6}$, shown by Fortier in 2007 [132]

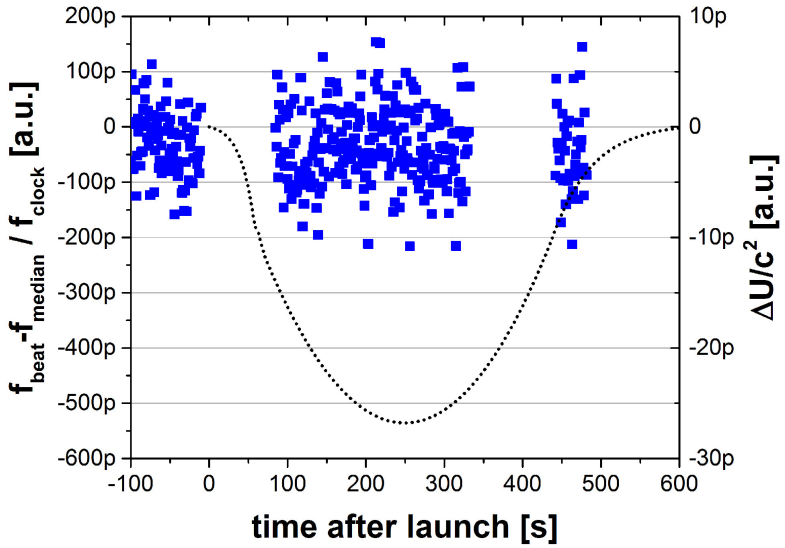

Figure 7.3: Relative changes of clock frequency comparison (blue squares) and gravitational potential (black dotted line) before and during flight. A linear drift of 122 Hz / s was subtracted from the optical frequency reading.

campaign (6th October 2015). The electro-optical characterization corresponds to the characterization described in section 6.1, including the optical output power, the emission spectrum and the linewidth characteristics (both FWHM and intrinsic) for various injection currents. However, after the flight campaign, it was not possible to measure either the free-space output power of the laser module or the total power in the fibre, because the laser module was integrated into the Rb module, the fibre coupled output of the laser module was spliced to a fibre optic splitter. The power values therefore are not directly comparable to each other.

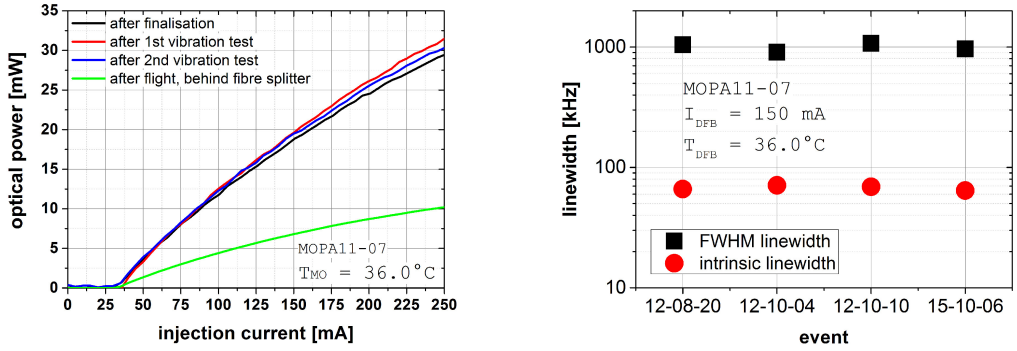

(a) (b)

Figure 7.4: Optical output (a) power and linewidth (b) of FOKUS laser module before and after mechanical stress tests.

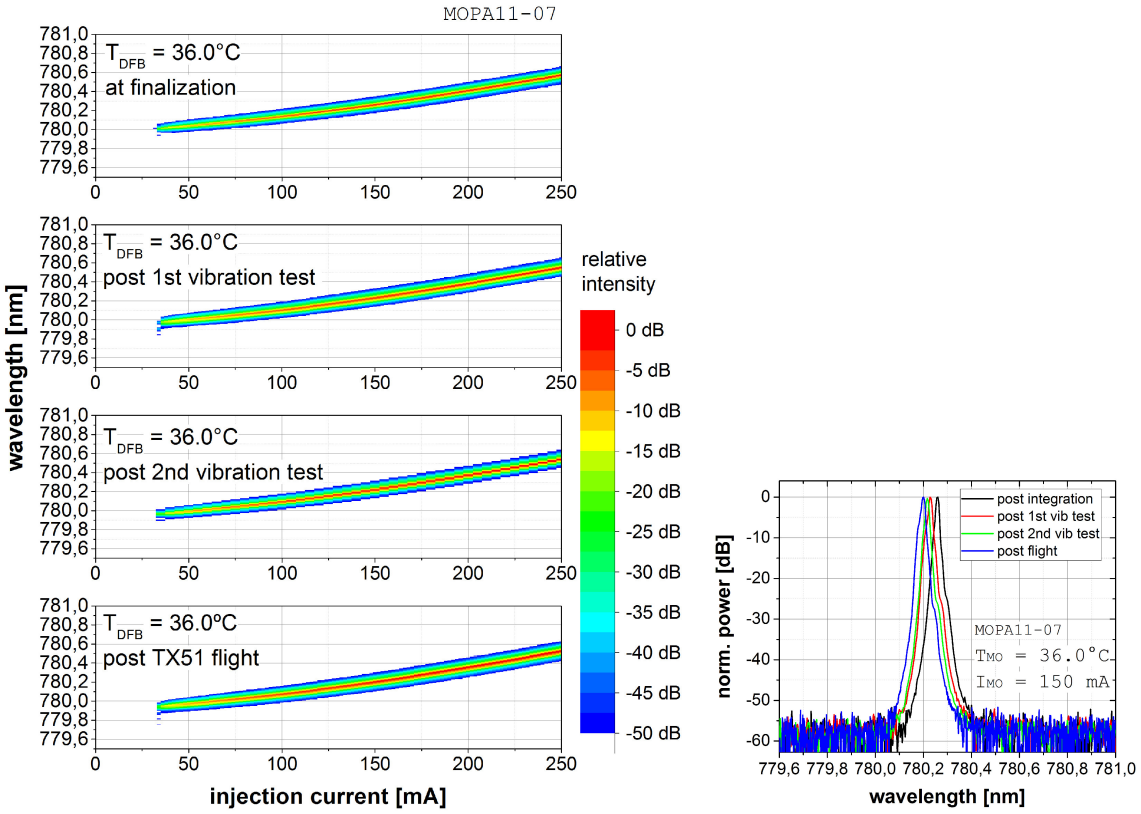

(a) (b)

Figure 7.5: Spectral performance of FOKUS diode laser module before and after vibration tests and after the flight campaign, (a) spectral map, (b) single spectrum at WP.

The optical output power is shown in figure 7.4a. In the pre-flight measurements, the output power did increase after the first vibration test. This behaviour can be explained with the burn-in process of a laser diode and was observed before, also by Spießberger in 2012 [111]. The slight lost in power after the second vibration test could be explained with different absorption behaviour of the optical isolator that had to be exchanged between the vibration tests. The free-space output power was approximately 19 mW at a WP of 150 mA and 36 °C before flight. The coupling efficiency of the free-space light into the optical fibre was roughly 60 %, estimated before system integration. The splitter between laser and spectroscopy module guides nominally 90% of the beam to the comb system. With that, 10.3 mW at the port for beat detection was expected. Post-flight, 6.8 mW could be measured at the designated WP at the optical output of the Rb reference module, featuring a fibre coupler, fibre splices, and the fibre splitter in the optical propagation path. The measured value does not fulfil the expectations. The reason probably is a combination of either: the laser diode degraded over

time, the coupling efficiency is less than the expected 60 %, there are in-fibre losses, e.g. at the splices, or the fibre splitter propagates less than 90 % of the light in this fibre output e.g. due to the mismatch of the design wavelength of the splitter. Since a reference value after integration into the FOKUS module is missing, it cannot be determined whether the power degraded in the fibre during the flight campaign.

If the laser diode degraded over time, this did not have an impact on the spectral behaviour. The FWHM and intrinsic linewidth remained constant within the measurement tolerance in all measurements, as can be seen in figure 7.4b. The FWHM linewidth was 0.996 MHz in 10 μs with a standard deviation of 75 kHz, the intrinsic linewidth, based on the white noise floor, was 64 kHz, with a standard deviation of 3 kHz. These values lie well within the expected performance as described in section 6.1.3 and the experimental requirements, given in table 2.1.

The emission spectrum remained constant at first view, as depicted in figure 7.5a. Comparing the emission wavelength at a single working point, as done in figure 7.5b, reveals that the SMSR remains constant below - 50 dB. The peak wavelength, however, seems to decrease after each mechanical stress with an overall drift of 44 pm. As described in section 6.2.2.1, the accuracy of the OSA measurement instrument is limited, with a RBW of 10 pm and an absolute accuracy in the range of $\pm$ 200 pm. The drift therefore could be explained by the inaccuracy of the OSA. Nevertheless, the current tunability remains stable at 3.2 pm/mA, noting that the spectrum seems to be shifted by an offset. The current tuning range of the laser module also remains stable above 450 pm[2]. Even if the emission spectrum drifted due to degradation of the laser diode, the drift can be compensated by the current tuning range of the laser.

The characterizations reveal that the spectral laser module behaviour remained stable all through the stress tests and the FOKUS flight campaign. Despite the uncertainty of the degradation of the power in the fibre output there is no evidence of degradation of the performance of the laser module itself. The laser module itself proofs suitable for sounding rocked based optical sensor operations and can be used for further missions.

[2]Since the minimal optical output power is defined to be 10 mW, the injection current range is 85 mA to 250 mA

7.2 MAIUS Mission

The MAIUS-1 mission was successfully launched at t_0 = 3:30:18 January 22nd 2017 CET from Kiruna Space Station. Telemetry data gathered during the mission and transmitted to the operation centre revealed that during the mission flight time it was possible to generate a BEC with Rb atoms, the first BEC produced in space [133]. Table 7.2 gives the main events of the flight.

mission time	**event**
t_0	launch at 3:30:18 January 22nd, 2017 CET
t_0 + 64 s	μg regime reached
t_0 + 421 s	μg phase ended
t_0 + 873 s	touch down

Table 7.2: Time table of FOKUS mission flight

The experiment data, stored on the on-board computer still has to be evaluated. Further details about the physics experiments therefore cannot be presented in this thesis. The remote telemetry data, however, contained the reading of the MO injection currents, the free-space photodiodes at the rear of the MOPAs, and the in-fibre photodiodes monitoring the optical power emitted by the laser modules into the fibres. To reduce the telemetry link budget the data sample rate of the housekeeping data was reduced to 0.1 Hz. The in-fibre PDs were monitored with 0.2 Hz.

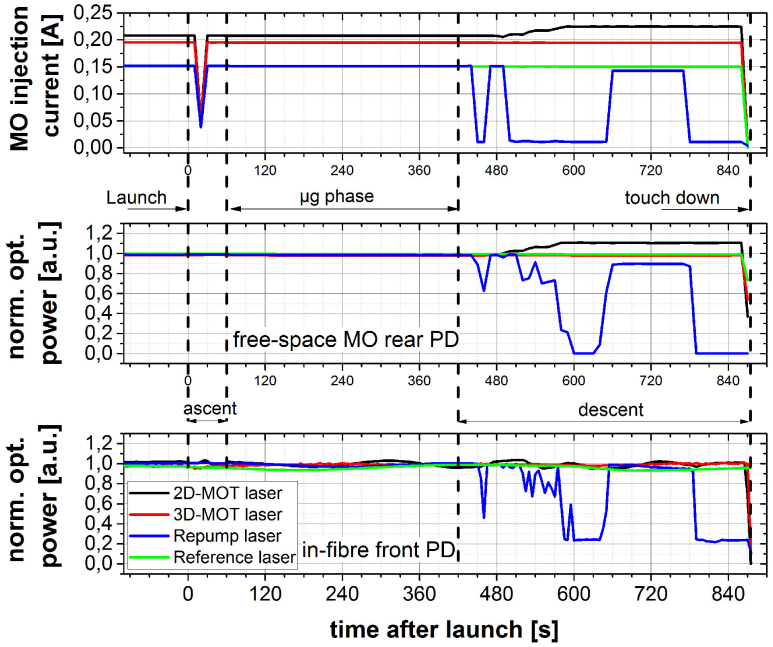

Figure 7.6: Telemetry data of MO injection current (top), the rear free-space optical power of the MO (centre), and optical power in fibre (bottom) of MAIUS laser modules

Two of the 5 MOPA modules were cold redundancy and therefore not operative during flight. Figure 7.6 shows the injection current and PD readings of the three science-MOPAs and the DFB frequency reference laser. The recorded PD voltage, corresponding to the optical power at the rear output and in the fibre, is normalized to the reading in stable operation. The values are expected to be stable because switching and preparation for the experiment is done in the switching and distribution module behind the optical power monitoring. The data reveals that the lasers have been operating before and during launch. There is an interruption of the injection current 20 s after launch. This time corresponds to the separation of the first rocket stage. Since this data point is not reflected in the output power values, it might be caused by a reading or transmission error. The injection current and optical power remains stable during the entire μg phase. After the μg phase, during descent, the current driver of the 2D-MOT laser module increased the current and with that increasing the optical power of the MO, as shown in black in the top and middle graph in figure 7.6. As expected, the MO power variances were not propagated through the amplifier of the 2D-MOT laser. Also after the μg phase, the current of the re-pump laser shows multiple interruptions, resulting in power fluctuations both for the MO and in the fibre. These interruptions were most likely cause by a lose SMA cable connection of the re-pumpers MO injection current. It can be seen, that for an injection current close to zero the MO output power drops to zero and the amplified in-fibre power is reduced to ASE emission. The 3D-MOT laser and the reference laser remained stable during the entire flight.

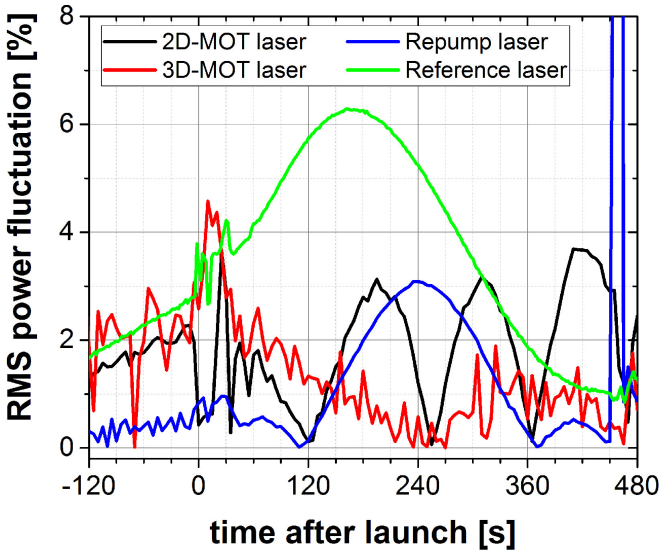

Figure 7.7: RMS power fluctuations of the in-fibre power readings of the laser modules

Although the power of all modules remained stable during ascent and μg phase, there are deviations in power when comparing the in-fibre data with the free-space data. The RMS fluctuations in figure 7.7 reveal that the deviation of the mean value of the MOPA modules is not larger than 5 %. There are short-term ripples and long-term drifts observable. The ascent phase after launch until $t_0 + 60$ s is clearly visible by fluc-

tuation peaks in all data sets. However, during the mission sine-like fluctuations, lasting several minutes, dominate. This long-term drift is very clearly visible for the reference laser with up to 6.5 %, although, due to the smaller optical power in the fibre thermal dependencies might show a stronger effect. Since this drift can only be observed in the fibre path reading, but not in the free-space data at the rear port, the drifts are most likely introduced by the fibre components of the laser system. They are probably caused by temperature differences in the laser system and different temperature dependencies of the components in the optical path, such as the fibres, fibre couplers, and the in-fibre PDs themselves, and not by the amplifier and collimation optics. This assumption also is supported by the data of the reference laser that does not host an amplifier.

However, all interruptions of optical power can be traced back to fluctuations of the injection current. It also has to be stated that all lasers performed stable with no interruption from launch and through the entire μg phase when the experiments took place. Power fluctuations in fibre were rather small and not caused by the laser modules themselves.

After recovery of the payload and minor repairs in the optical distribution system, the experiment apparatus still could be operated and was able to create a BEC, underlining the robust design of the entire MAIUS experiment apparatus. As shown by these preliminary results of the MAIUS mission the MOPA modules proved their suitability for quantum optical experiments in space.

Chapter 8

Summary and Outlook

The main objective in this work was the development and production of high-power, narrow-linewidth semiconductor laser modules with improved frequency stabilization capabilities for applications on board of sounding rockets. This chapter gives a brief summary of the results achieved in this work and identifies some aspects that could be improved in future design. Future prospects of hybrid integrated laser modules for space missions are named in the outlook section.

8.1 Summary

In this thesis a semiconductor based laser module for high precision mobile quantum optical sensors was developed that is capable for operation in harsh environments. To do so, a hybrid micro-integration approach was chosen, allowing the integration of active semiconductor devices as well as passive optical components in order to enhance the spectral performance of the laser modules and form the beam output. DFB laser diodes, optimized for narrow linewidth emission at the demanded emission frequencies, as well as TPA diodes with sufficient gain at the demanded emission frequencies were chosen to provide the spectral stability and sufficient optical power as required for quantum optical sensor applications. Optical feedback on the DFB diodes is prevented by the integration of a miniaturised optical isolator, maintaining the spectral performance of the MO. The optical output beam was collimated with miniaturized lenses in order to meet beam parameters for fibre coupling.

The laser diodes and micro-optics are integrated on a micro-optical bench based on a 4 mm thick AlN ceramic with a footprint as small as 25 mm × 80 mm. The ceramic base plate offers a high mechanical stability and good thermal conduction. The latter is important for thermal stabilization of the laser diodes in order to stabilize the laser's emission frequency. The thermal stabilization of the laser module is supported by thermal sensors placed close to the laser diodes. These temperature sensors allow for a more explicit regulation of the temperature of the laser diodes since the thermal environment of the diode can be measured more precisely. The MIOB also offers an electrical interface for coaxial cable connectors and a RF interface for modulation of the injection current of the diodes in short distance to the semiconductor. With that

the frequency stabilization capabilities of the laser module are improved. The laser module omits movable parts. The micro-optics are adhesively attached to the MIOB after active alignment. This decreases the probability of misalignment and increases the mechanical stability of the laser module.

Methods and procedures for producing a small series of laser modules were established, including pre-integration qualification of the components, burn-in of laser diode and amplifier chips, and active alignment procedures for the laser module integration. With help of the qualification of the diodes only the ones with the best performance were selected for integration, increasing the yield of laser module production. A statistical analysis of the pre-integration characterization of the semiconductor chips revealed a yield of less than 50 %, both for DFB diodes and for TPA amplifiers. The failure causes, though, were different for both kinds of chips. For DFB diode lasers a poor spectral performance, such as instability or mismatch of the wavelength, dominated. Amplifiers most often failed the qualification due to poor facet quality. Because of small production numbers, the semiconductor processing and coating processes at the FBH are not fully automated and can be seen as experimental. The processes therefore cannot be fully optimized to increase the yield. The resulting yield of less than 50 % therefore was expected and underlines the necessity of a qualification process prior to integration of the semiconductor diodes into a complex laser system.

The laser modules were characterized electro-optically, showing an optical output power of > 1 W and an electrical-to-optical efficiency up to 29%. The optical behaviour of DFB diode lasers depends on the resonator length of the DFB laser. Lasers with a resonator length of 1.5 mm provide a higher efficiency and larger current tuning. 3 mm long lasers allow for a larger current range, and provide a much narrower linewidth. The overall single-mode spectral tuning range of 1.8 nm (corresponding to 886 GHz) can be reached, when tuning both the injection current and the operating temperature. The linewidth improves for longer chips: the 3 mm DFB chip provides an intrinsic linewidth less than 50 kHz and a short-term FWHM linewidth of less than 400 kHz (10 μs) for an optical output power of the DFB of 120 mA, whereas a 1.5 mm DFB chip only provides an intrinsic linewidth of in the range of 100 kHz and a short-term FWHM linewidth in the range of 1 MHz (10 μs) for a the same optical output power.

The effect of environmental stress on the laser modules was tested as well. Random vibration up to 29 g_{RMS} and shock tests with 1500 g did not influence the performance of the laser modules. The thermal cycling, however, caused degradation in the amplifier saturation, caused by misaligned in-coupling into the amplifier. Since the optical power of the MO is significantly larger than the optical power required to saturate the amplifier, no changes in the performance at WP operation could be observed after the thermal stress tests. For long-term missions, however, provisions, such as temperature control and thermal shielding, should be implemented for storage and operation mode to guarantee stable performance over a long time of the mission.

A micro-integrated DFB laser on a MIOB was employed in the FOKUS sounding rocked experiment where it was frequency-stabilized to a Rb transition in a Doppler-free spectroscopy setup. The optical beam then was compared to a CSAC, operating in the microwave range. This experiment served as technology demonstrator for an optical atomic clock based LPI experiment in space, aiming to prove or disprove the EEP.

The test was successful, all components operated as expected, although the sensitivity of the measurement was limited by long-term drifts of the reference frequency. The laser modules were still functional after the mission with comparable performance. In January 2017 the MAIUS apparatus, hosting five MOPA modules and one DFB module, was launched and generated the first BEC in space. The apparatus was, after minor repairs, fully operational after recovery. The laser modules were not harmed and operated as expected during the whole mission. The data collected in this mission still has to be analysed.

The successful execution of the FOKUS and MAIUS missions proves not only that it is possible to miniaturize laser sources with high precision frequency emission, but also that laser modules developed in this thesis fulfil all requirements demanded by quantum optical high precision sensor experiments in micro-gravity environments. To our current knowledge, the laser modules flown in MAIUS are the smallest and lightest laser modules providing more than 1 W optical output power ever operated in space.

Besides the sounding rocket experiments, laser modules developed in this thesis are also used in drop tower experiments as described by Kulas in [134]. These laser modules are not only suitable for spaceborne applications but serve also in rough environments on Earth and can save space in ordinary laboratories as well.

8.2 Outlook

The next logical step towards a laser module for field applications is the integration of a fibre coupler and a protective housing in order to provide a plug and play system for the users of quantum optical sensors.

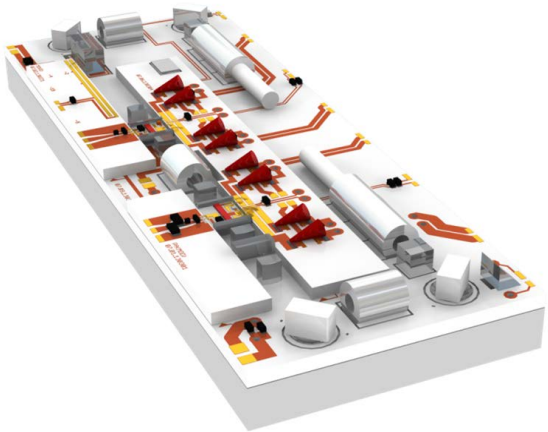

Figure 8.1: A laser module of the next generation, hosting a fibre coupling. Beam adjustment is done by mirrors on spherical mounts, the fibre ferrule contains a collimating lens.

The housing would prevent contamination of the optics by dirt particles. Furthermore, a hermetic housing would contain an atmosphere around the semiconductor chips even in a vacuum operation environment. This would enable the use of laser

modules in long-term operation in space such as on satellites. As mentioned before, an ECDL setup as MO would increase the frequency stability of the emission. However, existing ECDL modules provide an output power not larger than 100 mW [130] and have to be amplified in a separate module.

The MIOB of the next generation of laser modules is depicted in figure 8.1. It can be equipped modularly with different laser types, allowing for combinations such as ECDL with amplifier, combining a very narrow linewidth with high output power, or two laser chips pointing in opposite directions. The fibre couple concept makes use of a collimated fibre ferrule and mirrors on polished spherical joints. Since the MIOB provides fibre coupling for the front and for the rear output, besides the classical front and rear output configuration, there also is the option of two fibre coupled master oscillators on one module, minimizing space and weight in case the optical power requirements allow the absence of an amplifier.

The next generation of laser modules also considers aspects that were learned during the production of the laser modules described in this work. The new MIOB provides a wider channel for optics integration. The channel in the current version has a width of 2.2 mm. A width of > 4 mm is recommended for various reasons. First, the submount can be wider, allowing for additional bond-pads that omit multiple wire-bonding on the semiconductor chips during pre-characterization and integration. And second, adhesive, applied to hold the SACs during integration, will not flow in the space between the SAC lens and the MIOB side wall because the gap will be too large. Lateral pulling of the SAC, and with that displacement, during UV curing will be avoided. The beam propagation properties, adjusted before the curing of the adhesive, can be maintained.

With these changes and additional features, the successful laser module, described in this thesis, will be improved and the range of applications can be increased.

Appendix A

List of diodes used in this work

The following table A.1 identifies the laser diodes and amplifier chips integrated in the laser modules described in this thesis. Further, the appearance of measurement results obtained with these laser modules is given. The diode ID, MO ID, and PA ID consist of the number of the wafers test field (TF), the row in the test field in two digits (RR), and the diode number of the row in two digits (DD). They are arranged as TF-RR-DD.

module ID	wafer MO	MO ID	wafer PA	PA ID	appearance in figure
MOPA11-01	C1152-6-1	02-09-03	C2358-3	06-03-xx	5.2
MOPA11-07	C2212-6-1	00-08-21	no PA		7.4,7.5
MOPA11-09	C1152-6-1	02-09-04	C2358-3	08-09-21	6.2,6.10
MOPA11-10	C2212-6-1	01-01&02-10	C2358-3	08-07-14	6.3,6.4,6.6,6.7
MOPA11-13	C1152-6-1	02-09-07	C2358-3	08-07-15	6.8,6.9,
MOPA12-16	C2212-6-1	00-09-16	C2358-3	08-07-13	6.1
MOPA12-18	C2610-6-1	01-04-10	C2850-3	01-01-05	4.13,4.15

Table A.1: List of laser modules used in this work. The diode number of the PA in MOPA11-01 is unknown.

The following table A.2 gives the remaining diodes of which measurement results are presented in this thesis, but which are not integrated into a laser module.

diode type	diode wafer	diode ID	appearance in figure
DFB	C2212-6-1	01-01&02-17	5.1a
TPA	C2358-3	08-02-05	5.1b

Table A.2: List of single diodes used in this work

Appendix B

Schematics of MIOB PCBs

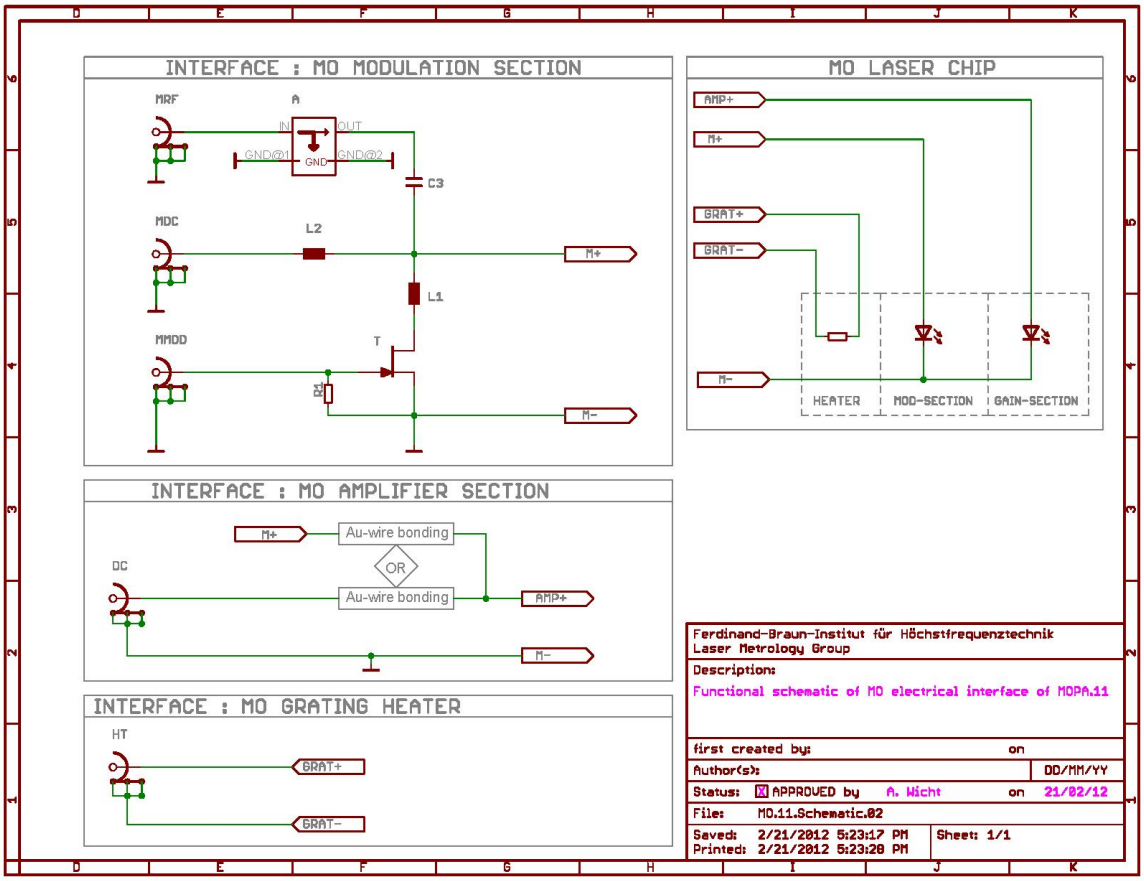

Figure B.1: Functional schematic of MO electrical interface

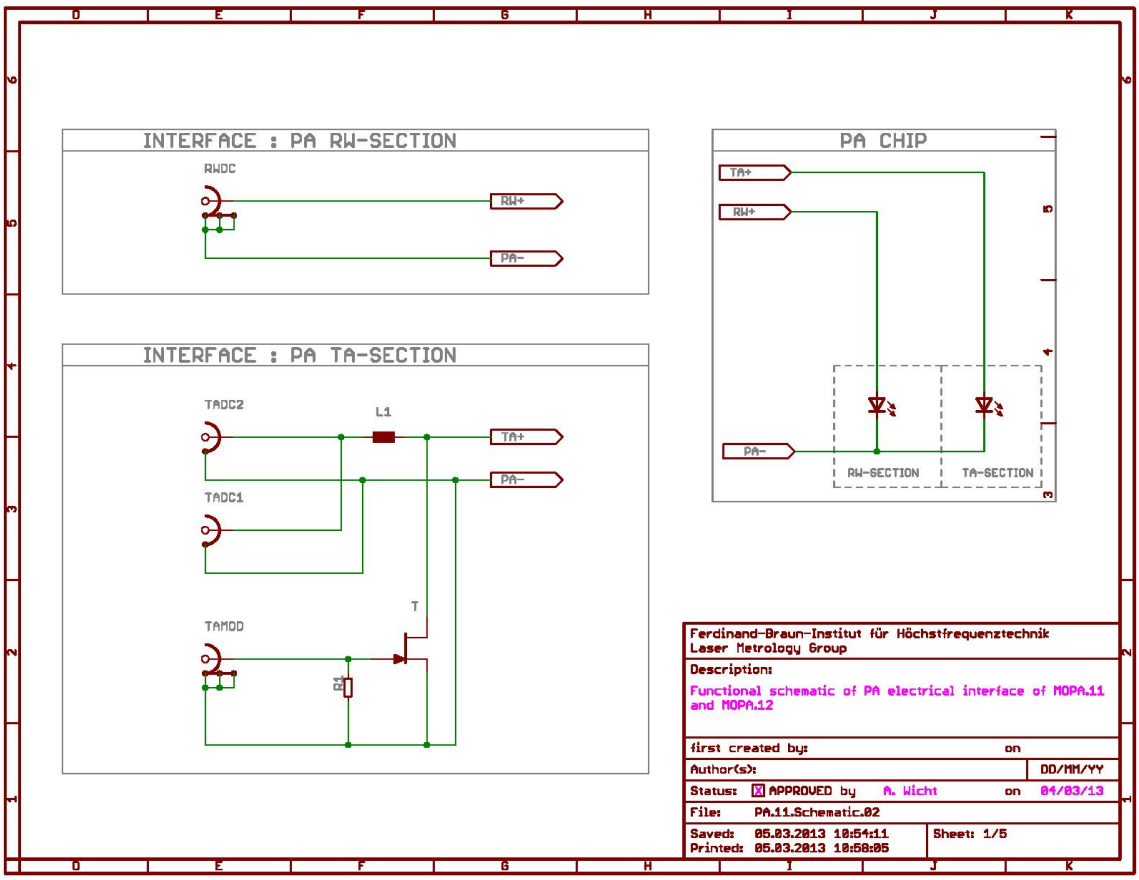

Figure B.2: Functional schematic of PA electrical interface

The values and description of the parts named in figures B.1 and B.2 are listed in table B.1

part	value	description
		MO interface PCB
A	10 dB	attenuator of MRF signal
C3	1 nF	bias-tee MRF
L1	2.2 nH	
L2	2.75 μH	bias-tee MRF
T	n.a.	JFET transistor
R1	100 Ω	pull-down resistor for transistor gate
		PA interface PCB
L1	1.35 μH	filter
T	n.a.	JFET transistor
R1	100 Ω	pull-down resistor for transistor gate
		temperature sensor interface PCB
C1	100 nH	filter, in parallel to C2
C2	1 nH	filter, in parallel to C1
NTC	10 kΩ	temperature sensor

Table B.1: Components list of the electrical interface of the MIOB

Appendix C

Examples of Facet Inspection Ratings

This appendix gives an overview of facet issues, as rated in chapter 5.

C.1 Qualified Facets

C.1.1 Blameless Facets

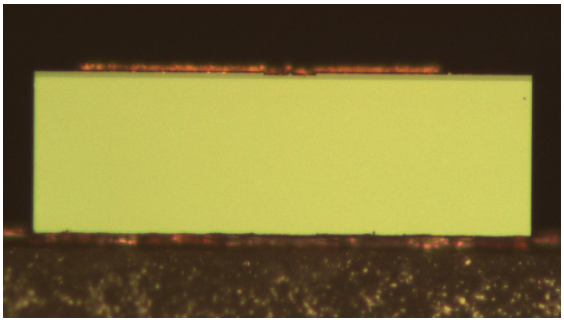

(a) passed DFB front facet

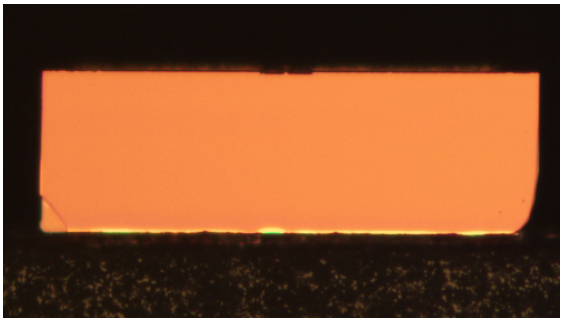

(b) passed DFB rear facet

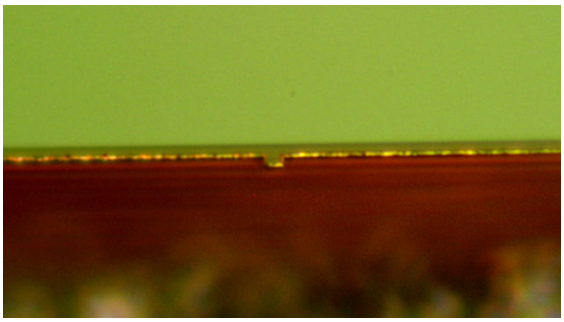

(c) passed TPA rear facet, RW

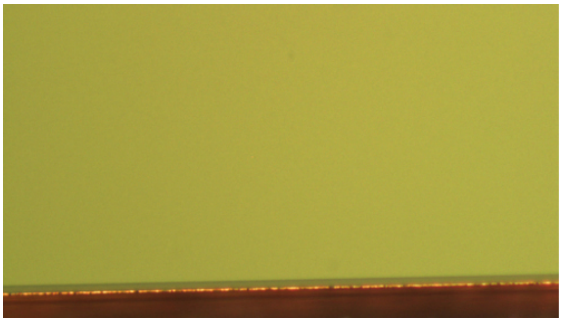

(d) passed TPA front facet

Figure C.1: Facets of DFB diode C2212-6-1: 00-09-22 (a,b) and TPA diode C2358-3: 08-02-13 (c,d)

C.1.2 Qualified Facets with Non-critical Defects

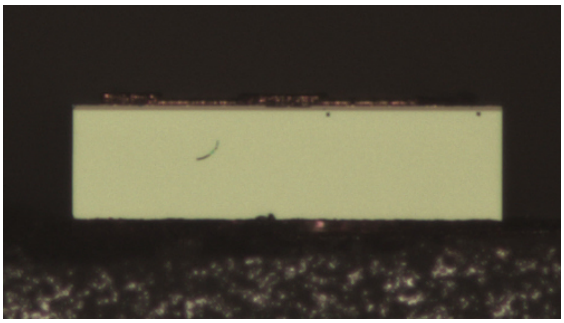

(a) particle close to active region

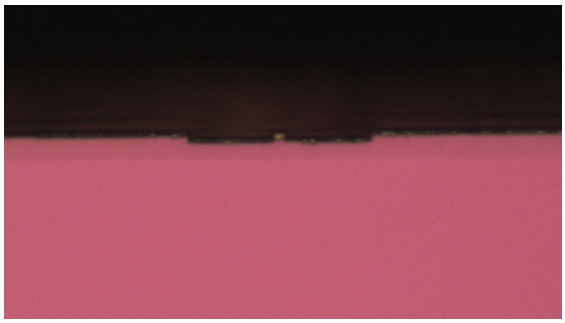

(b) shine above the ridge

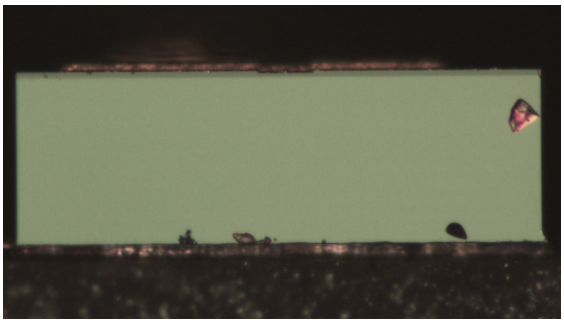

(c) particles at bulk

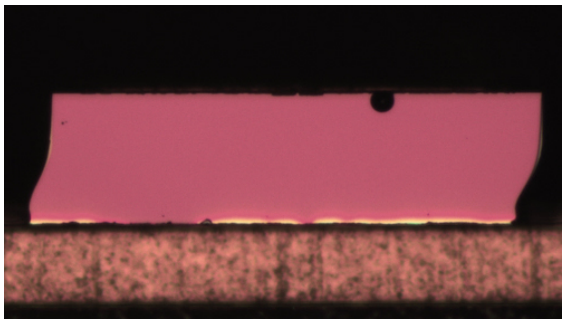

(d) blopp

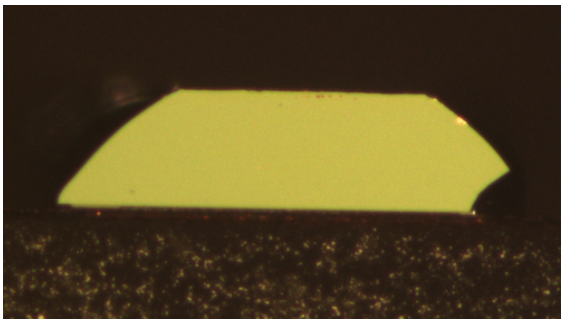

(e) bulk demolition, p-down

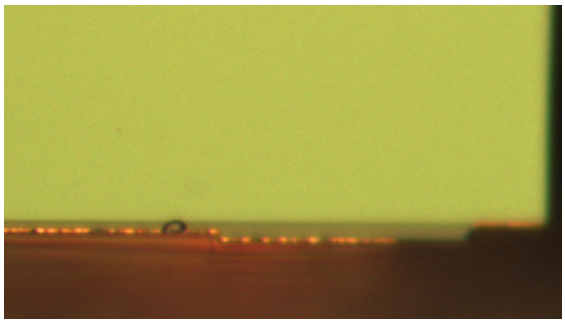

(f) particle outside active area, rear facet

Figure C.2: Questionable facets of DFB diode C2610-6-2: 02-0304-21 (a), (b), 01-04-13 (d) and C2212-6-1: 00-09-16 (c), as well as TPA diodes C2358-3: 08-06-08 (e) and 08-09-11 (f)

C.2 Facet Defects

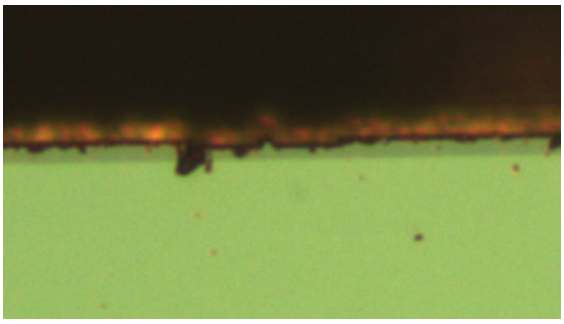

(a) defects at active area front facet

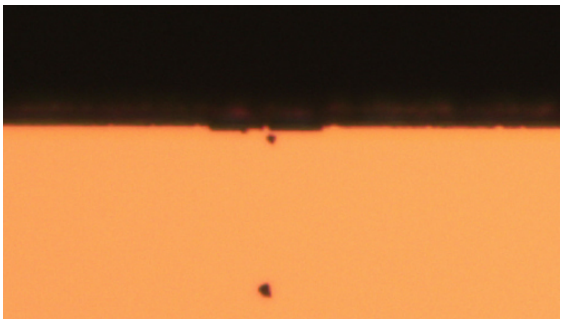

(b) defects at active area rear facet

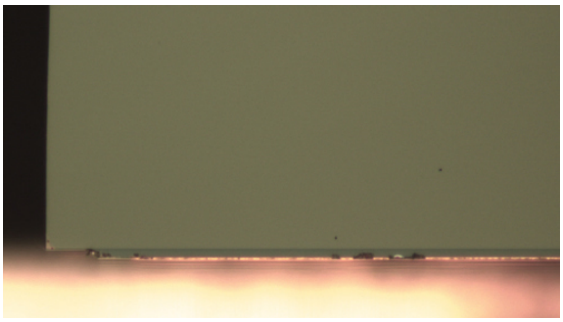

(c) particles at TA active area, p-down

Figure C.3: facets failed in inspection because of active area defects. DFBs: C2212-6-1: 00-07-07 (a) and 00-10-05 (b), TPA C2358-3: 01-01-03 (c)

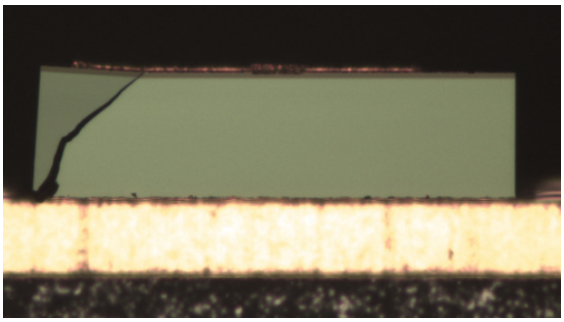

(a) lose bulk material

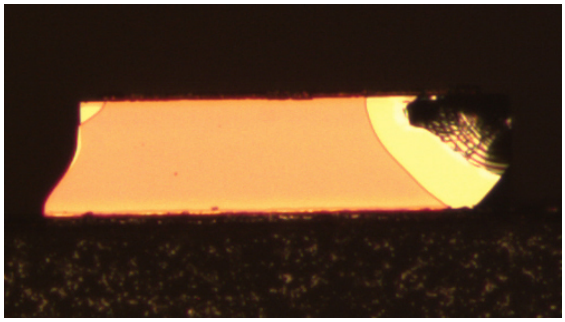

(b) flaked off coating at rear facet

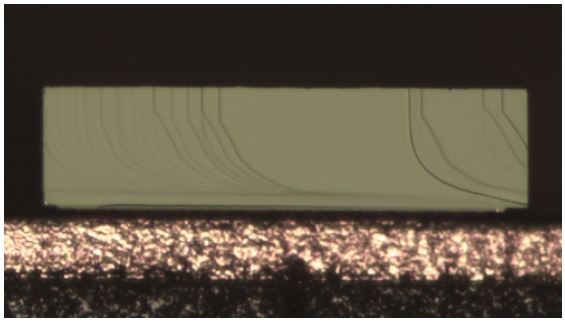

(c) terraces at front facet

Figure C.4: facets failed in inspection because of bulk defects. DFBs: C2610-6-2 01-04-17 (a) and 01-01-15 (b); TPA: C2358-3 08-07-16 (c)

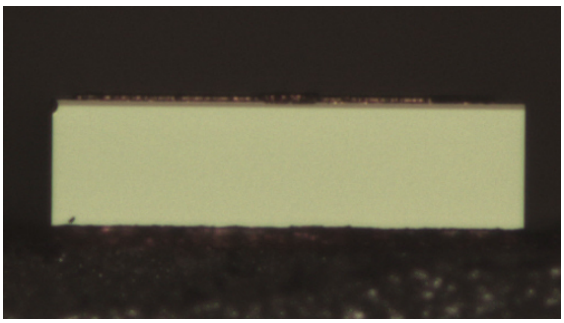

(a) before burn-in

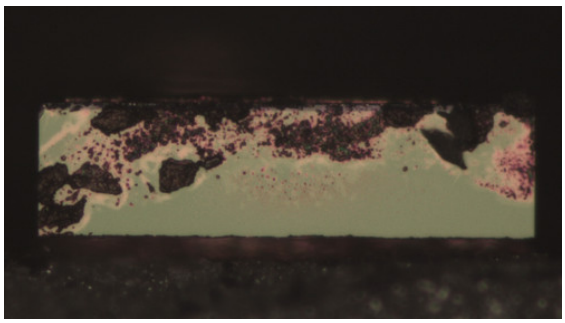

(b) after burn-in

Figure C.5: Facets of diode C2610-6-2: 02-0304-10, destroyed front facet after qualification process

Appendix D

Terms and Acronyms

2D-MOT two-dimensional magneto-optical trap 16

3D-MOT three-dimensional magneto-optical trap 16

Al aluminium 35

AlN aluminium nitride 7

AOM acousto-optic modulators 16

AR anti-reflection 28
facet coating option

ASE amplified spontaneous emission 29

Au gold 79

AuSn gold tin 39

BEC Bose-Einstein condensate 3

BPSK binary phase-shift keying 2

CCD charge-coupled device 14

CCP conductively cooled package 43

CEO carrier-envelope-offset 8

COD catastrophic optical damage 30

CSAC chip scale atomic clock 6

CTE coefficient of thermal expansion 91

Cu copper 38

CuW copper-tungsten 71

CW continuous wave 16

DC direct current 41

DFB distributed feedback laser diode 7

DLR "Deutsche Zentrum für Luft- und Raumfahrt e. V." 129

DLR-MORABA "Mobile Raketenbasis des Deutschen Zentrums für Luft- und Raumfahrt" 8

DOF degree of freedom 36

DUT device under test 61

ECDL extended cavity diode laser laser module configuration 27

EDM electrical discharge machining 43

EEP Einstein equivalence principle 6

EO electro-optical 66

Er erbium 8

ESA European Space Agency 2

ESCC European Space Components Coordination 90

FAC fast axis collimator 37

FBH "Ferdinand-Braun-Institut, Leibniz-Institut für Höchstfrequenztechnik" 35

FMS frequency modulation spectroscopy 7

FSR free spectral range 27

FOKUS "Faserlaserbasierter Optischer Kammgenerator unter Schwerelosigkeit" sounding rocked mission 5

FSR free spectral range 27

FWHM full width at half maximum 10

GaAs gallium arsenide 21

GaN gallium nitride 21

GSE ground support equipment 9

HR high reflection 22

Ni nickel . . . 43

OLO optical local oscillator . . . 86

OSA optical spectrum analyser . . . 49

PA optical power amplifier . . . 34

PBS polarizing beam splitter . . . 7

PCB printed circuit board . . . 39

PD photodiode . . . 7

PER polarization extinction ratio . . . 77

PSD power spectral density . . . 85

QAM quadrature amplitude modulation . . . 2

QUANTUS "Quantengase unter Schwerelosigkeit" . . . 11
project association featuring drop tower experiments

Rb rubidium . . . 6

RBW resolution bandwidth . . . 65

RF radio frequency . . . 13
typically in the range of 3 kHz to 300 GHz

RW ridge waveguide . . . 30

RWDC DC port for the RW pre-amplifier section . . . 42
RW interface on MIOB

RMS root mean square . . . 96

SAC slow axis collimator . . . 37

SDH self-delayed heterodyne . . . 86

SHG second harmonic generation . . . 6
frequency doubling technique

SMA SubMiniature version A . . . 43
cable interface type

SMSR side mode suppression ratio . . . 65

SNR signal to noise ratio . . . 14

SOA semiconductor optical amplifier . . . 28

TA tapered section of an optical amplifier 35

TADC DC port for the tapered section 42
PA interface on MIOB

TAMOD modulation port for the PA gain section modulation 42
PA interface on MIOB

TEXUS "Technologische Experimente unter Schwerelosigkeit" 8
rocket mission program of "Deutsche Zentrum für Luft- und Raumfahrt e. V." (DLR)

TPA tapered power amplifier 72

TRL technology readiness level 99

UHH "Universität Hamburg", Institut für Laserphysik 45

UV ultra violet 48
radiation with wavelengths in the range of 100 nm –380 nm

VSB-30 "Veículo de Sondagem Booster – 30" (engl.: Booster Sounding Vehicle) 8
Brazilian sounding rocket, used in FOKUS and MAIUS

WP working point 10
parameter set a diode laser operates with the aimed characteristics

Nomenclature

α	linewidth enhancement factor, also: Henry factor
α_m	cavity losses
$\bar{y}_n$	n^{th} average normalized frequency deviation from nominal frequency over a finite time interval
β_i	sensitivity to potential violation of the LPI
β_{sp}	spontaneous emission factor
$\Delta\nu_{sp}$	linewidth enhancement due to spontaneous emission
$\Delta\omega$	the difference of the angular frequency of two laser beams
ΔU	varying gravitational field
ϵ	conversion efficiency of electrical power into optical power.
η_i	injection efficiency, fraction of I that generates carriers in the active region
η	conversion efficiency, $\eta = P_{in}/P_o$
η_d	differential quantum efficiency, defined by the number of photons emitted per injected electron
Γ	confinement factor, ratio between the volume of the active area and the volume of the optical mode
ν	the frequency of the photon
ρ_{th}	thermal conductivity
σ^2	Allan variance
τ	time interval, carrier lifetime
τ_m	equivalent lifetime of photon in resonator before leaving through mirror
τ_p	average lifetime of a photon in a resonator
τ_{st}	lifetime of stimulated carriers

$\varphi(t)$ the phase of the beat note signal

A_{LD} footprint of the laser diode

c speed of light, $c = 299\,792\,458\,m/s$

E_m excited energy state of an electron

E_n ground energy state of an electron

E_{mode} stored optical energy in the cavity

f frequency

f_m modulation frequency

G gravitational constant, $G = 6.674 \times 10^{-4}\ m^3/kgs^2$

g gain

g_m material gain coefficient

g_{amp} amplifier gain coefficient

g_{thr} gain above threshold

g_{usat} unsaturated small signal gain

h the Planck constant, $h = 6.626\,070 \times 10^{-34}\,Js$

$h\nu$ energy per photon

h_{rocket} altitude of the experiment above ground

H_{vert} vertical height of the heat sink

I injection current

I_m difference of injection current, induced by modulation

I_s static injection current, without modulation

I_{thr} threshold current

K spontaneous emission enhancement factor, also: Petermann factor

L resonator length

L_m change of resonator length, induced by modulation

M_{Earth} mass of Earth, $M = 5.974 \times 10^{24}\,kg$

N number of carriers

n_c carrier density

$n_{r,m}$ change in the refraction index in the resonator due to carrier modulation

n_r refraction index

P_d dissipation power

P_o optical output power

$P_{i,sat}$ saturation input power

$P_{o,sat}$ saturation output power

q elementary electrical charge, $q = 1.602\,177 \times 10^{-19}$ C

R_d differential electrical resistance of the laser diode

R_l leakage rate

R_s serial resistance of laser diode

r_{Earth} radius of Earth, $r = 6378\,km$

R_i injection rate of electrons

R_{nr} non-radiative recombination rate

R_{rec} electron recombination rate

R_{sp} spontaneous recombination rate

R_{st} stimulated recombination rate

R_{th} thermal resistance of laser diode

S number of photons

T temperature

T_0 characteristic temperature, given by the material system

t_0 time of rocket launch

T_m temperature difference, induced by modulation

T_s static temperature, without modulation

T_{WP} external applied temperature, e.g. working point temperature

U_s static bias voltage

V volume

V_d diode voltage, quasi-Fermi level separation

v_g velocity of a photon in a gain medium

V_s series voltage over laser diode, current-independent

V_{beat} beat signal in heterodyne measurement, voltage of the photo diode

y fractional frequency

Z_t thermal impedance of the laser diode

Appendix E

Publications

The following scientific publications have been prepared in connection with this thesis:

E.1 Print

Compact narrow linewidth diode laser modules for precision quantum optics experiments on board of sounding rockets
A. Kohfeldt, Ch. Kürbis, E. Luvsandamdin, M. Schiemangk, A. Wicht, A. Peters, G. Erbert, G. Tränkle
Proc. SPIE, Quantum Optics, volume 9900, no. 99001G, 2016.

Miniaturized lab system for cold atom experiments in microgravity
S. Kulas, Ch. Vogt, A. Resch, J. Hartwig, S. Ganske, J. Matthias, D. Schlippert, T. Wendrich, W. Ertmer, E.M. Rasel, M. Damjanic, P. Weßels, **A. Kohfeldt**, E. Luvsandamdin, M. Schiemangk, Ch. Grzeschik, M. Krutzik, A. Wicht, A. Peters, S. Herrmann, C. Lämmerzahl
Microgravity Science and Technology, volume 29, no. 1:37, 2017.

A compact and robust diode laser system for atom interferometry on a sounding rocket
V. Schkolnik, O. Hellmig, A. Wenzlawski, J. Grosse, **A. Kohfeldt**, K. Döringshoff, A. Wicht, P. Windpassinger, K. Sengstock, C. Braxmaier, M. Krutzik, A. Peters
Applied Physics B, volume 122, no. 8:217, 2016.

Space-born Frequency Comb Metrology
M. Lezius, T. Wilken, Ch. Deutsch, M. Giunta, O. Mandel, A. Thaller, V. Schkolnik, M. Schiemangk, A. Dinkelaker, M. Krutzik, **A. Kohfeldt**, A. Wicht, A. Peters, O. Hellmig, H. Duncker, K. Sengstock, P. Windpassinger, K. Lampmann, T. Hülsing, T. Hänsch, R. Holzwarth
Optica, volume 3, no. 12:1381, 2016.

High power, micro-integrated diode laser modules at 767 and 780 nm for portable quantum gas experiments
M. Schiemangk, K. Lampmann, A. Dinkelaker, **A. Kohfeldt**, M. Krutzik, Ch. Kürbis A. Sahm, St. Spießberger, A. Wicht, G. Erbert, G. Tränkle, A Peters
Applied Optics, volume 54, no. 17:5332, 2015.

High power, narrow linewidth, micro-integrated semiconductor laser modules designed for quantum sensors in space
A. Kohfeldt, A. Bawamia, Ch. Kürbis, E. Luvsandamdin, M. Schiemangk, A. Wicht, G. Erbert, A. Peters, G. Tränkle
CLEO: 2014 OSA Technical Digest, paper JTh2A.36, 2014.

A frequency comb and precision spectroscopy experiment in space
T. Wilken, M. Lezius, T. W. Hänsch, **A. Kohfeldt**, A. Wicht, V. Schkolnik, M. Krutzik, H. Duncker, O. Hellmig, P. Windpassinger, K. Sengstock, A. Peters, R. Holzwarth
CLEO: 2013, OSA Technical Digest, paper AF2H.5, 2013.

Micro-integrated, high power, narrow linewidth master oscillator power amplifier for precision quantum optics experiments in space
A. Kohfeldt, M. Schiemangk, St. Spießberger, A. Wicht, A. Peters, G. Erbert, G. Tränkle
CLEO 2012: OSA Technical Digest, paper JW3C.2, 2012.

E.2 Oral

This following list only contains presentations, where the author of this thesis was first author:

Micro-integrated, high power, narrow linewidth master oscillator power amplifier for precision quantum optics experiments in space
Conference on Lasers and Electro-Optics (CLEO): Science and Innovations 2012, San Jose (USA), 6-11 May 2012.

Micro-integrated diode laser modules for high precision quantum sensors in space
Deutsche Physikalische Gesellschaft (DPG), AMOP Annual Meeting, Heidelberg (Germany), 23-27 March 2015.

Micro-integrated semiconductor laser modules designed for quantum sensors in space
Laser Optics Berlin, Berlin (Germany), 18-20 March 2014.

Lichtquellen für quantenoptische Sensoren im Weltraum
Kolloquium des FBH, Berlin (Germany), 6 June 2014.

E.3 Poster

This following list only contains presentations, where the author of this thesis was first author:

Compact narrow linewidth diode laser modules for precision quantum optics experiments on board of sounding rockets
SPIE Photonics Europe, Brussels (Belgia), 4-7 April 2016.

Micro-Integrated, Narrow Linewidth Master Oscillator Power Amplifier Designed for Quantum Sensors in Space
Conference on Lasers and Electro-Optics/ European Quantum Electronics Conference (CLEO Europe), Munich (Germany), 21-25 June 2015.

DFB-Master-Oscillator-Power-Amplifier system for high precision optical sensors
Deutsche Physikalische Gesellschaft (DPG), SKM Annual Meeting, Berlin (Germany), 15-20 March 2015.

High power, very narrow linewidth, micro-integrated diode laser modules designed for quantum sensors in space
International Conference on Atomic Physics (ICAP), Washington DC (USA), 3-8 August 2014.

High power, narrow linewidth micro-integrated semiconductor laser modules designed for quantum sensors in space
Conference on Lasers and Electro-Optics (CLEO), San Jose (USA), 8-13 June 2014.

Dynamic properties of diode laser modules for space application
WIAS Workshop: Nonlinear Dynamics in Semiconductor Lasers, Berlin (Germany), 12-15 May 2014.

Micro-integrated semiconductor laser modules for precision quantum sensors in space
Deutsche Physikalische Gesellschaft (DPG), AMOP Annual Meeting, Berlin (Germany), 17-21 March 2014.

Micro-integrated, high power, narrow linewidth diode lasers for precision quantum optics experiments in space
European Frequency and Time Forum (EFTF), Gothenburg (Sweden), 23-27 April 2012.

Bibliography

[1] Maiman, T.H., "Stimulated Optical Radiation in Ruby", *Nature*, volume 187, no. 4736: 493, 1960.

[2] Spetz, J., "Physicians and Physicists: The Interdisciplinary Introduction of the Laser to Medicine", in N. Rosenberg, A.C. Gelijns, and H. Dawkins (editors), "Sources of Medical Technology: Universities and Industry", chapter 3, pp. 41–66, Institute of Medicine (US) Committee on Technological Innovation in Medicine, Washington, D.C., 5th edition, 1995.

[3] Steen, W., Watkins, K., and Mazumder, J., *Laser Material Processing*, Springer London, London, 4 edition, 2010.

[4] Gowar, J., *Optical Communication Systems*, Prentice Hall, 2nd edition, 1993.

[5] Lambert, S.G. and Casey, W.L., *Laser Communications in Space*, Artech House, 1995.

[6] Donges, A. and Noll, R., *Laser Measurement Technology: Fundamentals and Applications*, Springer, Heidelberg, 1st edition, 2014.

[7] Browell, E., Ismail, S., McCormick, M., et al., "Spaceborne lidar system for measurements of atmospheric water vapor and aerosols", in "Earth Observing Systems Conference", pp. AIAA–85–2091, 1985.

[8] Winker, D.M., Couch, R.H., and McCormick, M.P., "An overview of LITE: NASA's Lidar In-space Technology Experiment", *Proceedings of the IEEE*, volume 84, no. 2: 164, 1996.

[9] ESA, "Earth Explorers – Technical & Programmatic Annex to EarthCARE mission", *Technical Report*, ESA, 2004.

[10] Chan, V.W.S., "Optical Satellite Networks", *J. Lightwave Technol.*, volume 21, no. 11: 2811, 2003.

[11] Sodnik, Z., Furch, B., and Lutz, H., "Free-space laser communication activities in Europe: SILEX and beyond", in "Conference Proceedings - Lasers and Electro-Optics Society Annual Meeting-LEOS", pp. 78–79, 2006.

[12] Gaudel, I., "Operational Use of SILEX Optical Laser Link between SPOT4 and ARTEMIS Satellites", in "Space OPS 2004 Conference", pp. 1–12, 2004.

[13] Norimatsu, S. and Iwashita, K., "Linewidth requirements for optical synchronous detection systems with nonnegligible loop delay time", *Journal of Lightwave Technology*, volume 10, no. 3: 341, 1992.

[14] Ip, E. and Kahn, J.M., "Carrier Synchronization for 3- and 4-bit-per-Symbol Optical Transmission", *Journal of Lightwave Technology*, volume 23, no. 12: 4110, 2005.

[15] Steck, D.A., "Rubidium 87 D Line Data", *Technical Report*, Oregon Center for Optics and Department of Physics, Univers ity of Oregon, Oregon, 2010.

[16] Tiecke, T.G., "Properties of Potassium", *Technical Report v1.02*, Harvard University, 2011.

[17] Kasevich, M. and Chu, S., "Measurement of the gravitational acceleration of an atom with a light-pulse atom interferometer", *Applied Physics B*, volume 54, no. 5: 321, 1992.

[18] Planck, M., "Zur Theorie des Gesetzes der Energieverteilung im Normalspektrum", in "Verhandlungen der Deutschen Physikalischen Gesellschaft", volume 2, p. 237, Berlin, 1900.

[19] Einstein, A., "Über einen die Erzeugung und Verwandlung des Lichtes betreffenden heuristischen Gesichtspunkt", *Annalen der Physik*, volume 17: 132, 1905.

[20] Einstein, A., "Zur Quantentheorie der Strahlung", *Mitteilungen der Physikalische Gesellschaft Zürich*, volume 18: 47, 1916.

[21] Fedak, W.A. and Prentis, J.J., "The 1925 Born and Jordan paper "On quantum mechanics"", *American Journal of Physics*, volume 77, no. 2: 128, 2009.

[22] De Broglie, L., "Waves and Quanta", *Nature*, volume 112, no. 2815: 540, 1923.

[23] Abbott, B.P., Abbott, R., Abbott, T.D., et al., "Observation of Gravitational Waves from a Binary Black Hole Merger", *Phys. Rev. Lett.*, volume 116, no. 6: 16, 2016.

[24] Weiss, D.S., Young, B.C., and Chu, S., "Precision measurement of hbar/m_{Cs} based on photon recoil using laser-cooled atoms and atomic interferometry", *Applied Physics B*, volume 59, no. 3: 217, 1994.

[25] Wicht, A., Hensley, J.M., Sarajlic, E., et al., "A Preliminary Measurement of the Fine Structure Constant Based on Atom Interferometry", *Physica Scripta*, volume 2002, no. T102: 82, 2002.

[26] Schlippert, D., Hartwig, J., Albers, H., et al., "Quantum Test of the Universality of Free Fall", *Physical Review Letters*, volume 112, no. 20: 203002, 2014.

[27] Peters, A., Chung, K.K.Y., and Chu, S., "Measurement of gravitational acceleration by dropping atoms", *Nature*, volume 400, no. 6747: 849, 1999.

[28] Tino, G.M., Cacciapuoti, L., Bongs, K., et al., "Atom interferometers and optical atomic clocks: New quantum sensors for fundamental physics experiments in space", *Nuclear Physics B - Proceedings Supplements*, volume 166: 159, 2007.

[29] Poli, N., Oates, C.W., Gill, P., et al., "Optical atomic clocks", *arXiv: 1401.2378 [physics]*, 2014.

[30] Cornell, E.A. and Wieman, C.E., "Nobel lecture: Bose-Einstein condensation in a dilute gas, the first 70 years and some recent experiments", *Reviews of Modern Physics*, volume 74, no. 3: 875, 2002.

[31] Ketterle, W., "Nobel lecture: When atoms behave as waves: Bose-Einstein condensation and the atom laser", *Reviews of Modern Physics*, volume 74, no. October: 1131, 2002.

[32] Torii, Y., Suzuki, Y., Kozuma, M., et al., "Mach-Zehnder Bragg interferometer for a Bose-Einstein condensate", *Physical Review A*, volume 61, no. 4: 41602, 2000.

[33] Kasevich, M. and Chu, S., "Atomic interferometry using stimulated Raman transitions", *Physical Review Letters*, volume 67, no. 2: 181, 1991.

[34] de Angelis, M., Bertoldi, A., Cacciapuoti, L., et al., "Precision gravimetry with atomic sensors", *Measurement Science and Technology*, volume 20, no. 2: 22001, 2009.

[35] Dickerson, S.M., Hogan, J.M., Sugarbaker, A., et al., "Multiaxis Inertial Sensing with Long-Time Point Source Atom Interferometry", *Physical Review Letters*, volume 111, no. 8: 83001, 2013.

[36] Müntinga, H., Ahlers, H., Krutzik, M., et al., "Interferometry with Bose-Einstein Condensates in Microgravity", *Physical Review Letters*, volume 110: 93602, 2013.

[37] Peters, A., Chung, K.Y., and Chu, S., "High-precision gravity measurements using atom interferometry", *Metrologia*, volume 38: 25, 2001.

[38] Kessler, T., Hagemann, C., Grebing, C., et al., "A sub-40-mHz-linewidth laser based on a silicon single-crystal optical cavity", *Nature Photonics*, volume 6, no. 10: 687, 2012.

[39] Nicholson, T.L., Campbell, S.L., Hutson, R.B., et al., "Systematic evaluation of an atomic clock at 2 x 10e(-18) total uncertainty", *Nature communications*, volume 6: 6896, 2015.

[40] Bresson, A., Bidel, Y., Bouyer, P., et al., "Quantum mechanics for space applications", *Applied Physics B: Lasers and Optics*, volume 84, no. 4: 545, 2006.

[41] Udem, T., Holzwarth, R., and Hänsch, T.W., "Optical frequency metrology", *Nature*, volume 416, no. 6877: 233, 2002.

[42] Lezius, M., Wilken, T., Deutsch, C., et al., "Space-born Frequency Comb Metrology", *Optica*, volume 3, no. 12: 1381, 2016.

[43] Duncker, H., Hellmig, O., Wenzlawski, A., et al., "Ultrastable, Zerodur-based optical benches for quantum gas experiments.", *Applied optics*, volume 53, no. 20: 4468, 2014.

[44] Baumann, E., Giorgetta, F.R., Nicholson, J.W., et al., "High-performance, vibration-immune, fiber-laser frequency comb", *Optics Letters*, volume 34, no. 5: 638, 2009.

[45] Hänsel, W., Holzwarth, R., Doubek, R., et al., "Laser with non-linear optical loop mirror", patent no. US 8873601 B2, 2013.

[46] Wilken, T., Lezius, M., Hänsch, T.W., et al., "A frequency comb and precision spectroscopy experiment in space", in "CLEO: 2013", p. AF2H.5, OSA, 2013.

[47] TEXUS Team, "TX-RIBRE-ICD-TBD TEXUS Technical Report", *Technical Report*, EADS Astrium.

[48] Seidel, S.T., *Eine Quelle für die Interferometrie mit Bose-Einstein-Kondensaten auf Höhenforschungsraketen*, Ph.D. thesis, Gottfried Wilhelm Leibniz Universität Hannover, 2014.

[49] Deutsches Zentrum für Luft- und Raumfahrt (DLR), *TEXUS - Forschen in Schwerelosigkeit, Missions-Broschüre*, DLR, 2007.

[50] Cronin, A.D., Schmiedmayer, J., and Pritchard, D.E., "Optics and interferometry with atoms and molecules", *Reviews of Modern Physics*, volume 81, no. 3: 1051, 2009.

[51] van Zoest, T., Gaaloul, N., Singh, Y., et al., "Bose-Einstein Condensation in Microgravity", *Science*, volume 328, no. 5985: 1540, 2010.

[52] Dittus, H., Lämmerzahl, C., and Turyshev, S.G., *Lasers, Clocks, and Drag-Free: Exploration of Relativistic Gravity in Space*, Springer, Berlin, 2009.

[53] Phillips, W. and Metcalf, H., "Cooling and Trapping Atoms", *Scientific American*, volume 256, no. 3: 50, 1987.

[54] Chu, S., "Laser Trapping of Neutral Particles", *Scientific American*, volume 266, no. 2: 70, 1992.

[55] Chu, S., Hollberg, L., Bjorkholm, J.E., et al., "Three-Dimensional Viscous Confinement and Cooling of Atoms by Resonance Radiation Pressure", *Physical Review Letters*, volume 55, no. 1: 48, 1985.

[56] Metcalf, H.J. and Straten, P.V.D., "Laser cooling and trapping of atoms", *Journal of Optical Society of America*, volume 20, no. 5: 887, 2003.

[57] Anderson, M.H., Ensher, J.R., Matthews, M.R., et al., "Observation of Bose-Einstein condensation in a dilute atomic vapor", *Science (New York, N.Y.)*, volume 269, no. 5221: 198, 1995.

[58] Hess, H.F., "Evaporative cooling of magnetically trapped and compressed spin-polarized hydrogen", *Physical Review B*, volume 34, no. 5: 3476, 1986.

[59] Grosse, J., *Thermal and Mechanical Design and Simulation for the first High Precision Quantum Optics Experiment on a Sounding Rocket*, Ph.D. thesis, Universität Bremen, 2016.

[60] Schkolnik, V., *Probing gravity with quantum sensors - on ground and in space -*, Ph.D. thesis, Humboldt-Universität zu Berlin, 2016.

[61] Wells, H.G., *The War of the Worlds*, William Heinemann, 1898.

[62] Schawlow, A.L. and Townes, C.H., "Infrared and Optical Masers", *Physical Review*, volume 112, no. 6: 1940, 1958.

[63] von Neumann, J., *Collected Works 5: Design of computers, theory of automation and numerical analysis*, Pergamon Press, 1963.

[64] von Neumann, J., "Notes on the photon-disequilibrium-amplification scheme (JvN), September 16, 1953", *IEEE Journal of Quantum Electronics*, volume 23, no. 6: 659, 1987.

[65] Hall, R.N., Fenner, G.E., Kingsley, J.D., et al., "Coherent Light Emission From GaAs Junctions", *Physical Review Letters*, volume 9, no. 9: 366, 1962.

[66] Alferov, Z.I. and Kazarinov, R.F., "Semiconductor laser with electric pumping", patent no. 181737 [in Russian], 1963.

[67] Kroemer, H., "A proposed class of hetero-junction injection lasers", *Proceedings of the IEEE*, volume 51, no. 12: 1782, 1963.

[68] Alferov, Z., Andreev, V., Garbuzov, D., et al., "Investigation of the influence of the AlAs - GaAs heterostructure parameters on the laser threshold current and the realization of continuous emission at room temperature", *Sov. Phys.-Semicond.*, volume 4: 1573, 1971.

[69] Siegman, A., *Lasers*, University Science Books, 1st edition, 1986.

[70] Sarzała, R.P., Piskorski, Ł., Szczerbiak, P., et al., "An attempt to design long-wavelength (>2 μm) InP-based GaInNAs diode lasers", *Applied Physics A: Materials Science and Processing*, volume 108, no. 3: 521, 2012.

[71] Diehl, R., *High-power diode lasers*, Springer, Berlin, 2000.

[72] Spießberger, S., Schiemangk, M., Wicht, A., et al., "Narrow linewidth DBR-RW lasers emitting near 1064 nm", *Journal of Lightwave Technology*, volume 28, no. 17: 2611, 2010.

[73] Lewoczko-Adamczyk, W., Pyrlik, C., Häger, J., et al., "Ultra-narrow linewidth DFB-laser with optical feedback from a monolithic confocal Fabry-Perot cavity", *Optics Express*, volume 23, no. 8: 9705, 2015.

[74] DeMaria, A. and Hennessey, T., "The CO2 Laser: The Workhorse of the Laser Material Processing Industry", *SPIE Professional Magazine*, pp. 1–27, 2010.

[75] Webster, S.A., Oxborrow, M., and Gill, P., "Subhertz-linewidth Nd:YAG laser.", *Optics letters*, volume 29, no. 13: 1497, 2004.

[76] Lévèque, T., Faure, B., Esnault, F.X.X., et al., "PHARAO Laser Source Flight Model: Design and Performances", *arXiv:1502.06376 [physics]*, pp. 1–12, 2015.

[77] Theron, F., Carraz, O., Renon, G., et al., "Narrow linewidth single laser source system for onboard atom interferometry", *arXiv:1407.4684 [physics]*, 2014.

[78] Chow, W.W. and Koch, S.W., *Semiconductor - Laser Fundamentals*, Springer, 1999.

[79] Servagent, N., "Specific applications of sensors for photonic and imaging - Laser Diode Principle", http://www.optique-ingenieur.org/en/courses/OPI_ang_M05_C04/co/Contenu.html, accessed on 2015-12-22, 2007.

[80] Bartl, J., Fíra, R., and Jacko, V., "Tuning of the laser diode", *Measurement Science Review*, volume 2, no. 3: 9, 2002.

[81] Petermann, K., *Laser Diode Modulation and Noise*, Kluwer Academic Publishers, 1988.

[82] Coldren, L.A., Corzine, S.W., and Masanovic, M.L., *Diode Lasers and Photonic Integrated Circuits*, Wiley, 2nd edition, 2012.

[83] Paoli, T.L., "Saturation Behavior of the Spontaneous Emission from Double-Heterostructure Junction Lasers Operating High Above Threshold", *IEEE Journal of Quantum Electronics*, volume 9, no. 2: 267, 1973.

[84] Coenning, W. and Bürkle, H.P., "Phasendiagramme zur Beschreibung des Halbleiterlasers bei Frequenzmodulation", *Archiv für Elektrotechnik*, volume 75, no. 5: 369, 1992.

[85] Kobayashi, S., Yamamoto, Y., Ito, M., et al., "Direct Frequency Modulation In AlGaAs Semiconductor Lasers", *IEEE Transactions on Microwave Theory and Techniques*, volume 30, no. 4: 428, 1982.

[86] Petermann, K., "Calculated Spontaneous Emission Factor for Double-Heterostructure Injection Lasers with Gain-Induced Waveguiding", *IEEE Journal of Quantum Electronics*, volume 15, no. 7: 566, 1979.

[87] Henry, C.H., "Theory of the linewidth of semiconductor lasers", *IEEE Journal of Quantum Electronics*, volume 18, no. 2: 259, 1982.

[88] Kojima, K., Kyuma, K., and Nakayama, T., "Analysis of the spectral linewidth of distributed feedback laser diodes", *Journal of Lightwave Technology*, volume 3, no. 5: 1048, 1985.

[89] Nguyen, T.P., Schiemangk, M., Spießberger, S., et al., "Optimization of 780 nm DFB diode lasers for high-power narrow linewidth emission", *Applied Physics B*, volume 108, no. 4: 767, 2012.

[90] Luvsandamdin, E., Spießberger, S., Schiemangk, M., et al., "Development of narrow linewidth, micro-integrated extended cavity diode lasers for quantum optics experiments in space", *Applied Physics B: Lasers and Optics*, volume 111, no. 2: 255, 2013.

[91] Kogelnik, H., "Coupled-Wave Theory of Distributed Feedback Lasers", *Journal of Applied Physics*, volume 43, no. 5: 2327, 1972.

[92] Brox, O., Bugge, F., Mogilatenko, A., et al., "Distributed feedback lasers in the 760 to 810 nm range and epitaxial grating design", *Semiconductor Science and Technology*, volume 29, no. 9: 095018, 2014.

[93] Connelly, M., *Semiconductor Optical Amplifiers*, Kluwer Academic Publisher, Boston, 2002.

[94] Moser, A., "Thermodynamics of facet damage in cleaved AlGaAs lasers", *Applied Physics Letters*, volume 59, no. 1991: 522, 1991.

[95] Ressel, P., Erbert, G., Zeimer, U., et al., "Novel passivation process for the mirror facets of Al-free active-region high-power semiconductor diode lasers", *IEEE Photonics Technology Letters*, volume 17, no. 5: 962, 2005.

[96] Zah, C., Bhat, R., Menocal, S., et al., "1.5 um GaInAsP angled-facet flared-waveguide traveling-wave laser amplifiers", *IEEE Photonics Technology Letters*, volume 2, no. 1: 46, 1990.

[97] Sochava, S., "Semiconductor optical amplifier for an external cavity diode laser", patent no. US20080304826 A1, 2008.

[98] Bendelli, G., Komori, K., Arai, S., et al., "A new structure for high-power TW-SLA (Travelling wave semiconductor laser amplifier)", *IEEE Photonics Technology Letters*, volume 3, no. 1: 42, 1991.

[99] Fiebig, C., Blume, G., Uebernickel, M., et al., "High-power DBR-tapered laser at 980 nm for single-path second harmonic generation", *IEEE Journal on Selected Topics in Quantum Electronics*, volume 15, no. 3: 978, 2009.

[100] Fiebig, C., *Diodenlaser mit Trapezstruktur und hoher Brillanz für die Realisierung einer Frequenzkonversion auf einer mikro-optischen Bank Elektrotechnik und Informatik*, Ph.D. thesis, Technische Universität Berlin, 2013.

[101] Paschke, K., Spießberger, S., Kaspari, C., et al., "High-power distributed Bragg reflector ridge-waveguide diode laser with very small spectral linewidth", *Optics letters*, volume 35, no. 3: 402, 2010.

[102] Kohfeldt, A., Kürbis, C., Luvsandamdin, E., et al., "Compact narrow linewidth diode laser modules for precision quantum optics experiments on board of sounding rockets", *Proc. of SPIE*, volume 9900, no. 0: 99001G, 2016.

[103] Eppich, B., "Optical Design of Beam Delivery and Beam Forming Systems", *Optik and Photonik*, volume 2, no. 2: 48, 2008.

[104] Schkolnik, V., Hellmig, O., Wenzlawski, A., et al., "A compact and robust diode laser system for atom interferometry on a sounding rocket", *Applied Physics B*, volume 122, no. 8: 217, 2016.

[105] Schiemangk, M., Lampmann, K., Dinkelaker, A., et al., "High power, micro-integrated diode laser modules at 767 nm and 780 nm for portable quantum gas experiments", *Applied Optics*, volume 54, no. 17: 5332, 2015.

[106] Meschede, D., *Optik, Licht und Laser*, Vieweg+Teubner, Wiesbaden, 3rd edition, 2008.

[107] Chik, K.C.D., Devenyi, T.F., and Dyment, J.C., "Method for screening laser diodes", patent no. US4489477 A, 1985.

[108] Koenig, M., Hartmayer, R., Thiagarajan, P., et al., "Automated tests improve laser diode manufacturing", *Laser Focus World*, volume 34, no. 8, 1998.

[109] Johnson, L.A., "Laser Diode Burn-in and Reliability Testing", *IEEE Communiations*, volume 44, no. 2: 4, 2006.

[110] Huang, J.s., "Burn-In Aging Behavior and Analytical Modeling of Wavelength-Division Multiplexing Semiconductor Lasers : Is the Swift Burn-In Feasible for Long-Term Reliability Assurance ?", *Advances in OptoElectronics*, volume 2013, no. 568945, 2013.

[111] Spießberger, S., *Compact Semiconductor-Based Laser Sources with Narrow Linewidth and High Output Power*, Ph.D. thesis, Technische Universität Berlin, 2012.

[112] Schiemangk, M., Spießberger, S., Wicht, A., et al., "Accurate frequency noise measurement of free-running lasers", *Applied Optics*, volume 53, no. 30: 7138, 2014.

[113] Kourogi, M. and Ohtsu, M., "Novel optical frequency discriminator for FM noise reduction of semiconductor lasers", *Optics communications*, volume 81, no. 3-4: 204, 1991.

[114] Spießberger, S., Schiemangk, M., Wicht, A., et al., "DBR laser diodes emitting near 1064 nm with a narrow intrinsic linewidth of 2 kHz", *Applied Physics B: Lasers and Optics*, volume 104, no. 4: 813, 2011.

[115] Okoshi, T., Kikuchi, K., and Nakayama, A., "Novel method for high resolution measurement of laser output spectrum", *Electronics Letters*, volume 16, no. 16: 630, 1980.

[116] Mercer, L.B.L.B., "1/f frequency noise effects on self-heterodyne linewidth measurements", *Journal of Lightwave Technology*, volume 9, no. 4: 485, 1991.

[117] European Space Components Coordination, "Evaluation Test Programme Guidelines for Laser Diode Modules, ESCC Basic Specification No . 23201", *Technical Report 23201*, ESA, 2014.

[118] European Cooperation for Space Standardization, "Web page of the ECSS", http://ecss.nl/, accessed on 2016-12-16, 2016.

[119] European Space Components Coordination, "Web page of the ESCC", https://spacecomponents.org, accessed on 2016-12-16, 2016.

[120] Sexton, F.W., "Destructive single-event effects in semiconductor devices and ICs", *IEEE Transactions on Nuclear Science*, volume 50 III, no. 3: 603, 2003.

[121] Garden, C., "Effects of Proton Radiation on InGaAs Photodiodes and Laserdiodes", *Technical Report*, ESA, 2000.

[122] Department of Defense, "MIL-STD-202G: Test Method Standard Electronic and Electrical Component Parts", *Technical Report G*, US Department of Defense, Columbus, 2002.

[123] Department of Defense, "MIL-STD-883J: Test Method Standard Microcircuits", *Technical Report J*, US Department of Defense, Columbus, 2012.

[124] Nordland, "Norland Optical Adhesive 88", *Technical Report*, Norland Products, Cranbury, 2016.

[125] NASA, "Space Shuttle Specification Environmental Acceptance Testing", *Technical Report SP-T-0023*, NASA, 2001.

[126] Burkhardt, T., Hornaff, M., Kamm, A., et al., "Low-strain laser-based solder joining of mounted lenses", in "Proc. SPIE 9574, Material Technologies and Applications to Optics, Structures, Components, and Sub-Systems II", San Diego, California, 2015.

[127] Robins, W.P., *Phase Noise in Signal Sources: Theory and Applications*, IET, 1984.

[128] Barnes, J. and Allan, D.W., "Variances based on data with dead time between the measurement", *NIST Tech. Note*, volume 1318, 1990.

[129] Affolderbach, C. and Mileti, G., "A compact laser head with high-frequency stability for Rb atomic clocks", *Review of Scientific Instruments*, volume 76, no. 7: 1, 2005.

[130] Luvsandamdin, E., Kürbis, C., Schiemangk, M., et al., "Micro-integrated extended cavity diode lasers for precision potassium spectroscopy in space", *Optics Express*, volume 22, no. 7: 7790, 2014.

[131] Ludlow, A.D., Boyd, M.M., Ye, J., et al., "Optical atomic clocks", *Reviews of Modern Physics*, volume 87: 637, 2015.

[132] Fortier, T.M., Ashby, N., Bergquist, J.C., et al., "Improved limits on variation of the fine structure constant and violation of Local Position Invariance", *Proceedings of the IEEE International Frequency Control Symposium and Exposition*, volume 070801, no. 2: 663, 2007.

[133] Pro-Physik.de, "Bose-Einstein-Kondensat im All", http://www.pro-physik.de/details/news/10417601/Bose-Einstein-Kondensat_im_All.html, accessed on 2017-03-16, 2017.

[134] Kulas, S., Vogt, C., Resch, A., et al., "Miniaturized lab system for cold atom experiments in microgravity", *Microgravity Science and Technology*, pp. 1–12, 2016.

List of Figures

List of Tables